D I S S E R T A T I O N

Thermal and Thermoelectric Properties of Nanostructures

ausgeführt zum Zwecke der Erlangung des akademischen Grades
eines Doktors der technischen Wissenschaften

eingereicht an der Technischen Universität Wien
Fakultät für Elektrotechnik und Informationstechnik
von

Hossein Karamitaheri

Wien, im Juli 2013

Kurzfassung

Die Fähigkeit eines Materials, Wärme in elektrische Energie umzuwandeln, wird durch die dimensionslose Größe $ZT = S^2\sigma T/\kappa$ bestimmt. Dabei ist S der Seebeckkoeffizient, σ die elektrische Leitfähigkeit, T die Temperatur und κ die Wärmeleitfähigkeit. Gute thermoelektrische Materialien sollen daher einen hohen Seebeckkoeffizienten, eine gute elektrische Leitfähigkeit sowie eine geringe Wärmeleitfähigkeit besitzen. Durch die starke gegenseitige Abhängigkeit dieser Größen ist es schwierig, ZT-Werte über eins zu erreichen, womit allerdings nur geringe Wirkungsgrade erreichbar sind. Fortschritte in der Nanofabrikation haben zu einem experimentellen Durchbruch bei nanostrukturierten, thermoelektrischen Bauelementen geführt. In dieser Arbeit wurden die thermischen und thermoelektrischen Eigenschaften von Silizium- und Graphenbasierten Nanostrukturen numerisch untersucht. Die berechneten Größen umfassen den Seebeckkoeffizienten, die elektrische und die thermische Leitfähigkeit sowie den ZT-Wert.

Im Fall der Graphen-basierten Nanostrukturen wurde die sogenannte "Force Constant" Methode zur Berechnung der thermischen Eigenschaften verwendet, und die "Tight-Binding" Methode zur Berechnung der elektronischen Eigenschaften. Es wurden sowohl die ballistischen als auch die diffusiven Transporteigenschaften untersucht, wobei für erstere der Landauer-Formalismus und für letztere die Methode der Nichtgleichgewichts-Greenschen Funktionen verwendet wurde. Für sogenannte "armchair graphene nanoribbons" (AGNR) wurde der Übergang vom ballistischen zum diffusiven Transportverhalten untersucht. Die Ergebnisse zeigen, dass in AGNR der thermoelektrische Leistungsfaktor $S^2\sigma$ auf Grund des Beitrages des zweiten Leitungsbandes mit der Breite der nanoribbons zunimmt. Andererseits wird mit zunehmender Breite die Bandlücke kleiner, wodurch der Seebeckkoeffizient und damit der Leistungsfaktor abnimmt. Auf Grund dieses Zusammenhanges bleibt der ballistische ZT-Wert mit 0.3 beschränkt. Unter Berücksichtigung der Kantenrauigkeit wird der Elektronentransport deutlich stärker als der Phononentransport beeinträchtigt. Daher ist der diffusive ZT-Wert von AGNR mit Kantenrauheit kleiner als der ballistische, und ZT sinkt mit zunehmender Länge.

Im Falle von sogenannten "zigzag graphene nanoribbons" (ZGNR) konnte gezeigt werden, dass positive Hintergrundladungen sowie Liniendefekte in Längsrichtung zu einer Asymmetrie in der Modendichte um das Ferminiveau führen, wodurch der Seebeckkoeffizient verbessert wird. In Gegensatz zu AGNR wird in ZGNR durch die Kantenrauheit die Phononenleitfähigkeit wesentlich stärker als die Elektronenleitfähigkeit reduziert. Durch Liniendefekte und Kantenrauheit können ZGNR theoretisch ZT Werte um 4 erreichen.

In Graphen, das in seiner ursprünglichen Form keine Bandlücke besitzt, kann durch Strukturierung in ein sogenanntes "Antidot"-Gitter eine kleine Bandlücke erzeugt werden. Wir zeigen, dass Größe und Umfang der Antidots sowie deren Abstand einen großen Einfluss auf die thermischen Eigenschaften haben. Durch die geeignete Wahl dieser Parameter kann die thermische Leitfähigkeit von Antidot-Gittern signifikant reduziert und ein ZT Wert von etwa 0.3 erreicht werden.

Für Silizium-basierte Nanostrukturen wurde die sogenannte "Modified-Valence-Force-Field" Methode zur Berechnung des Phononenspektrums verwendet. Es wurden Silizium-Nanodrähte mit Durchmessern zwischen 1 und 10 nm sowie ultradünne Silizium-Filme mit Dicken zwischen 1 und 16 nm untersucht. Unsere Resultate zeigen, dass die Phononen-Gruppengeschwindigkeiten und damit die thermische Leitfähigkeit in <110> Nanodrähten am höchsten und in <111> Nanodrähten am niedrigsten sind.

In ultradünnen Silizium-Filmen ist der ballistische thermische Leitwert anisotrop. Für die Kombination {110}/<110> aus Oberflächenorientierung und Transportrichtung finden wir den höchsten Leitwert, für {112}/<111> den niedrigsten. Das Verhältnis ist ungefähr zwei. <111> Nanodrähte sowie {112}/<111> Filme sind somit am geeignetsten für thermoelektrische Bauelemente vom Standpunkt der thermischen Leitfähigkeit. Die Effekte von Streuprozessen wie etwa der Phonon-Phonon-Streuung und der Oberflächenrauigkeits-Streuung wurden mit Hilfe der Boltzmanntransportgleichung für Phononen untersucht. Ein bemerkenswertes Ergebnis ist dass die thermische Leitfähigkeit von quasi-eindimensionalen Nanodrähten mit abnehmendem Durchmesser divergiert. Der Grund liegt darin, dass bei verschwinedr Energie die Zustandsdichte und somit die Phononen-Transmissionsfunktion in ultraschmalen Nanodrähten einen endlichen Wert annimmt, während sie in Bulkmaterialien den Wert Null annimmt. Dadurch steigt der Beitrag von Phononen mit großen Wellenlängen zur Wärmeleitung beträchtlich an.

Bei einer gegebenen Oberflächenrauigkeit erfahren Phononen in ultradünnen Nanodrähten häufiger eine Spiegelreflexion an der Oberfläche und seltener eine diffusive Streuung. Mit zunehmendem Durchmesser ändert sich dieses Verhältnis in Richtung Zunahme der diffusiven Streuprozesse. Dies resultiert in einen markanten, anomalen Anstieg der thermischen Leitfähigkeit bei Durchmessern unter 5 nm. Mit der berechneten thermischen Leitfähigkeit und Abschätzungen für den Leistungsfaktor $S^2\sigma$ von ultraschmalen Nanodrähten aus der Literatur kann der ZT-Wert bei 300 K im besten Falle mit 0.75 abgeschätzt werden. Dieser für Silizium relativ hohe Werte wird hauptpsächlich durch eine signifikante Reduktion der Wärmeleitfähigkeit durch Oberflächenstreuung der Phononen erreicht. Im Falle vollständig diffusiver Oberflächen wären ZT-Werte für n- und p-dotierte Nanodrähte von über eins erreichbar.

Abstract

The ability of a material to convert heat into electricity is measured by the dimensionless thermoelectric figure of merit $ZT = S^2 \sigma T / \kappa$, where S is the Seebeck coefficient, σ the electrical conductivity, T the temperature, and κ the thermal conductivity. Good thermoelectric materials should simultaneously have a high Seebeck coefficient, a high electrical conductivity, and a low thermal conductivity. Due to the strong interconnection between the parameters that control ZT, it has been traditionally proved difficult to achieve values above unity, which translates to low conversion efficiencies. Recent advancements in nanofabrication, however, have led to breakthrough experiments on nanostructured thermoelectric devices. In this thesis, the thermal and thermoelectric properties of silicon- and graphene-based nanostructures are numerically investigated. The Seebeck coefficient, electrical conductivity, and thermal conductivity in nanostructures are computed, and the thermoelectric figure of merit is extracted.

For graphene-based nanostructures, we employ the force constant method for the calculations of the phononic properties, and the tight-binding model for the electronic properties. Both ballistic and diffusive transport regimes are considered employing the Landauer approach and the non-equilibrium Greens function technique, respectively. The ballistic to diffusive crossover of the thermoelectric properties of graphene nanoribbons with armchair edges has been studied. Our results indicate that in armchair graphene nanoribbons the power factor $S^2\sigma$ increases with the width due to the contribution of the second conduction subband. However, the small band-gap of wide ribbons degrades the Seebeck coefficient which results in a low power factor. Including the high thermal conductance of graphene, we show that the ballistic ZT value remains below 0.3. The introduction of edge roughness degrades the transport of electrons much more than that of phonons. The diffusive ZT values of armchair ribbons, therefore, are smaller than the ballistic ones, and the thermoelectric performance decreases with increasing the channel length. On the other hand, by introducing ordered antidots, the zero band-gap graphene can be converted into a narrow band-gap semiconductor. We show that the size and the circumference of the antidots, and the distance between them can strongly influence the thermal properties of graphene antidot lattices. By appropriate selection of the antidot parameters, the thermal conductance can be significantly reduced and $ZT \approx 0.3$ achieved. In the case of zigzag graphene ribbons, positively charged substrate background impurities and extended line defects in the length direction of the nanoribbon create an asymmetry in the density of modes around the Fermi level, which improves the Seebeck coefficient. In contrast to armchair ribbons, here, the introduction of edge roughness degrades the

phonon thermal conductivity much more than the electronic thermal conductivity. In zigzag graphene nanoribbons these effects can theoretically result in large ZT values of around 4.

For silicon-based nanostructures, we employ atomistic calculations of the phonon modes using the modified-valence-force-field method. We consider ultra-narrow silicon nanowires of side sizes of 1 to 10 nm as well as ultra-thin silicon layers of thicknesses between 1 and 16 nm. Our results indicate that <110> nanowires have the highest phonon group velocity and thermal conductance, whereas <111> nanowires have the lowest. We also find that the ballistic thermal conductance in the thin layers is anisotropic, with the {110}/<110> channels exhibiting the highest and the {112}/<111> channels the lowest thermal conductance with a ratio of about two. The <111> nanowires and {112}/<111> thin layers are thus the most suitable channels for thermoelectric devices in terms of the thermal conductance. The effects of scattering mechanisms, such as phonon-phonon scattering and surface roughness scattering are investigated employing the Boltzmann transport equation for phonons. The thermal conductivity of quasi-1D nanowires diverges as the diameter is reduced. We attribute this to the fact that in ultra-narrow nanowires the density-of-states and the transmission function of long-wavelength phonons acquires a finite value, as compared to zero in the bulk materials, which increases their importance in carrying heat. At the same roughness conditions, boundary scattering is more specular for the ultra-narrow nanowires, and becomes more diffusive as the diameter is increased. This results in a striking anomalous increase in the thermal conductivity as the diameter is reduced below 5 nm. Taking the electronic power factor of ultra-narrow silicon nanowires from literatures, we show that in the best case the ZT value at 300 K is around 0.75. The largest contribution towards achieving this relatively high value is attributed to the significant reduction in the thermal conductivity due to boundary scattering of phonons. In the case of fully diffusive boundaries, the ZT values can increase above unity for both n-type and p-type nanowires.

Acknowledgment

It would not have been possible to write this doctoral thesis without the help and support of the kind people around me, to only some of whom it is possible to give particular mention here.

Foremost, I would like to express my sincere gratitude to my supervisor and friend Prof. Hans Kosina, for the continuous support of my Ph.D study and research, for his patience, help, support, and motivation. My sincere thanks also goes to Dr. Neophytous Neophytou and Dr. Mahdi Pourfath for their help and guidance in all the time of research and writing of this thesis.

The Institute for Microelectronics has supported me to complete my thesis. My special thanks goes to Prof. Siegfried Selberherr, Prof. Erasmus Langer, and Prof. Tibor Grasser.

In addition, I have been very privileged to get to know and to collaborate with many other great people who became friends over the last few years. Hereby, I would like to thank the following (in alphabetical order):

Oskar Baumgartner, Markus Bina, Hajdin Ceric, Johann Cervenka, Raffaele Alberto Coppeta, Lado Filipovic, Lidija Filipovic, Wolfgang Gös, Ewald Haslinger, Philipp Hehenberger, Manfred Katterbauer, Hiwa Mahmoudi, Alexander Makarov, Mahdi Moradinasab, Mihail Nedjalkov, Roberto Orio, Dmitry Osintsev, Vassil Palankovski, Karl Rupp, Franz Schanovsky, Anderson Singulani, Zlatan Stanojevic, Viktor Sverdlov, Oliver Triebl, Stanislav Tyaginov, Paul-Jürgen Wagner, Michael Waltl, Josef Weinbub, Thomas Windbacher, Renate Winkler, and Wolfhard Zisser.

Last but not the least, I would like to thank my parents, for supporting me spiritually throughout my life.

Contents

List of Figures

List of Tables

List of Abbreviations

DOS	$\cdots$	Density-of-states
GAL	$\cdots$	Graphene antidot lattice
GNR	$\cdots$	Graphene nanoribbon
AGNR	$\cdots$	Armchair graphene nanoribbon
ZGNR	$\cdots$	Zigzag graphene nanoribbon
FCM	$\cdots$	Force constant method
NEGF	$\cdots$	Non-equilibrium Green's function
NN	$\cdots$	Nearest neighbor
VFF	$\cdots$	Valence force field
MVFF	$\cdots$	Modified valence force field
KVFF	$\cdots$	Keating valence force field
LCAO	$\cdots$	Linear combination of atomic orbitals
BTE	$\cdots$	Boltzmann transport equation
SMRT	$\cdots$	Single-mode relaxation time
LER	$\cdots$	Line-edge-roughness
MFP	$\cdots$	Mean free path
ELD	$\cdots$	Extended line defects
SRS	$\cdots$	Surface roughness scattering
BZ	$\cdots$	Brillouin zone
DFT	$\cdots$	Density functional theory
CNT	$\cdots$	Carbon nanotube

1 Introduction

The second law of thermodynamics indicates that in any energy conversion process there is some waste heat the amount of which depends on the efficiency of the thermodynamic engine. The efficiency of typical heat engines is around 40%. In other words, nearly 60% of the energy is wasted in the form of heat [1]. Thermoelectric generators are solid state devices that can be used to convert part of this waste heat into useful electrical energy. Thermoelectricity is currently obtaining large interest, especially from the automobile industry. For example, the BMW car-manufacturer is planning to use a 1 kW thermoelectric generator at the exhaust pipes of its cars for fuel saving (see Fig. 1.1). This interest in thermoelectricity is due to the fact that currently about 60% of the energy in automobiles is wasted as heat, one third of which is through the exhaust pipe [1]. Other than energy harvesting, thermoelectric devices can also be used in a very wide range of applications including solid state refrigeration, semiconductor lasers, aerospace applications, and military applications. However, thermoelectric devices have not yet been used in large scale applications because of their limited efficiency, high costs and material availability. In this chapter, we introduce the basic principles of thermoelectric phenomena and thermoelectric devices, and the importance of using nanotechnologies in order to enhance their efficiency.

Figure 1.1: A 200 W thermoelectric generator is used in BMW's automobile (The 31st international and 10th European conference on thermoelectrics, July 9-12, 2012, Aalborg, Denmark).

1.1 Fundamentals of Thermoelectrics

Thermoelectric phenomena in materials can be described through three thermoelectric effects, the Seebeck effect, the Peltier effect, and the Thomson effect. The Seebeck effect, discovered in 1821 by Thomas Johann Seebeck [2], represents the generation of an electromotive force by a temperature gradient. When a temperature gradient is applied along a conductive material, charge carriers move from the hot to the cold side. In the case of open-circuit, charge accumulation results in an electric potential difference, as shown in Fig. 1.2. The Seebeck coefficient S of a material shows the magnitude of the induced voltage in response to the temperature difference:

$$\Delta V = \int_{T_{\mathrm{C}}}^{T_{\mathrm{H}}} S(T) dT \tag{1.1}$$

where T_{C} and T_{H} are the temperatures of the cold and the hot side, respectively. The Seebeck coefficient of a material is generally a function of temperature. However, if the temperature difference $\Delta T = T_{\mathrm{H}} - T_{\mathrm{C}}$ is small enough, and the Seebeck coefficient is nearly constant in the range of applied temperatures, one has:

$$S = \left.\frac{\Delta V}{\Delta T}\right|_{I=0} \tag{1.2}$$

A single thermoelectric conductor, however, is not able to play the role of a battery. This is due to the fact that the net loop voltage would be zero if circuit wires of the same conductor were connected. A non-zero loop voltage can be obtained when two dissimilar conductors are connected in the configuration shown in Fig. 1.3. The circuit configuration of a thermoelectric generator is shown in Fig. 1.4-a. Here the generator is composed of two materials, an n-type and a p-type material. The voltage obtained from this configuration is:

$$\Delta V = S_{pn}\Delta T = (S_p - S_n)\Delta T \tag{1.3}$$

where S_p and S_n are the Seebeck coefficients of the p-type and n-type materials, respectively, and S_{pn} is the Seebeck coefficient of the device (junction). The Seebeck coefficient of a p-type material is positive, that of an n-type material negative. Therefore, using this configuration one can achieve a high net voltage.

The Peltier effect, on the other hand, discovered by Athanaseal Jean Charles Peltier in 1834, describes how an electrical current can create a heat flow. This effect has enabled the second application of thermoelectric devices, the thermoelectric cooler, as shown in Fig. 1.4-b. Here, by applying an external power source, both the electrons of the n-type conductor and the holes of the p-type conductor move and carry heat from one side to the other. Therefore, one side cools down, whereas the other side heats
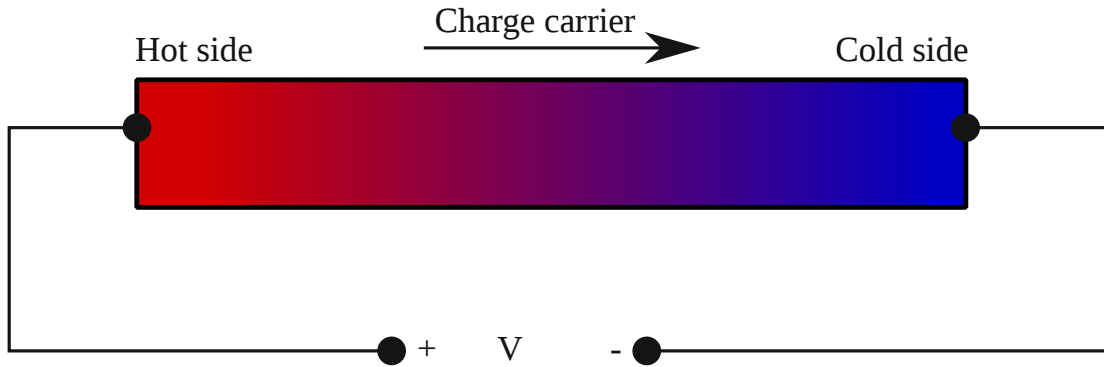
Figure 1.2: Seebeck effect: Electric potential formation in response to the temperature gradient applied along the open-circuit channel.
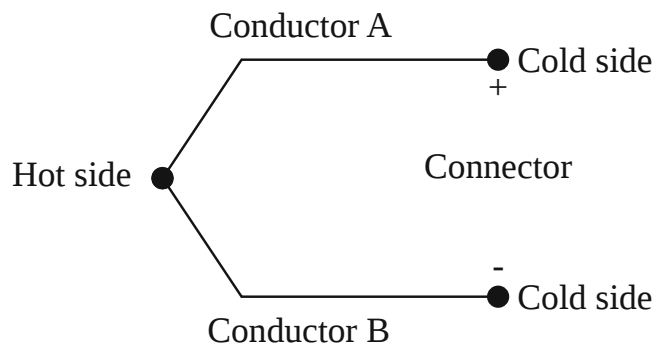
Figure 1.3: Configuration of a thermoelectric generator composed of two dissimilar materials.

up. The heat flow absorbed at the hot side is proportional to the current through the junction:

$$\dot{Q} = \Pi_{pn} I = (\Pi_p - \Pi_n) I \tag{1.4}$$

where, Π_p, Π_n, and Π_{pn} are the Peltier coefficients of the p-type material, the n-type material, and the device, respectively [3].

The Thomson effect, observed by William Thomson in 1851, expresses a relation for heat production in a current-carrying conductor in the presence of temperature gradient:

$$q_H = \rho J^2 - \mu J \frac{dT}{dx} \tag{1.5}$$

where q_H is the heat production per volume, ρ the electrical resistivity, J the current density, and μ the Thomson coefficient. Considering the second term in Eq. 1.5, the conductor can either release or absorb the heat, depending on the direction of current with respect to the temperature gradient.

According to the Thomson relations, these three thermoelectric coefficients are not

3
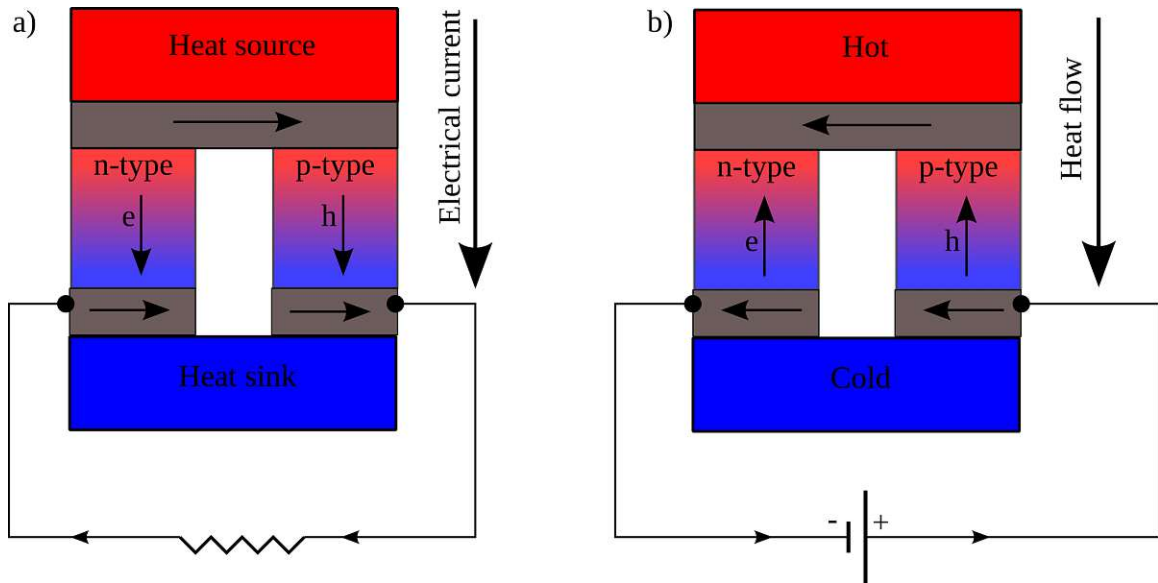
Figure 1.4: Circuit configuration for (a) generator and (b) cooler applications.

independent. The Peltier coefficient and the Seebeck coefficient are linearly related to each other [3]

$$\Pi = ST \tag{1.6}$$

whereas the Thomson coefficient can be expressed as [3]:

$$\mu = T\frac{dS}{dT} \tag{1.7}$$

Therefore, the Seebeck coefficient as a function of temperature is enough for describing all three thermoelectric phenomena. In Chapter 2, the computational method for obtaining the Seebeck coefficient, as well as the calculation of the other transport coefficients, is presented. It is, however, worth mentioning that one can only measure the Seebeck coefficient for a pair (junction) of dissimilar materials, but not of an individual conductor, whereas measurement of the Thomson coefficient is possible even for individual materials.

1.2 Device Efficiency

The efficiency of thermoelectric devices in converting heat into the electricity is defined as the ratio of "energy provided to the external load" to "heat energy absorbed at the hot junction". The maximum efficiency $\eta_{\max}$ of the power generator is achieved when

the external load is matched with the device resistance [3]:

$$\eta_{\max} = \frac{T_{\mathrm{H}} - T_{\mathrm{C}}}{T_{\mathrm{H}}} \frac{\sqrt{1 + ZT_{\mathrm{M}}} - 1}{\sqrt{1 + ZT_{\mathrm{M}}} + \frac{T_{\mathrm{C}}}{T_{\mathrm{H}}}} \tag{1.8}$$

Here,

$$ZT_{\mathrm{M}} = \frac{1}{T_{\mathrm{H}} - T_{\mathrm{C}}} \int ZT dT \tag{1.9}$$

is the average of the thermoelectric device figure of merit ZT defined as:

$$ZT = \frac{(S_p - S_n)^2\, T}{\left[\sqrt{\rho_n \kappa_n} + \sqrt{\rho_p \kappa_p}\right]^2} \tag{1.10}$$

where κ_n and κ_p are the thermal conductivities of n-type and p-type materials, respectively.

The efficiency of a thermoelectric power generator, as any other heat engine, is less than the Carnot engine efficiency:

$$\eta_{\mathrm{Carnot}} = \frac{T_{\mathrm{H}} - T_{\mathrm{C}}}{T_{\mathrm{H}}} \tag{1.11}$$

Indeed, the Carnot engine has the most efficient cycle for converting a given amount of thermal energy into work. In addition to the temperature difference, $\eta_{\max}$ is also related to the average of ZT, which is related to the material properties of the n-type and p-type materials used in the thermoelectric element. Figure 1.5 shows the maximum efficiency of the thermoelectric generator as a function of T_{H} for $T_{\mathrm{C}} = 300$ K and different ZT_{M}. The efficiency increases with ZT_{M} and T_{H}. For $ZT_{\mathrm{M}} = 0.1$, the maximum efficiency is about 5%. The efficiency for high T_{H} increases to $\sim 20\%$ and $\sim 40\%$ for $ZT_{\mathrm{M}} = 1$ and $ZT_{\mathrm{M}} = 3$, respectively. The efficiency of Carnot cycle is plotted as well for comparison. We also note that the efficiency of some other common energy convertors is as follows: $80\% - 90\%$ for hydro-electric technologies, $50\% - 70\%$ for fuel cells, $40\% - 50\%$ for wind turbines, and $20\% - 40\%$ for tidal turbines [1]. As a result, an average figure of merit higher than 3 is required, in order to compete with the rest of the commercial generators that are already in large-scale use in the market [4].

The thermoelectric device figure of merit and the efficiency are related to the material properties of the n-type and p-type semiconductors as well as the electrical and thermal contact resistances. For simplicity, the thermoelectric material figure of merit:

$$ZT = \frac{S^2 T}{\rho \kappa} \tag{1.12}$$

can provide an approximation for the thermoelectric figure of merit. The Eq. 1.12

5
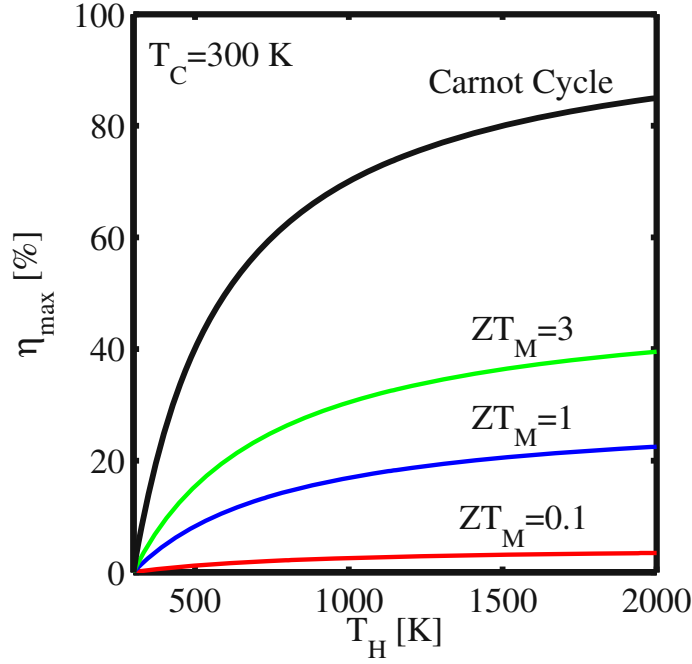
Figure 1.5: The maximum thermoelectric generator efficiency η_{max} with is shown as a function of T_H for $T_C = 300$ K and different average figure of merit. For comparison, the Carnot efficiency is plotted as well.

can be alternatively written in terms of the electrical conductance G and thermal conductance K as:

$$ZT = \frac{S^2GT}{K} \tag{1.13}$$

However, one should note that to achieve a high efficiency, it is necessary to have both n- and p-type materials with high average ZT over a wide range of temperatures [1].

1.3 Thermoelectric Materials

Bismuth telluride Bi_2Te_3, a narrow bandgap semiconductor, is one of the most commonly used thermoelectric materials [5]. It has been shown that by adding antimony telluride Sb_2Te_3 and bismuth selenide Bi_2Se_3 to Bi_2Te_3, it is possible to obtain a ZT of around unity. In turn, it was shown that by alloying of Bi_2Te_3 with bismuth selenide and antimony telluride, the thermal conductivity decreases, without significant degradation of the electrical conductivity [3]. As mentioned in Sec. 1.2, working at high temperature is advantageous for energy conversion efficiency. However, the alloys of bismuth telluride are not suitable at temperature higher than 400 K. Common

thermoelectric materials for higher temperatures are lead telluride (PbTe) and silicon-germanium alloys. These materials have ZT between 0.5 and 1.1, depending on the temperature and the type of material (whether n-type or p-type) [3]. As a result, the average efficiency of current thermoelectric generators is about 5% [6].

Good thermoelectric materials should simultaneously have a high Seebeck coefficient, a high electrical conductivity, and a low thermal conductivity. While each property of ZT can individually be changed by several orders of magnitude, the interdependence and coupling between these properties in bulk materials have made it extremely difficult to increase $ZT > 1$. In the case of bulk materials, assuming the effective mass approximation and Fermi-Dirac statistics, one can relate the Seebeck coefficient and the electrical conductivity σ to the carrier concentration n as [6]:

$$S = \frac{8\pi^2 k_{\mathrm{B}}^2}{3eh^2} m^* T \left(\frac{\pi}{3n}\right)^{2/3} \tag{1.14}$$

and

$$\sigma = ne\mu \tag{1.15}$$

where, k_{B} is the Boltzmann constant, h the Planck constant, e the elementary charge, m^* the effective mass, and μ the carrier mobility. In addition, the Wiedemann-Franz law relates the thermal conductivity of charge carriers to the electrical conductivity by:

$$\kappa_e = L\sigma T \tag{1.16}$$

where L is the Lorenz number:

$$L = \frac{\pi^2}{3}\left(\frac{k_{\mathrm{B}}}{e}\right)^2 = 2.44 \times 10^{-8} \ \mathrm{V}^2/\mathrm{K}^2 \tag{1.17}$$

The electrical conductivity is proportional to the carrier concentration, whereas the Seebeck coefficient is inversely proportional to the carrier concentration. Therefore, if one tries to increase ZT by increasing n and thus σ, one may lose the gain through the reduction of S (and increase in κ_e). Figure 1.6 schematically shows that insulators have high Seebeck coefficient and extremely low electrical conductivity, whereas metals have high electrical conductivity and a low Seebeck coefficient [7]. Therefore, in semiconducting materials a finite maximum of the thermoelectric power factor is achieved. As a result, the most effective way to enhance the thermoelectric figure of merit of bulk materials is to decrease the lattice contribution to the thermal conductivity κ_l. However, thermal conductivity reduction, without decreasing the power factor, was not possible for a long time (in all efforts up to the 1990s), and the ZT values were limited to unity. This translates to low conversion efficiencies and limited applications for thermoelectricity.
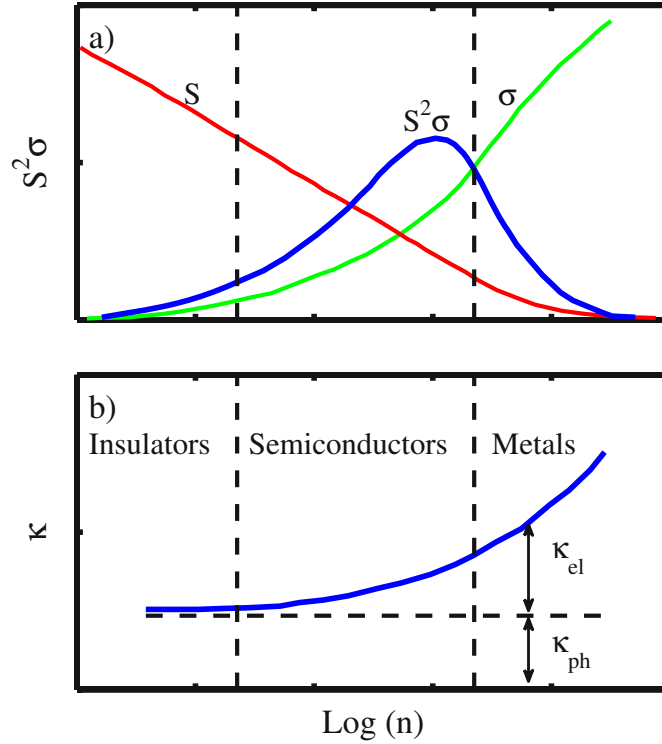
Figure 1.6: Variation of the transport coefficients as a function of the carrier concentration.

1.4 Nanostructured Materials for Thermoelectrics

In the last two decades thermoelectric devices received significant attention, mainly due to the introduction of nanostructures with promising thermoelectric properties. One of the first approaches was the phonon-glass-electron-crystal (PGEC) approach. This means that one has to design nanostructured materials which simultaneously decrease the thermal conductivity and keep the carrier mobility unchanged [8]. Another approach, suggested by Dresselhaus [9, 10], is related to the shape of the density of states (DOS) of low-dimensional materials. It has been argued that sharp features in the $DOS(E)$ function of 1D and 2D conductors can result in a higher Seebeck coefficient and higher thermoelectric performance. As shown in Fig. 1.7, the density of states of 1D nanostructures has sharp features that could increase the Seebeck coefficient. In a different work, it was pointed out that the best thermoelectric material would be the one with a delta-function shape $DOS(E)$ [11]. This ideal thermoelectric material, however, benefits from the zero value for the electrical carrier contribution to the thermal conductivity, which minimizes the dominator of ZT [11, 12]. Nanostructures could in addition offer several degrees of freedom for parameter optimization, i.e. geometrical parameters such the diameter of nanowires and thickness of thin-layers,
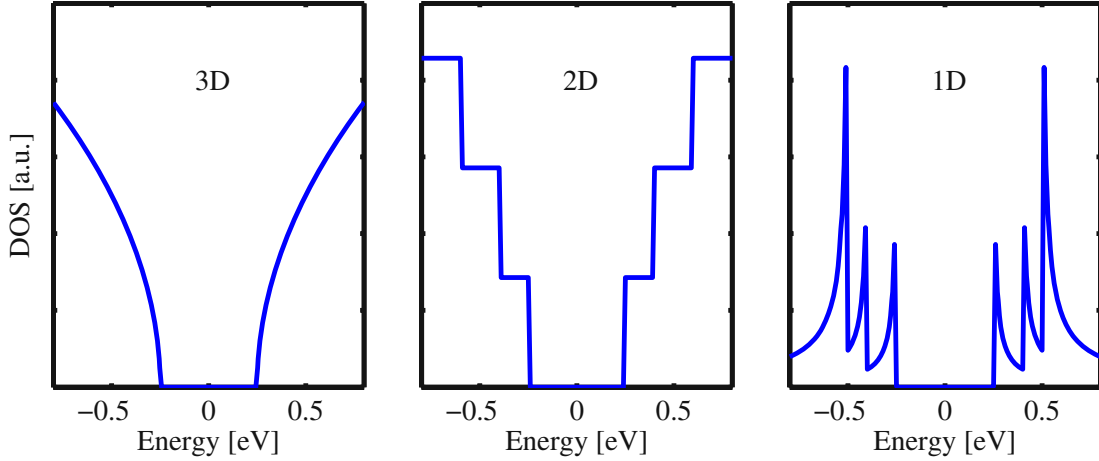
Figure 1.7: The density of states for 3D, 2D and 1D structures in the effective mass approximation.

and provide the possibility of independently designing the quantities that control ZT. The advancements in lithography and nanofabrication have recently led to the realization of breakthrough experiments on nanostructured thermoelectric devices that demonstrated enhanced performance, sometimes even up to 2 orders of magnitude higher than the performance of corresponding bulk material, as shown in Fig. 1.8.

These experimental (and theoretical) studies utilize several forms of nanostructures, such as bulk materials with nanocomposites, in-plane and out-plane transport superlattices, nanowires and nanoribbons, and 1D supperlattices. As mentioned in Sec. 1.3, one of the first efforts to improve ZT of bulk materials was alloying Bi_2Te_3 [3, 13] to decrease the lattice thermal conductivity, without significant reduction in the electrical conductivity. Similar approaches have been recently followed by introducing ErAs nanoparticles of $1 - 5$ nm in diameter in InGaAs/AlAs structures [14, 15]. These nanopariticles effectively behave as scattering centers for phonons. In addition, they provide charge carriers that improve the electrical conductivity.

Further improvement can be achieved in low dimensional materials. 2D supperlattices have been studied for providing simultaneous enhancement of the thermoelectric power factor, and reduction of thermal conductivity [4, 16]. In these structures, the power factor could increase due to the quantum confinement, strain engineering, and the sharp features of the 2D density of states. In addition, various scattering mechanisms such as boundary scattering, interface scattering, and defects scattering decrease the thermal conductivity. These mechanisms can even be stronger in 1D structures such as nanowires and nanoribons, as their ratio of boundary surface to volume is higher. To date, several studies have been performed on silicon nanowires [17], Si/Ge superlattice nanowires [18], and graphene nanoribbons [19]. However, the record high ZT of about 2.4 was experimentally achieved for p-type $Bi_2Te_3/Sb_2 2Te_3$ superlattices (see

9
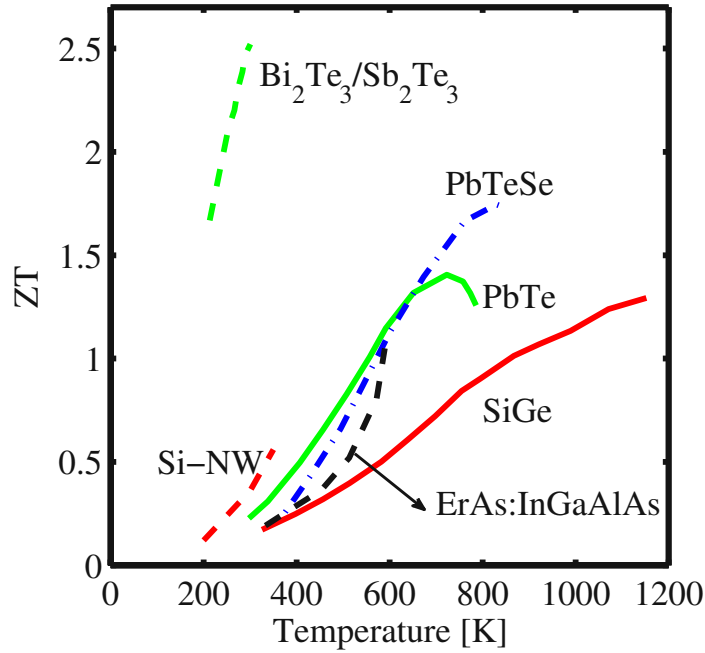
Figure 1.8: ZT values of nanostructured material as a function of temperature. Data taken from Refs. [1, 15–17].

Fig. 1.8) [16], which is composed of the best bulk thermoelectric materials.

1.5 Graphene- and Silicon-based Nanostructures

Bismuth and its compounds that are commonly used in thermoelectric applications [5] suffer from high cost. In addition, tellurium compounds cannot be used in large-scale applications due to rarity. Silicon, on the other hand, is the second most abundant element on earth and has been used in large scale manufacturing processes. Silicon is the most widely used material in semiconductor industry and its fabrication process are optimized. Silicon crystallizes in a diamond structure with lattice constant of $a_c \sim$ 0.54 nm (see Fig. 1.9) and has a bandgap of nearly 1.1 eV and thermal conductivity of $\kappa_l = 149$ W/mK at room temperature. Due to high thermal conductivity at room temperature bulk silicon has $ZT \approx 0.01$, which makes it a very poor thermoelectric. However, recent experimental studies showed that the thermal conductivity is sharply reduced in silicon-based nanostructures, i.e. nanowires and thin layers [17, 20, 21]. The large reduction in the thermal conductivity was attributed to enhanced scattering of phonons on the surfaces of the nanochannels. As a result, ZT values of about 0.6 were achieved at room temperature, a large improvement compared to ZT of bulk silicon. Furthermore, it should be possible to reach even higher values of ZT using techniques
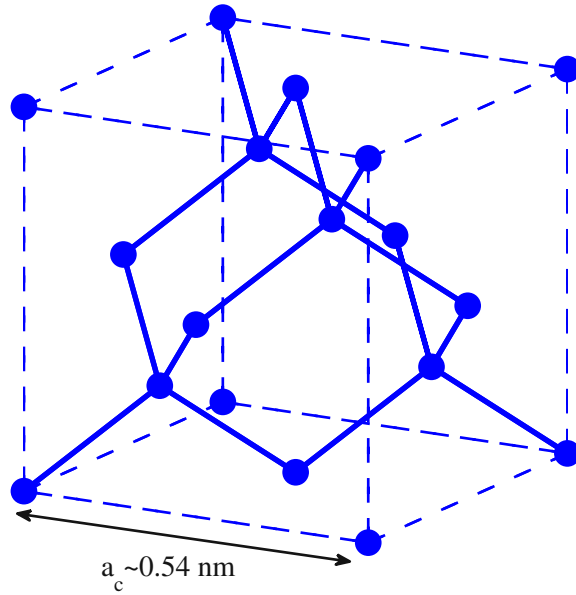
Figure 1.9: Diamond crystal structure of silicon.

for optimizing the geometry, transport and confinement orientations, and confinement size.

On the other hand, graphene, a recently discovered form of carbon, has received much attention over the past few years due to its excellent electrical, optical, and thermal properties [22]. As shown in Fig. 1.10, carbon atoms in graphene are tightly packed into a two-dimensional (2D) honeycomb lattice due to their sp^2 hybridization. The primitive unit cell is defined by two lattice vectors $\vec{a}_1$ and $\vec{a}_2$:

$$\vec{a}_1 = \frac{3}{2}a_{cc}\hat{x} + \frac{\sqrt{3}}{2}a_{cc}\hat{y} \qquad (1.18)$$

and

$$\vec{a}_1 = \frac{3}{2}a_{cc}\hat{x} - \frac{\sqrt{3}}{2}a_{cc}\hat{y} \qquad (1.19)$$

where $a_{cc} = 0.14$ nm is carbon-carbon bond length. The lattice (unit cell) is composed of two sublattices called A and B. Although the electrical conductance of graphene is as high as that of copper [23], as a zero bandgap material, pristine graphene has a small Seebeck coefficient [24]. However, one can open up bandgaps by appropriate patterning of graphene sheets [25–27]. Many theoretical studies have been recently performed on the thermal conductivity of graphene-based structures as well. It has been shown that boundaries and edge roughness can strongly degrade [19] its high thermal conductance [28, 29]. Recently, a large scale method to produce graphene sheets has been reported [30], which could pave the way for large scale graphene
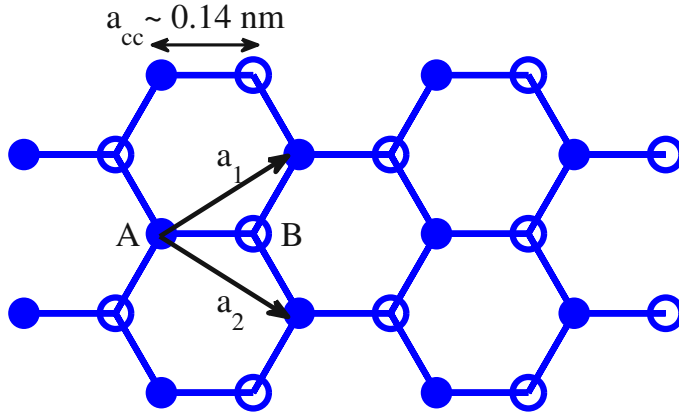
Figure 1.10: The crystal structure for graphene is defined by lattice vectors $\vec{a}_1$ and $\vec{a}_2$, and the basis includes two carbon atoms called type A and type B.

applications. These factors render graphene as a candidate for future thermoelectric applications.

2 Physical Models

The thermoelectric figure of merit for materials is defined as:

$$ZT = \frac{S^2GT}{(K_{\mathrm{el}} + K_{\mathrm{ph}})} \tag{2.1}$$

where S is the Seebeck coefficient, G the electrical conductance, T the temperature, K_{el} and K_{ph} the electrical and lattice contributions to the thermal conductivity, respectively [3]. The numerator of Z is called power factor. The figure of merit determines the efficiency of a thermoelectric material (device) and can be improved by increasing the power factor and decreasing the thermal conductivity. Hence, thermoelectric materials must simultaneously have a high Seebeck coefficient, a high electrical conductivity, and a low thermal conductivity. For ballistic channels, one needs to employ conductances instead of conductivities in the Eq. 2.1. For channels in which diffusive transport prevails, however, the actual conductivity values are employed.

In this chapter, the methodology used for calculating the thermoelectric coefficients is discussed. Two steps are needed in the simulation procedure: i) material properties, a step including the calculation of electronic and phononic bandstructures and ii) transport properties, using formalisms such as the Landauer approach and Boltzmann transport theory.

2.1 Graphene

To describe the electronic structure of graphene-based nanostructures we employ the tight-binding (TB) approximation, whereas to describe the phononic bandstructure we employ the Force Constant Method (FCM).

2.1.1 Electronic Structure

The empirical tight-binding model is a standard, convenient, and accurate method for calculating the electronic structure of semiconductors. It is also referred to as Bloch or linear combination of atomic orbitals (LCAO) method [31]. The Hamiltonian matrix for a simplified 2D system, using the TB method is described as follows: The 2D structure in Fig. 2.1 is composed of n_y chains of lattice points (i.e. atomic sites), each
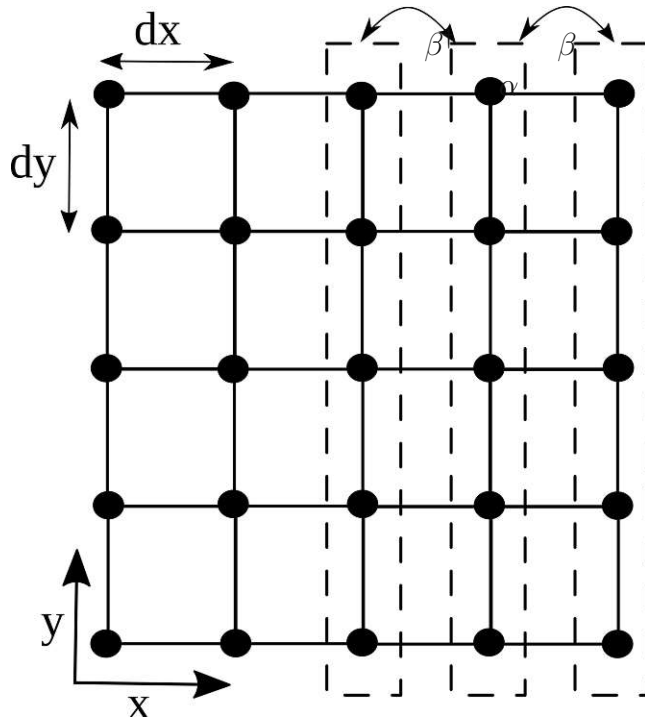
Figure 2.1: Two dimensional rectangular structure.

chain with n_x sides. Assuming that each point is represented by one basis orbital, the Hamiltonian matrix will have the size $(n_x n_y) \times (n_x n_y)$, and is given by:

$$H = \begin{pmatrix} \alpha & \beta & 0 & 0 & 0 & ... \\ \beta^\dagger & \alpha & \beta & 0 & 0 & ... \\ 0 & \beta^\dagger & \alpha & \beta & 0 & ... \\ \vdots & \vdots & \vdots & \vdots & \vdots & \vdots \\ ... & 0 & 0 & 0 & \beta^\dagger & \alpha \end{pmatrix}_{n_x n_y \times n_x n_y} \qquad (2.2)$$

where

$$\alpha = \begin{pmatrix} 2(t_x + t_y) & -t_y & 0 & 0 & 0 & ... \\ -t_y & 2(t_x + t_y) & -t_y & 0 & 0 & ... \\ 0 & -t_y & 2(t_x + t_y) & -t_y & 0 & ... \\ \vdots & \vdots & \vdots & \vdots & \vdots & \vdots \\ ... & 0 & 0 & 0 & -t_y & 2(t_x + t_y) \end{pmatrix}_{n_y \times n_y} \qquad (2.3)$$

14
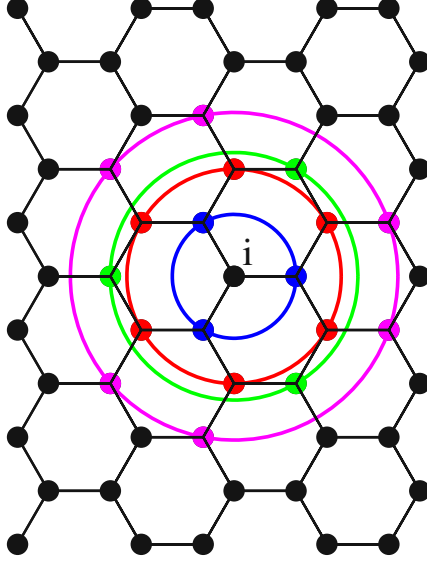
Figure 2.2: Schematic representation of the nearest neighbors of the ith carbon atom. Up to four nearest-neighbors are included.

and

$$\beta = \begin{pmatrix} -t_x & 0 & 0 & 0 & ... \\ 0 & -t_x & 0 & 0 & ... \\ \vdots & \vdots & \vdots & \vdots & \vdots \\ ... & ... & 0 & 0 & -t_x \end{pmatrix}_{n_y \times n_y} \qquad (2.4)$$

where the $[\alpha]_{n_y \times n_y}$ submatrix describes the coupling within each chain, and the $[\beta]_{n_y \times n_y}$ submatrix describes the coupling between the adjacent chains. In general, the size of these components would be $n_b \times n_b$, where n_b is the number of basis orbitals in each unit cell. The eigenvalues of H are the corresponding energies for the electrons in the structure and can be adjusted by fitting the parameters t_x and t_y. In the case of an open system, the boundary conditions are implemented by modifying the Hamiltonian to:

$$H = \begin{pmatrix} \alpha & \beta & 0 & ... & 0 & \beta^\dagger \\ \beta^\dagger & \alpha & \beta & 0 & 0 & ... \\ 0 & \beta^\dagger & \alpha & \beta & 0 & ... \\ \vdots & \vdots & \vdots & \vdots & \vdots & \vdots \\ \beta & 0 & ... & 0 & \beta^\dagger & \alpha \end{pmatrix}_{n_x n_y \times n_x n_y} \qquad (2.5)$$

The only change, here, is in the submatrices $H(1, n_x)$ and $H(n_x, 1)$, which now include the self energies of the left and right contacts. In the case of periodic boundary conditions, the bandstructure is calculated by considering the unit cell (index n) of the lattice, connected to the neighboring unit cells (index m) using the matrix elements

15
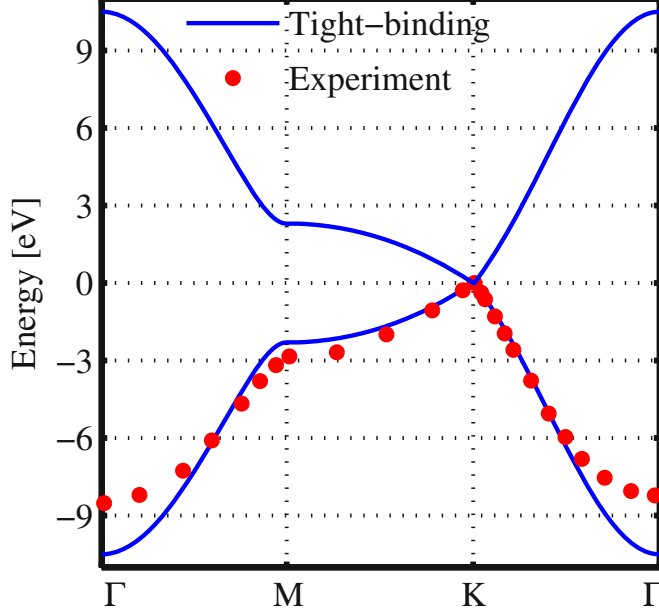
Figure 2.3: Electronic band structure of Graphene along the high-symmetry band line is calculated employing a third nearest tight binding approximation. Experimental results are taken from Ref. [33]

$[H_{nm}]$. For example, as indicated in the structure of Fig. 2.1, once periodic boundary conditions are applied along the x-axis, then $H_{nn} = \alpha$ and $H_{n,n+1} = \beta$ for all $n \in [1, n_x]$. The bandstructure of the lattice is then obtained by calculating the eigenvalues of the Hamiltonian as:

$$[h(k)] = \sum_m H_{nm} e^{i\vec{k}\cdot(\vec{d}_m - \vec{d}_n)} \tag{2.6}$$

for each $\vec{k}$-point in the Brillouin zone (BZ) [32]. Here, $\vec{d}_m$ is the vector corresponding to the position of neighboring unit cell m and the sum is over all neighboring unit cells.

In the case of graphene, a third nearest neighbor tight-binding model is used to describe its electronic structure. In this case, the particular atom i and its nearest neighbor atoms are shown in Fig. 2.2. The hopping parameter between two nearest atoms separated by distance a_{cc} is $t_1 = -3.2$ eV. The tight-binding parameter of the third-nearest neighbor atoms located $2a_{cc}$ away from each other is $t_3 = -0.3$ eV [34]. The hopping parameter for the second nearest-neighbor is assumed to be 0 eV. The bandstructure of graphene along the high-symmetry band line is shown in Fig. 2.3. The tight-binding results are in good agreement with experimental data taken from [33], in particular around the Fermi energy $E_F = 0$ which dominates the electrical properties. As shown in Ref. [34] this method can capture the details of the bandstructure of graphene-

Table 2.1: The fitting parameters of the force constant tensor in N/m for graphene [42].

N	Φ_r	Φ_{ti}	Φ_{to}
1	365.0	245.0	98.2
2	88.0	-32.3	-4.0
3	30.0	-52.5	1.5
4	-19.2	22.9	-5.8

based nanostructures. The tight-binding model with calibrated parameters provides band-gap and subband-edge energies in excellent agreement with first-principles calculations [34].

2.1.2 Phononic Structure

The phonon bandstructure can be described by first principle models [35, 36], the valence force field (VFF) method [37, 38], and the force constant method (FCM). The latter has the lowest computation time requirements. In this model, the dynamics of atoms are simply described by a few force springs connecting an atom to its surroundings up to given numbers of neighbors. In contrast, the VFF method is based on the evaluation of the force constants [39], which requires a much larger computational times. The FCM uses a small set of empirical fitting parameters and can be easily calibrated to experimental measurements. Despite its simplicity, it can provide accurate and transferable results [40, 41]. Thus, it is a convenient and robust method to investigate thermal properties of crystals and in particular of graphene nanostructures.

The FCM model we employ involves a fourth nearest-neighbor approximation (see Fig. 2.2). The force constant tensor describing the coupling between the ith and the jth carbon atom, which are the Nth nearest-neighbor of each other, is given by:

$$K_0^{(ij)} = \begin{pmatrix} \Phi_r^{(N)} & 0 & 0 \\ 0 & \Phi_{ti}^{(N)} & 0 \\ 0 & 0 & \Phi_{to}^{(N)} \end{pmatrix} \tag{2.7}$$

where, Φ_r, Φ_{ti} and Φ_{to} are the radial, the in-plane transverse, and the out-of-plane transverse components of the force constant tensor, respectively. Their values are presented in Table 2.1 [42].

The motion of the atoms can be described by a dynamic matrix as:

$$D = [D_{3\times3}^{(ij)}] = \left[\frac{1}{\sqrt{M_i M_j}} \times \begin{cases} K_{3\times3}^{(ij)} & , \quad i \neq j \\ -\sum_{l\neq i} K_{3\times3}^{(il)} & , \quad i = j \end{cases} \right] \tag{2.8}$$

where M_i is the atomic mass of the ith carbon atom, and K^{ij} is a 3×3 force constant tensor describing the coupling between the ith and the jth carbon atom. In Cartesian coordinates it is given by:

$$K^{(ij)} = U_m^{-1} K_0^{(ij)} U_m \tag{2.9}$$

where U_m is a unitary matrix defined as:

$$U_m = \begin{pmatrix} \cos\Theta_{ij} & \sin\Theta_{ij} & 0 \\ -\sin\Theta_{ij} & \cos\Theta_{ij} & 0 \\ 0 & 0 & 1 \end{pmatrix} \tag{2.10}$$

Here, we assume that the graphene sheet is located in the $x - y$ plane and that Θ_{ij} represents the angle between the x-axes and the bond between the ith and j^{th} carbon atom. The phononic bandstructure can be calculated by solving the eigenvalue problem described by:

$$\left(\sum_l K^{(il)} - \omega^2(\vec{q})I \right) \delta_{ij} - \sum_l K^{(il)} \exp\left(i\vec{q}\cdot\Delta\vec{r}_{il}\right) = 0 \tag{2.11}$$

where $\Delta\vec{r}_{ij} = \vec{r}_i - \vec{r}_j$ is the distance between the ith and the jth carbon atom, and $\vec{q}$ is the wave vector. Equivalently, after setting up the dynamic matrix, one can use the following eigen-value problem:

$$D + \sum_l D_l \exp\left(i\vec{q}.\Delta\vec{R}_l\right) - \omega^2(\vec{q})I = 0 \tag{2.12}$$

where D_l is the dynamic matrix representing the interaction between the unit cell and its neighboring unit cells separated by $\Delta\vec{R}_l$.

The phononic bandstructure of graphene shown in Fig. 2.4 is evaluated using the fourth nearest-neighbor FCM with force constants given in Table. 2.1. This method relies on twelve fitting parameters that determine the force constants, which are extracted from experiments. To validate the model, we present the experimental phonon bandstructure results from Refs. [40, 43]. As expected, the result is in good agreement with the experimental data (see Fig. 2.4), especially for the low phonon frequencies, which are the most important ones in determining the thermal conductivity.

Because the model relies on empirical parameters fitted to experiments, it is much more computationally efficient compared to other atomistic formalisms, such as the valence
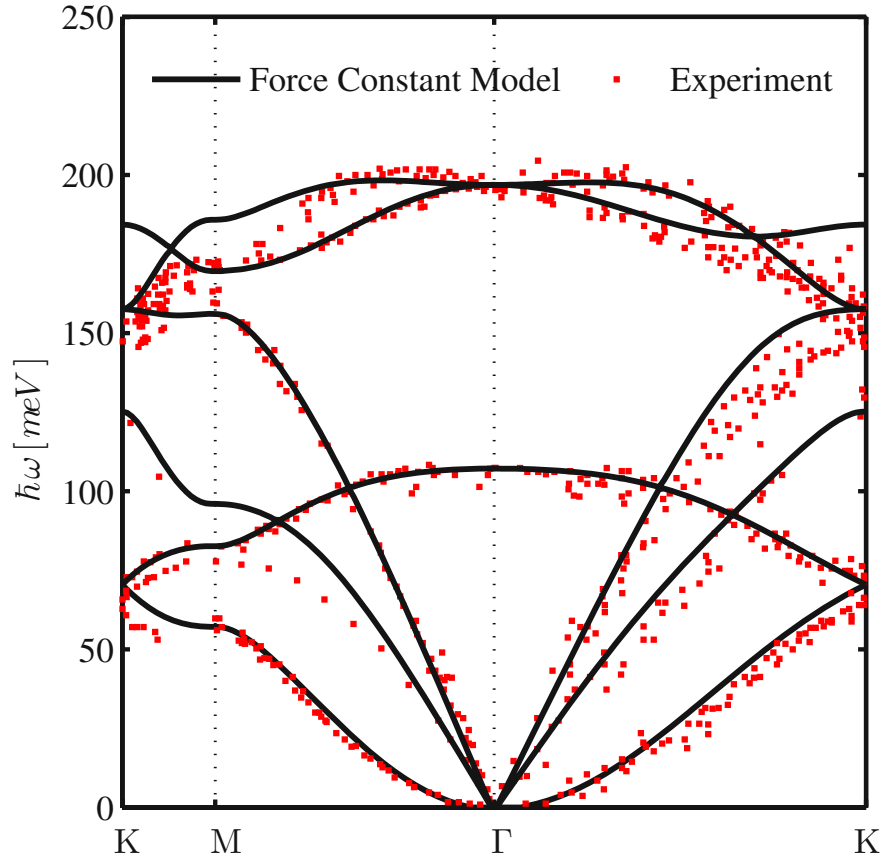
Figure 2.4: Phononic bandstructure of graphene (solid) evaluated using the fourth nearest-neighbor FCM. Experimental results (dots) are taken from Refs. [40, 43].

force field (VFF) method. In the VFF method, for example, the force constants for each atom in the unit cell are calculated, and the simulation time is dominated by the dynamic matrix construction [39]. The approximation in that method comes from the parameters used in the evaluation of the potential energy. For FCM, since force constants are empirical parameters, the construction time of the dynamic matrix is negligible, which makes the computation much more efficient. The simulation time is determined by the solution of the eigenvalue problem. In the graphene lattice this results in 18 neighbors for each atom as shown in Fig. 2.2. In FCM we assume that there is a spring between each carbon atom and its 18 neighbors. This number is reduced in the case of boundary atoms with less nearest-neighbors.

2.2 Silicon

To calculate the electronic and phononic structures of silicon-based nanostructures, one can employ the atomistic $sp^3d^5s^*$ tight-binding method [44] and the modified valence force field method [45], respectively.

2.2.1 Electronic Structure

As proposed by Slater in 1954, the bandstructure of silicon (as well as that of other diamond-like semiconductors) can be calculated using the sp^3 tight-binding method. This method considers four valence orbitals $3s$ and $3p^3$, including $3p_x$, $3p_y$, and $3p_z$, for each silicon atom [31]. To enhance accuracy for reproducing the conduction band of diamond and zinc blende semiconductors, it is common to use the sp^3s^* tight-binding method in which the first excited s-like orbital s^* (i.e. $4s$ in the case of silicon) is also included [46]. It was further improved by including the five excited d orbitals $4d^5$ in the so called $sp^3d^5s^*$ tight-binding method. This method includes ten orbitals per silicon atom.

We first consider the $sp^3d^5s^*$ tight-binding method without spin-orbit coupling for bulk silicon, the unitcell of which consists of two atoms commonly called the anion and the cation. Each anion atom is connected to four cation atoms through for bonds B_1, B_2, B_3, and B_4 and vice versa. The Hamiltonian of the unitcell, when considering the coupling of the anion with only one neighboring cation, consists of four blocks as:

$$H = \begin{bmatrix} H_{aa} & H_{ac} \\ H_{ca} & H_{cc} \end{bmatrix} \tag{2.13}$$

Here, H_{aa} and H_{cc} represent the on-site terms and $H_{ac} = H_{ca}^\dagger$ the coupling between two atoms. In the case of silicon, we note that $H_{aa} = H_{cc}$ as the unitcell consists of two similar silicon atoms. The on-site term is a diagonal matrix:

$$H_{aa} = [E_{i,j}\delta_{i,j}] \tag{2.14}$$

and the coupling term has the form of:

$$H_{ac} = [g_{i,j}^B V_{i,j}^{ac}] \tag{2.15}$$

where i and j run over all 10 orbital indexes:

$$s, p_x, p_y, p_z, d_{xy}, d_{yz}, d_{zx}, d_{x^2-y^2}, d_{z^2-r^2} \tag{2.16}$$

The $g_{i,j}^B$ in Eq. 2.15 are taken from a sign matrix [47] and depend on the corresponding bond (B) between the anion and the cation. The matrix elements $V_{i,j}^{ac}$ are formed as

$$V_{i,j}^{ac} = f_{i,j}(l, m, n)V_{u,v} \tag{2.17}$$

where $f_{i,j}(l, m, n)$ are the two center Slater-Koster energy integrals [31]. $V_{u,v}$ and $E_{i,j}$ are fitting parameters used to correctly capture the details of bandstructure over the entire Brillouin zone. Values are provided in Ref. [44] for silicon.

To describe the top of the valence band correctly, one needs to include the spin-orbit coupling [32]. In this case, the number of orbitals per atom increases to 20 [44, 47]. However, the spin-orbit interactions affect only orbitals with different spins of the same atom. Therefore, they are only added to the diagonal blocks H_{aa}, and H_{cc} of the Hamiltonian [47].

2.2.2 Phononic Structure

For the calculation of the phononic bandstructure of silicon-based nanostructures, we employ the modified valence force filed method [45]. In this method the interatomic potential is modeled by the following bond deformations: bond stretching, bond bending, cross bond stretching, cross bond bending stretching, and coplanar bond bending interactions [45]. The model accurately captures the bulk silicon phonon spectrum as well as the effects of confinement [39]. In the MVFF method, the total potential energy of the system is defined as [39]:

$$U \approx \frac{1}{2} \sum_{i \in N_A} \left[\sum_{j \in nn_i} U_{\text{bs}}^{ij} + \sum_{j,k \in nn_i}^{j \neq k} \left(U_{\text{bb}}^{jik} + U_{\text{bs-bs}}^{jik} + U_{\text{bs-bb}}^{jik} \right) + \sum_{j,k,l \in COP_i}^{j \neq k \neq l} U_{\text{bb-bb}}^{jikl} \right] \quad (2.18)$$

where N_A, nn_i, and COP_i are the number of atoms in the system, the number of the nearest neighbors of a specific atom i, and the coplanar atom groups for atom i, respectively. As shown in Fig. 2.5, U_{bs}, U_{bb}, $U_{\text{bs-bs}}$, $U_{\text{bs-bb}}$, and $U_{\text{bb-bb}}$ are the bond stretching, bond bending, cross bond stretching, cross bond bending stretching, and coplanar bond bending interactions, respectively [39, 45]. The terms $U_{\text{bs-bs}}$, $U_{\text{bs-bb}}$, and $U_{\text{bb-bb}}$ are an addition to the usual Keating valence force filed (KVFF) model [48], which can only capture the silicon phononic bandstructure in a limited part of the Brillouin zone. As indicated in Ref. [39] the introduction of these additional terms provides a more accurate description of the entire Brillouin zone.

These short-range interactions depends on the atomic positions by [39]:

$$U_{\text{bs}}^{ij} = \frac{3}{8} \alpha_{ij} \frac{\left(r_{ij}^2 - d_{ij}^2 \right)^2}{d_{ij}^2} \quad (2.19)$$

$$U_{\text{bb}}^{ij} = \frac{3}{8} \beta_{jik} \frac{\left(\Delta \theta_{jik} \right)^2}{d_{ij} \ d_{ik}} \quad (2.20)$$

$$U_{\text{bs-bs}}^{ij} = \frac{3}{8} \delta_{jik} \frac{\left(r_{ij}^2 - d_{ij}^2 \right) \left(r_{ik}^2 - d_{ik}^2 \right)}{d_{ij} \ d_{ik}} \quad (2.21)$$
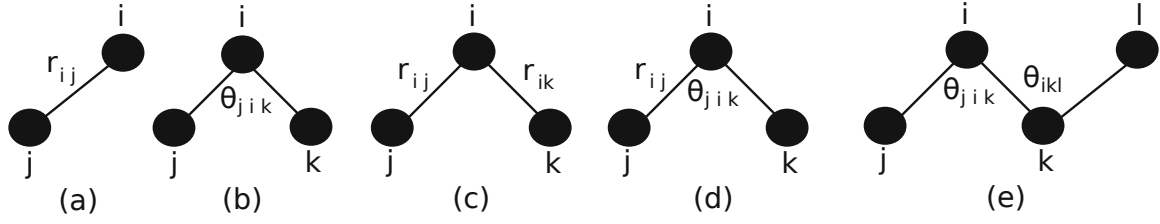
Figure 2.5: Schematic representation of (a) bond-stretching, (b) bond bending, (c) cross bond stretching, (d) cross bond bending-stretching, and (e) coplanar bond bending interactions.

Table 2.2: The force constant fitting parameters for silicon in N/m.

Model	α	β	δ	γ	ν
KVFF [48]	48.5	13.8	0	0	0
MVFF [45]	49.4	4.79	5.2	0.0	6.99

$$U_{\text{bs}-\text{bb}}^{ij} = \frac{3}{8}\gamma_{jik}\frac{\left(r_{ij}^2 - d_{ij}^2\right)(\Delta\theta_{jik})}{d_{ij}\ d_{ik}} \tag{2.22}$$

$$U_{\text{bb}-\text{bb}}^{ij} = \frac{3}{8}\sqrt{\nu_{jik}\nu_{ikl}}\frac{(\Delta\theta_{jik})(\Delta\theta_{ikl})}{\sqrt{d_{ij}\ d_{ik}^2\ d_{kl}}} \tag{2.23}$$

where $\vec{r}_{ij}$ and $\vec{d}_{ij}$ are the non-equilibrium and equilibrium bond vectors from atom i to atom j, respectively. The angle deviation of bonds between i and j, and i and k is defined by $\Delta\theta_{jik} = \vec{r}_{ij} \cdot \vec{r}_{ik} - \vec{d}_{ij} \cdot \vec{d}_{ik}$. The fitting parameters of silicon α, β, δ, γ, and ν are presented in Table 2.2 for both KVFF and MVFF models.

The total potential energy is zero when all the atoms are located in their equilibrium position. Under the harmonic approximation, the motion of atoms can be described by a dynamic matrix as:

$$D = \left[D_{3\times3}^{ij}\right] = \left[\frac{1}{\sqrt{M_i M_j}} \times \begin{cases} D_{ij} & , \ i \neq j \\ -\sum_{l\neq i} D_{il} & , \ i = j \end{cases}\right] \tag{2.24}$$

where dynamic matrix component between atoms i and j is given by [39]:

$$D_{ij} = \begin{bmatrix} D_{ij}^{xx} & D_{ij}^{xy} & D_{ij}^{xz} \\ D_{ij}^{yz} & D_{ij}^{yy} & D_{ij}^{yz} \\ D_{ij}^{zx} & D_{ij}^{zy} & D_{ij}^{zz} \end{bmatrix} \tag{2.25}$$
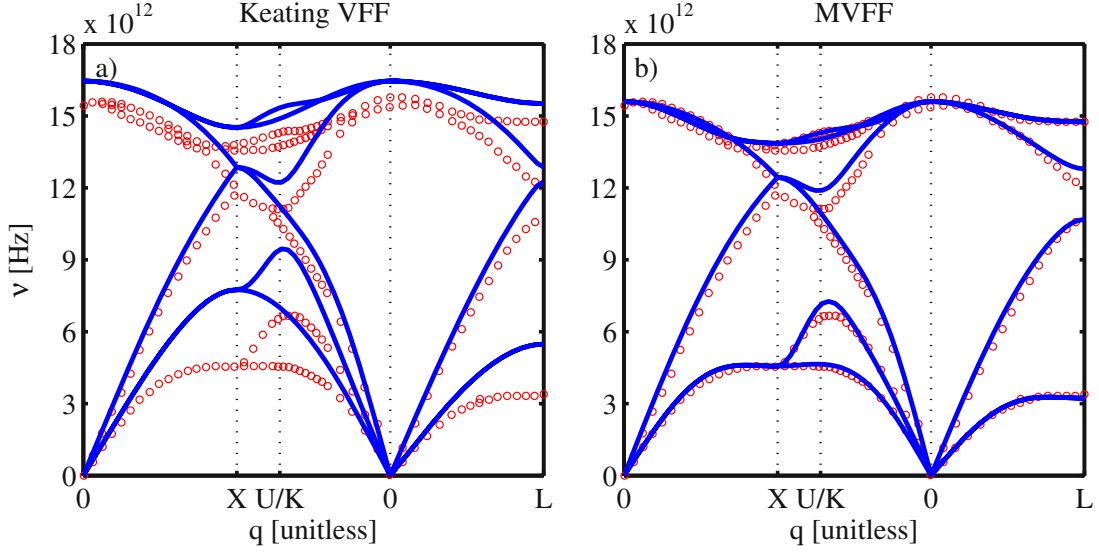
Figure 2.6: Phononic bandstructure of bulk silicon (solid) evaluated using (a) Keating VFF and (b) MVFF. Experimental results (circles) are taken from Ref. [49].

and

$$D_{ij}^{mn} = \frac{\partial^2 U_{\text{elastic}}}{\partial r_m^i \partial_n^j}, \qquad i,j \in N_{\text{A}} \text{ and } m,n \in [x,y,z] \qquad (2.26)$$

is the second derivative of the potential energy with respect to the displacement of atom i along the m-axis and atom j along the n-axis. U_{elastic} is the potential associated with the motion of only two atoms i and j, whereas the other atoms are considered frozen (unlike U, which is the potential when all atoms are allowed to move out of their equilibrium position). To compute U_{elastic}: 1) We start with U from Eq. 2.18. 2) We fix the positions of all atoms except atoms i and j. 3) We compute the inter-atomic potential due to all bond deformations that result from interaction between both of these two atoms, and sum them up to obtain U_{elastic}. All other inter-atomic potential terms that result from interactions due to atom i alone, or atom j alone, are not considered, since all double derivatives taken with respect to $\partial^2/\partial r_m^i \partial_n^j$, give zero. After setting up the dynamic matrix, the eigenvalue problem can be set up according to Eq. 2.12, the solution of which is the phononic dispersion. Figure 2.6 compares the bulk silicon dispersions calculated using the KVFF and MVFF models with experimental data taken from Ref. [49]. The KVFF fails in some part of the Brillouin zone, whereas the MVFF with three additional terms provides a more accurate description of the entire Brillouin zone.

2.3 Electron Transport

To calculate the electron transport properties, the Landauer approach [50] is used for both ballistic and diffusive regimes.

2.3.1 Landauer Formula

According to the Landauer formalism [51], the electric current can be calculated using the electronic transmission function $\overline{T}_{\mathrm{el}}(E)$:

$$I = \frac{2e}{h} \int_{-\infty}^{+\infty} \overline{T}_{\mathrm{el}}(E) \left[f_{\mathrm{s}}(E) - f_{\mathrm{d}}(E) \right] \, dE \tag{2.27}$$

Here, $f_{\mathrm{s,d}}(E)$ are the Fermi distribution functions of the source and drain contacts, respectively. In the linear response regime, the electrical current is proportional to the applied voltage:

$$I = \frac{2e^2 \Delta V}{h} \int_{-\infty}^{+\infty} \overline{T}_{\mathrm{el}}(E) \left(-\frac{\partial f}{\partial E} \right) \, dE = G \Delta V \tag{2.28}$$

where the electrical conductance G is defined as:

$$G = \frac{2e^2}{h} \int_{-\infty}^{+\infty} \overline{T}_{\mathrm{el}}(E) \left(-\frac{\partial f}{\partial E} \right) \, dE \tag{2.29}$$

The derivative of the Fermi function:

$$-\frac{\partial f}{\partial E} = \frac{1}{4k_{\mathrm{B}}T} \left[\cosh \left(\frac{E - E_{\mathrm{F}}}{2k_{\mathrm{B}}T} \right) \right]^{-2} \tag{2.30}$$

is known as the thermal broadening function, where E_{F} is the Fermi-level of the system. It has a width of a few $k_{\mathrm{B}}T$ around E_{F}, indicating that electrons around the Fermi energy have a major contribution to the electrical current.

Other than the applied voltage, a temperature difference can also result in a flow of charge carriers, as explained in Chapter 1. In the linear response regime, the electrical and heat currents are proportional to the applied voltage, when the temperature difference is zero. They are also proportional to the temperature difference, if there is no applied voltage. These currents are expressed as:

$$I = G \Delta V + \overline{SG} \Delta T \tag{2.31}$$

$$I_q = -T \overline{SG} \Delta V - K_0 \Delta T \tag{2.32}$$

where I and I_q are the electric and the heat current, respectively. Here, K_0 is the electronic contribution to the thermal conductivity for zero electric field, defined as [52]:

$$K_0 = \frac{2}{hT} \int_{-\infty}^{+\infty} \overline{T}_{\text{el}}(E)\,(E - E_{\text{F}})^2 \left(-\frac{\partial f}{\partial E}\right)\, dE \tag{2.33}$$

As we show later, the proportionality factor of the temperature difference ΔT in Eq. 2.31 is equal to the product SG, where S is the Seebeck coefficient and G is the electrical conductance. We represent this factor by $\overline{SG}$. Similarly, the proportionality factor of ΔV in Eq. 2.32 is represented by $-T\overline{SG}$. Eqs. 2.31 and 2.32 can be rewritten as [30, 52]:

$$\Delta V = I/G - S\Delta T \tag{2.34}$$

$$I_q = \Pi I - K_{\text{el}}\Delta T \tag{2.35}$$

where $\Pi = -TS$ is the Peltier coefficient and

$$K_{\text{el}} = K_0 - TS^2 G \tag{2.36}$$

The Seebeck coefficient can be evaluated by $S = \overline{SG}/G$ as [52]:

$$S = \frac{1}{-eT} \frac{\int_{-\infty}^{+\infty} \overline{T}_{\text{el}}(E)(E - E_{\text{F}})\left(-\frac{\partial f}{\partial E}\right) dE}{\int_{-\infty}^{+\infty} \overline{T}_{\text{el}}(E)\left(-\frac{\partial f}{\partial E}\right) dE} \tag{2.37}$$

2.3.2 Transmission Function

An important material property of a semiconductor is the density of states (DOS). The DOS of a system indicates the number of states per energy interval and per volume. The analytical descriptions for the DOS of an isotropic material can be easily calculated [32, 53]. However, the bandstructure of materials is not always isotropic. Especially in low dimensional materials, the electronic structure is affected by confinement and several complex features appear. Numerical approaches in the calculation of the DOS are necessary, and depending on the sophistication of the numerical model employed, most of the electronic structure properties are usually captured accurately [32].

If $\varepsilon_\alpha(\vec{k})$ denotes the bandstructure, where α indicates the band number and $\vec{k}$ is the wave vector, then the number of states with energy smaller than E is [32]:

$$N(E) = \sum_{\alpha, \vec{k}} \vartheta \left(E - \varepsilon_\alpha(\vec{k})\right) \tag{2.38}$$

where ϑ is the unit step function. Therefore, the DOS is calculated by:

$$D(E) = \frac{1}{\Omega} \frac{dN(E)}{dE} = \frac{1}{\Omega} \sum_{\alpha,\vec{k}} \delta\left(E - \varepsilon_\alpha(\vec{k})\right) \tag{2.39}$$

where δ is the Dirac-delta function and Ω the volume. In the case of two- and one-dimensional systems, the volume is replaced by the area A and the length L, respectively. For numerical stability, in order to obtain a continuous DOS, a broadening through a Lorentzian function is employed, instead of the sharp delta function [32]:

$$\delta\left(E - \varepsilon_\alpha(\vec{k})\right) \Longrightarrow \frac{\gamma/2\pi}{\left(E - \varepsilon_\alpha(\vec{k})\right)^2 + (\gamma/2)^2} \tag{2.40}$$

where the broadening parameter to be used $\gamma = 0.3$ meV is similar to the energy spacing between the various states.

Another important ballistic quantity is the number of subbands or modes. The transmission function $\overline{T}_{\mathrm{el}}(E)$ is, indeed, the multiplication of the number of modes $M(E)$ and transmission probability $T_{\mathrm{el}}(E)$:

$$\overline{T}_{\mathrm{el}}(E) = M_{\mathrm{el}}(E)T_{\mathrm{el}}(E) \tag{2.41}$$

In the ballistic regime, the transmission of each subband is one and, therefore, the number of modes represents the ballistic transmission function. To calculate $M_{\mathrm{el}}(E)$, it is enough to count the number of modes at a given energy:

$$\begin{aligned}
\overline{T}_{\mathrm{el}}(E)|_{\mathrm{Ballistic}} = M_{\mathrm{el}}(E) &= \sum_{\alpha,k_\perp} \vartheta\left(E - \min\left[\varepsilon_\alpha(k_\perp)\right]\right) - \vartheta\left(E - \max\left[\varepsilon_\alpha(k_\perp)\right]\right) \\
&= \frac{1}{2} \sum_{\alpha,\vec{k}} \delta\left(E - \varepsilon_\alpha(\vec{k})\right) \Delta k_\perp \frac{\partial \varepsilon_\alpha(\vec{k})}{\partial k_\parallel}
\end{aligned} \tag{2.42}$$

where $k_\perp$ refers to the wave vector component perpendicular to the transport direction and $k_\parallel$ to the wave vector component parallel to the transport direction [30, 32, 52]. Finally, we mention that the group velocity of an electron in a Bloch state is defined as:

$$\vec{v}_{g,\alpha}(\vec{k}) = \frac{1}{\hbar} \vec{\nabla}_k \varepsilon_\alpha(\vec{k}) \tag{2.43}$$

The prefactor $1/2$ in Eq. 2.42 is used since only states with positive group velocities along the transport direction contribute to the conductance:

$$v_{g,\parallel} = \frac{1}{\hbar} \frac{\partial \varepsilon_\alpha(\vec{k})}{\partial k_\parallel} > 0 \tag{2.44}$$

A typical test-case bandstructure and the way of counting the modes is shown in Fig. 2.7.
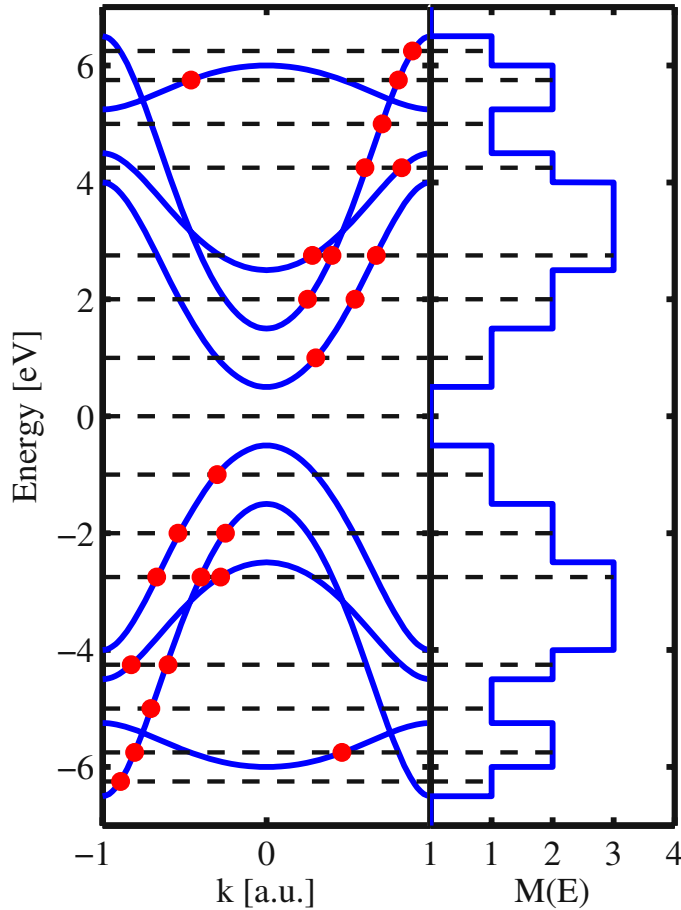
Figure 2.7: A typical bandstructue and its corresponding number of modes at some energies.

In the presence of scattering processes, the transmission probability T_{el} is less than one. To include scattering effects, several transport approaches are commonly used, such as the linearized Boltzmann transport equation, Monte Carlo simulations for solutions of the Boltzmann equation beyond the linear regime, the scattering-matrix method, and the non-equilibrium Green's function (NEGF) method. From all these methods, only the quantum mechanical NEGF method is able to capture the wave nature of electrons. It is also able to take into account the atomistic details of actual boundaries and surfaces and capture boundary scattering in nanostructures [32,54].

We use the NEGF method to study the effect of boundary scattering on the electronic transmission of one-dimensional graphene-based structures. For these simulations, the system is assumed to consist of three sections: the channel, the source contact, and the drain contact. The boundary scattering mechanism is introduced in the channel by physically distorting the boundaries. The contacts are assumed to be pristine and always at equilibrium. To describe the electronic structure of this system, the

Hamiltonian matrix is set up using the third nearest neighbor tight-binding method as described in Sec. 2.1.1. The system can be described using the following matrices [32]: i) $[H_{ch}]_{n_{ch} \times n_d}$ is the Hamiltonian matrix of the channel (device Hamiltonian), ii) $[H_{s/d}]_{n_R \times n_R}$ is the Hamiltonian of the source and drain contacts (reservoirs), and iii) the couplings between the unit cells of the device $[\tau_{s/d}]_{n_d \times n_R}$. Here, n_{ch} and n_R indicate the number of basis orbitals in the channel and contacts, respectively. In the NEFG method, the contacts are described through the self-energy matrices:

$$\Sigma_{s/d} = \tau_{s/d} G_{s/d} \tau_{s/d}^{\dagger} \tag{2.45}$$

where

$$G_{s/d} = \left[E I_{n_R \times n_R} - H_{s/d} + i0^{+} I_{n_R \times n_R} \right]^{-1} \tag{2.46}$$

is the Green's function for the isolated contacts. $I_{n_R \times n_R}$ is an identity matrix of the size of the contacts. The device (channel) Green's function can then be calculated as [32]:

$$G_{ch}(E) = [E I_{n_d \times n_d} - H_{ch} - \Sigma_s - \Sigma_d]^{-1} \tag{2.47}$$

The transmission function can be calculated as:

$$\overline{T}_{\text{el}}(E) = \text{Trace}[\Gamma_s G_{ch} \Gamma_d G_{ch}] \tag{2.48}$$

where the broadening matrices are defined as:

$$\Gamma_{s/d} = i \left[\Sigma_{s/d} - \Sigma_{s/d}^{\dagger} \right] \tag{2.49}$$

Finally, it is worth mentioning that in NEGF formalism scattering processes are included using some additional self-energy functions [32]. However, in this thesis, we only investigate the effect of roughness scattering (as the dominant scattering event in nanostructures), which can directly be included in H_{ch} through missing atoms at the edges.

2.3.2.1 Surface Green's Function

To calculate the properties of the channel, we assume semi-infinite contacts. Using the NEGF formalism, these contacts yield a finite surface energy [32, 55]. The channel couples with only a finite number of surface atoms in the contacts that contain, however, the information of entire semi-infinite lead. Therefore, since most of the elements in $\tau_{s/d}$ are zero, the matrices can be reduced to smaller ones, β and $\beta^{\dagger}$, which only contain the couplings between neighboring unit cells. In this case, the first elements of the Hamiltonian that contain the information of a unit cell, α, is used to describe the first section/unit cell of the contact, whereas the rest of the contacts can be modeled by self-energy matrices. Due to the periodicity of the semi-infinite contacts, the

surface Green's function can be calculated iteratively as:

$$g_{\text{surface}}(E) = \left[EI_{n_b \times n_b} - \alpha - \beta g_{\text{surface}} \beta^\dagger \right]^{-1} \tag{2.50}$$

where n_b is the number of orbital bases in the unit cell. The size of g_s can be further reduced to the number of surface atoms in the contact that couple to the channel atoms, and not the atoms of the entire unit cell, which simplifies computation significantly. To solve the non-linear matrix equation 2.50 different algorithms have been proposed [55]. One of the most efficient one is the Sancho-Rubio method [56]. After obtaining the surface Green's function, one can easily calculate the corresponding self-energy matrix as:

$$\Sigma = \beta g_{\text{surface}} \beta^\dagger \tag{2.51}$$

2.4 Phonon Transport

To calculate the thermal conductivity, we employ non-equilibrium Green's function for phonons in conjunction with the Landauer formula for graphene-based nanostructures and Boltzmann transport equation for phonons for silicon-based materials.

2.4.1 Landauer Formula

In semiconductors, the largest component of the heat current is due to the phonon transport. Using the Landauer theory for phonon transport, the heat flow is proportional to the phonon transmission function $\overline{T}_{\text{ph}}(\omega)$, the Bose-Einstein distribution function $n(\omega)$ of source and drain contacts, and the phonon energy/frequency ω as:

$$I_q = \frac{1}{h} \int_0^{+\infty} \overline{T}_{\text{ph}}(\omega) \hbar\omega \left[n_s(\omega) - n_d(\omega) \right] \; d(\hbar\omega) \tag{2.52}$$

In the linear response regime of the Landauer theory the heat current is proportional to the temperature difference by:

$$\begin{aligned}
I_q &= \frac{1}{h} \int_0^{+\infty} \overline{T}_{\text{ph}}(\omega) \hbar\omega \Delta T \frac{[n_s(\omega) - n_d(\omega)]}{\Delta T} \; d(\hbar\omega) \\
&= \frac{\Delta T}{h} \int_0^{+\infty} \overline{T}_{\text{ph}}(\omega) \hbar\omega \frac{\partial n(\omega)}{\partial T} \; d(\hbar\omega)
\end{aligned} \tag{2.53}$$

This can alternatively be written as:

$$I_q = -\Delta T \frac{k_B^2 T \pi^2}{3h} \int_0^{+\infty} \overline{T}_{\text{ph}}(\omega) W_{\text{ph}}(\hbar\omega) \; d(\hbar\omega) \tag{2.54}$$

where the phononic window function is given by [57]:

$$W_{\mathrm{ph}}(\hbar\omega) = -\frac{3}{\pi^2}\left(\frac{\hbar\omega}{k_{\mathrm{B}}T}\right)^2\frac{\partial n}{\partial(\hbar\omega)}$$
$$= \frac{3}{4\pi^2 k_{\mathrm{B}}T}\left(\frac{\hbar\omega}{k_{\mathrm{B}}T}\right)^2\left[\sinh\left(\frac{\hbar\omega}{2k_{\mathrm{B}}T}\right)\right]^{-2} \tag{2.55}$$

As $I_q = -K_{\mathrm{ph}}\Delta T$, one can express the lattice contribution to the thermal conductance as [58]:

$$K_{\mathrm{ph}} = \frac{k_{\mathrm{B}}^2 T\pi^2}{3h}\int_0^{+\infty}\overline{T}_{\mathrm{ph}}(\omega)W_{\mathrm{ph}}(\omega)d(\hbar\omega) \tag{2.56}$$

To extract the ballistic phonon transmission $\overline{T}_{\mathrm{ph}}(E)$ in Eq. 2.56, similar to the electronic quantities (Eqs. 2.39-2.42), the phononic density of modes $M_{\mathrm{Ph}}(E)$ is calculated using the phononic bandstructures, where $E = \hbar\omega$ denotes the energy of a phonon with frequency ω. In our calculations for phonon density of states DOS_{ph}, we broadened the delta function by 1 meV. This helps to numerically smoothen the DOS function, without affecting the thermal conductance calculations.

The FCM can also be effectively coupled to NEGF for the investigation of coherent phonon transport in low dimensional systems. The NEGF method has been traditionally employed for electronic transport studies, but has been extended to phonon studies as well [54]. Here, the phononic device Green's function is obtained by

$$G(E) = \left(E^2 I - D - \Sigma_s - \Sigma_d\right)^{-1} \tag{2.57}$$

where D is device dynamic matrix and $E = \hbar\omega$ is the phonon energy [59]. Note that this is a Green's function of a classical wave equation, which is second order in time. Therefore, the square of the energy appears in Eq. 2.57. This is in contrast to the Schrodinger equation for quantum treatment of electrons which is first order in time, such that the eigen energy E appears linearly in that case.

Finally, similar to the electron transport, the transmission probability of phonons through the rough channel can then be calculated using:

$$\overline{T}_{\mathrm{ph}}(E) = \mathrm{Trace}[\Gamma_s G\Gamma_d G^\dagger] \tag{2.58}$$

Here, the phononic broadening and contact self-energy matrices are obtained in a similar way as the electronic ones (Eq. 2.51) with the substitutions $H \rightarrow D$ and $E \rightarrow \hbar^2\omega^2$.

2.4.2 Boltzmann Transport Equation

At equilibrium, the distribution of phonons in branch α and wavevector $\vec{q}$ is given by the Bose-Einstein distribution function $n(\omega)$:

$$n\left(\omega_\alpha(\vec{q})\right) = \frac{1}{e^{\hbar\omega_\alpha(\vec{q})/k_B T} - 1} \tag{2.59}$$

Under non-equilibrium conditions, the distribution of phonons deviates from its equilibrium distribution, and transport of phonons is computed using the Boltzmann transport formalism. The non-equilibrium distribution function $\overline{n}(t,\vec{r},\omega)$, in general, is a function of time t and position $\vec{r}$. The BTE can be written as:

$$\frac{\partial\overline{n}}{\partial t} + \vec{v}\cdot\nabla_{\vec{r}}\overline{n} = \left(\frac{\partial\overline{n}}{\partial t}\right)_{\text{scat}} \tag{2.60}$$

and for the steady state:

$$\vec{v}\cdot\nabla_{\vec{r}}\overline{n} = \left(\frac{\partial\overline{n}}{\partial t}\right)_{\text{scat}} \tag{2.61}$$

Under a temperature gradient, the BTE can be written as [60]:

$$\vec{v}\cdot\nabla_{\vec{r}}T\frac{\partial\overline{n}}{\partial T} = \left(\frac{\partial\overline{n}}{\partial t}\right)_{\text{scat}} \tag{2.62}$$

In the relaxation time approximation, the change of the distribution function due to the scattering events can be given by:

$$\left(\frac{\partial\overline{n}}{\partial t}\right)_{\text{scat}} = \frac{n - \overline{n}}{\tau_\alpha(\vec{q})} \tag{2.63}$$

and therefore

$$\vec{v}\cdot\nabla_{\vec{r}}T\frac{\partial\overline{n}}{\partial T} = \frac{n - \overline{n}}{\tau_\alpha(\vec{q})} \tag{2.64}$$

where $\tau_\alpha(\vec{q})$ is the relaxation time of phonons of frequency $\omega_\alpha(\vec{q})$. In this work we use a linearized form of Eq. 2.64, which assumes that the temperature gradient causes only a small deviation from Bose-Einstein distribution function [61, 62], so that:

$$\frac{\partial\overline{n}}{\partial T} \approx \frac{\partial n}{\partial T} = \frac{\hbar\omega_\alpha(\vec{q})}{k_B T^2}n(n+1) \tag{2.65}$$

and

$$\overline{n} = \frac{1}{e^{(\hbar\omega_\alpha(\vec{q}) - \Psi_\alpha(\vec{q}))/k_B T} - 1} \approx n - \Psi_\alpha(\vec{q})\left(\frac{\partial n}{\partial(\hbar\omega)}\right) = n + \frac{\Psi_\alpha(\vec{q})n(n+1)}{k_B T} \tag{2.66}$$

where $\Psi_\alpha(\vec{q})$ shows the deviation from the equilibrium distribution. Then, one may eliminate the temperature gradient using $\Psi_\alpha(\vec{q}) = -\psi_\alpha(\vec{q})\nabla_{\vec{r}}T$ and write:

$$\overline{n} = n - \frac{n(n+1)}{k_{\mathrm{B}}T}\psi_\alpha(\vec{q})\nabla_{\vec{r}}T \tag{2.67}$$

Since the equilibrium distribution does not carry any heat flux, the heat flux equals to [62]:

$$I_{\mathrm{q}} = \sum_{\alpha,\vec{q}} \hbar\omega(\overline{n}-n)v_\alpha(\vec{q}) = -\sum_{\alpha,\vec{q}} \hbar\omega v_\alpha(\vec{q})\frac{n(n+1)}{k_{\mathrm{B}}T}\psi_\alpha(\vec{q})\nabla_{\vec{r}}T \tag{2.68}$$

On the other hand, it holds the differential form of Fourier's law:

$$I_{\mathrm{q}} = -\kappa_l \nabla T \tag{2.69}$$

Therefore, one can obtain the lattice thermal conductivity as:

$$\kappa_l = \sum_{\alpha,\vec{q}} \hbar\omega v_\alpha(\vec{q})\frac{n(n+1)}{k_{\mathrm{B}}T}\psi_\alpha(\vec{q}) \tag{2.70}$$

Under the single-mode relaxation time (SMRT) approximation [62], $\psi_\alpha(\vec{q})$ follows from the linearized BTE (Eqs. 2.64-2.66) as:

$$\psi_\alpha(\vec{q}) = \frac{\hbar\omega_\alpha(\vec{q})}{T}v_\alpha(\vec{q})\tau_\alpha(\vec{q}) \tag{2.71}$$

Here, $\tau_\alpha(\vec{q})$ is the scattering time in SMRT approximation. Therefore, Eq. 2.70 becomes

$$\kappa_l = \sum_{\alpha,\vec{q}} \hbar\omega v_\alpha(\vec{q})^2\tau_\alpha(\vec{q})\frac{\partial n}{\partial T} \tag{2.72}$$

32

3 Thermoelectric Properties of Graphene-Based Nanostructures

Graphene, a recently discovered form of carbon, has received much attention over the past few years due to its excellent electrical, optical, and thermal properties [22]. The electrical conductance of graphene is as high as that of copper [23]. As a zero band-gap material, pristine graphene has a small Seebeck coefficient [24]. However, one can open up band-gaps by appropriate patterning of the graphene sheets [25–27]. Graphene nanoribbons (GNRs) are thin strips of graphene, where the band gap is varied by the chirality of the edge and the width of the ribbon. Zigzag GNRs show metallic behavior, whereas armchair GNRs are semiconductors with a band-gap inversely proportional to the width [25]. Very recently, Zhang and coworkers showed that one can open up a significant band-gap in zigzag GNRs by edge manipulation [63]. In addition, it has been theoretically [64] and experimentally [65] shown that by introducing an array of holes into the graphene sheet a band-gap can be achieved. On the other hand, a large scale method to produce graphene sheets has been reported [30]. Experimental studies have also reported a high Seebeck coefficient in graphene-based devices [66, 67].

The high Seebeck coefficient has been achieved by applying voltages (e.g. gate voltage) and magnetic field to the graphene-based devices. The applied voltage is normally used for breaking the symmetry between electron and hole conduction. Without applying a voltage, the symmetry between valence and conduction bands results in a low Seebeck coefficient, and as a result a relatively small thermoelectric power factor for pristine graphene. The thermoelectric figure of merit, however, can be further improved by degrading the lattice thermal conductivity. This was also experimentally demonstrated for traditionally poor thermoelectric materials such as silicon which resulted in ZT values close to $ZT \sim 0.5$, a large improvement compared to $ZT = 0.01$ of bulk silicon [17].

The ability of graphene to conduct heat is an order of magnitude higher than that of copper [28]. The high thermal conductance of graphene is mostly due to the lattice contribution, whereas the electronic contribution to the thermal conduction can be ignored [28, 29]. Therefore, for thermoelectric applications it is necessary to reduce its thermal conductance. By proper engineering the phonon transport properties it is possible to reduce the total thermal conductance without significant reduction of the electrical conductance and the power factor.

Recently many theoretical studies have been performed on the thermal conductivity of graphene-based structures. It has been shown that boundaries and edge roughness can strongly influence the thermal conductance [19]. Uniaxial strain can remarkably decrease the thermal conductance of GNRs. In the case of zigzag GNRs, 15% uniaxial strain can decrease the thermal conductance to one fifth of that of an unstrained GNR [68]. Vacancy, defects, and isotope doping have magnificent effects on thermal conductance [58, 69]. Furthermore, it has been recently shown that the thermal conductance of GNRs can be reduced by hydrogen-passivation of the edges [70]. In this chapter, therefore, we aim to investigate the thermal and thermoelectric properties of various graphene-based structures. This can help to improve understanding of thermoelectrics in nanostructues and provide some useful guidelines for engineering nanostructures for thermoelectric applications.

3.1 Thermoelectric Properties of AGNRs

Recent studies have investigated the thermoelectric properties of AGNRs in the presence of vacancies and edge defects [58, 71]. The results show that by increasing the number of defects, the figure of merit decreases. The enhanced phonon scattering on the boundaries of nanostructures is the primary motivation of using nanostructures for thermoelectrics. In this section, we explore the role of geometrical parameters and temperature on the ballistic and diffusive thermoelectric properties.

3.1.1 Ballistic Thermoelectric Properties of AGNRs

GNRs are tailored from the 2D graphene sheet with finite width W. N-AGNR denotes a GNR with armchair edges, the unit cell of which contains N atoms of each sublattice (A and B), as shown in Fig. 3.1. The band-gap (E_g) of AGNRs is inversely proportional to the ribbon's width. AGNRs are classified according to their indices into three categories, $N = 3m - 1$, $N = 3m$, and $N = 3m + 1$, where m in an integer. The lowest band-gap belongs to the category $N = 3m - 1$, whereas the category $N = 3m + 1$ has the highest band-gap. As the band-gap plays an important role in thermoelectrics, only the category $N = 3m + 1$ is considered. However, similar results are expected for the other categories too.

In this section, ballistic thermoelectric properties of AGNRs with different widths at various temperatures are investigated. In the ballistic regime, the transport properties are independent of channel length L. The features of band structures play an important role in the performance of AGNR-based devices. The channel length, therefore, is chosen to be the length of a unit cell ($3a_{cc}$), whereas the ribbon's width varies between $W = 1$ nm and 6 nm and the temperature between $T = 50$ K and 750 K.
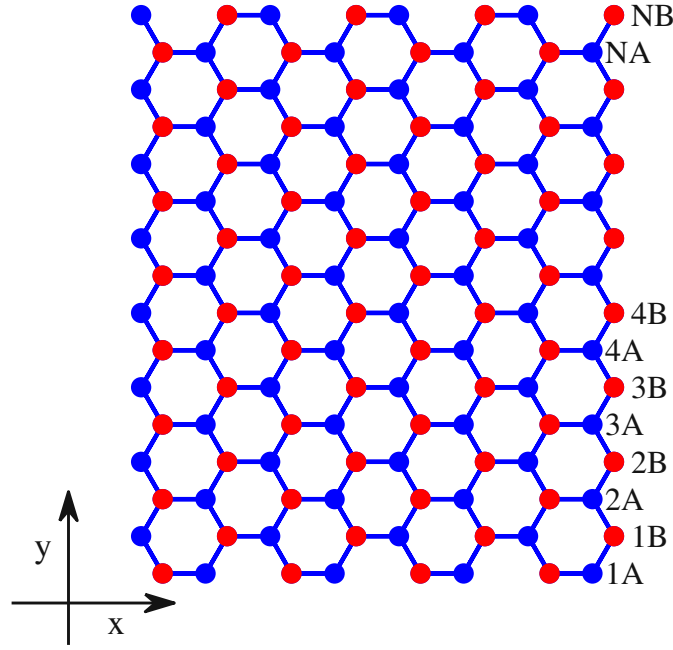
Figure 3.1: The geometrical structure of an N-AGNR. The unit cell contains N carbon atoms of sublattices A and B.

3.1.1.1 Electronic Properties

The ballistic transmission function of AGNRs with different widths is shown in Fig. 3.2. As expected, the energy-gap between conduction and valence band decreases with increasing the ribbon's width. Here, we also denote the energy difference between the second and the first conduction subband by ΔE. This parameter indicates the possibility of a contribution of the second subband to the electronic transport. E_g and ΔE decrease by increasing the ribbons' width. On the other hand, the derivative of the Fermi function, known as the thermal broadening function, has a width of a few $k_B T$ around E_F. Therefore, the width of the thermal broadening function increases with the temperature and, at high temperature, one can expect the second subband also contribute to the electronic conductance of a wide AGNRs.

The electrical conductance (Eq. 2.29), the Seebeck coefficient (Eq. 2.37), the thermo-electric power factor $(S^2 G)$, and the electrical contribution to the thermal conductance (Eq. 2.36) of a 25-AGNR as a function of Fermi energy are shown in Fig. 3.3a-d, respectively. Three different temperatures $T = 150$ K, 300 K, and 500 K are considered. Here, $E_c = E_g/2$ refers to the energy corresponding to the band-edge of the first conduction subband. In contrast to the Seebeck coefficient, the electrical conductance decreases by increasing $E_c - E_F$, so that the power factor has a maximum near the conduction band-edge. The maximum value of the power factor increases with temper-
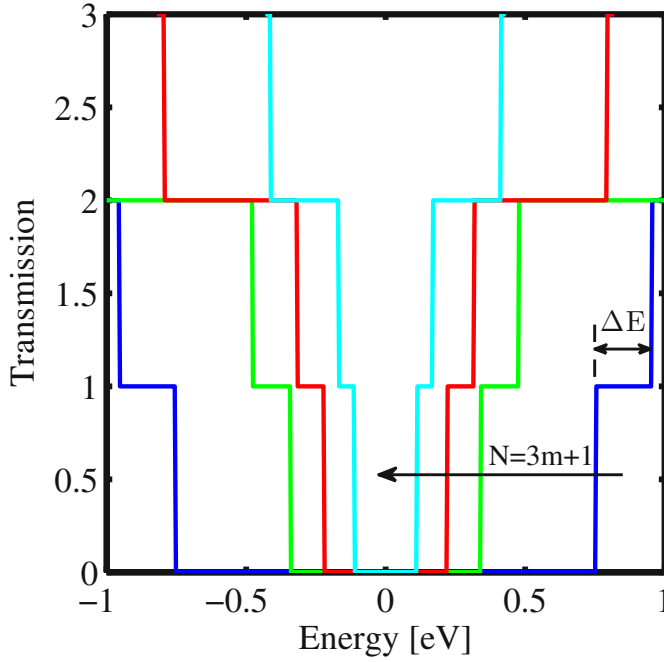
Figure 3.2: The ballistic electronic transmission function as a function of energy with the ribbon's width as a parameter. m varies between 2, 5, 8, and 16 which are corresponding to the ribbon's width of 1, 2, 3, and 6 nm, respectively. ΔE is the energy difference between first and second conduction band edges.

ature due to the contribution of the second conduction subband. Different parameters, corresponding to the Fermi energy at which the power factor is maximum, are shown in Fig. 3.3e-f. By increasing the ribbon's width and so decreasing ΔE, the second conduction band-edge gets closer to the first conduction band-edge E_c. As a result, the overall tranmission function increases near the appropriate Fermi energy, and so the conductance increases with the ribbon's width. This increase is significant at high temperature. On the other hand, the band-gap and so the Seebeck coefficient decrease by increasing W. It is due to the fact that in a low band-gap material, the current of holes and electrons cancel each other out. Overall, the power factor slightly increases by the ribbon's width and temperature. In addition, the electrical contribution to the thermal conductance increases with the ribbon's width and temperature, as well. However, as shown below, it can be neglected in comparison with the lattice thermal conductance.

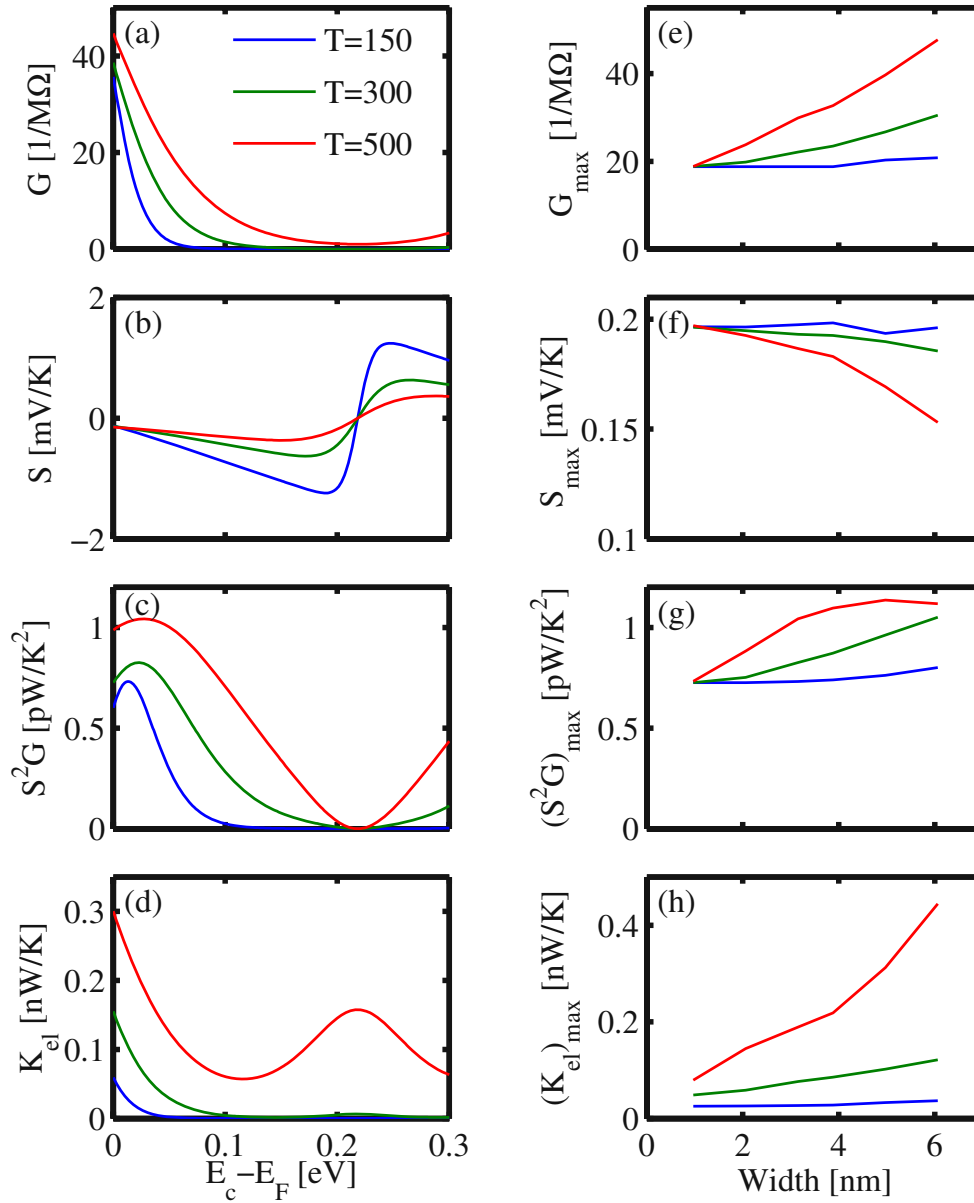
Figure 3.3: (a)-(d) show the ballistic electrical transport parameters of a 25-AGNR as a function of $E_c - E_F$. E_c is the band edge of the first conduction subband. Three different temperatures 150, 300, and 500 K are considered. (e)-(f) show the transport parameters at the Fermi energy at which the thermoelectric power factor has a maximum (see Fig. 3.3-c).

3.1.1.2 Phononic Properties

The ballistic transmission function of phonons, which is the number of phononic modes at some energy $\hbar\omega$ (Eq. 2.42), is shown in Fig. 3.4. As expected, the transmission func-
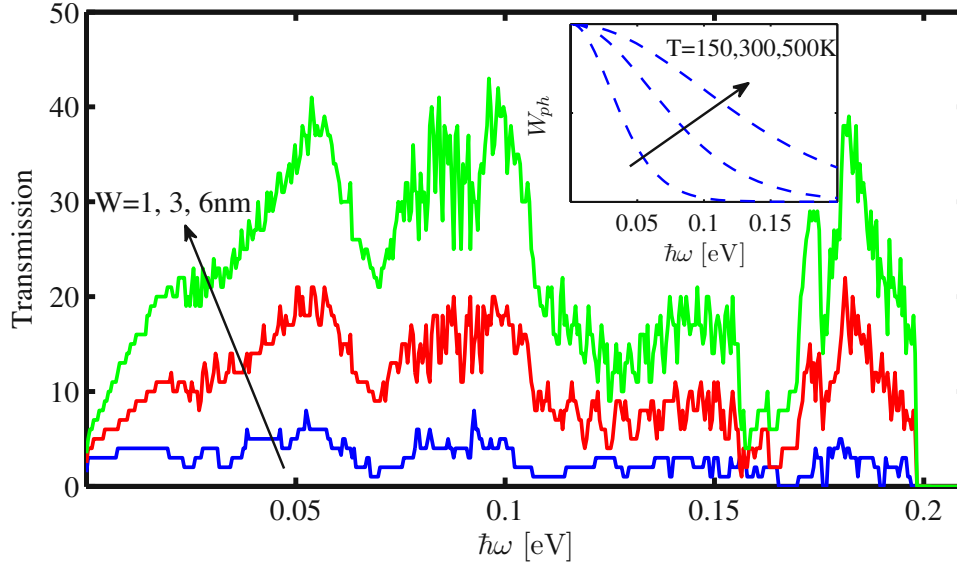
Figure 3.4: Ballistic transmission function of phonons in AGNRs of widths 1, 3, and 6 nm corresponding to $N = 7, 25$, and 49. The inset shows the phononic window function at $T = 150, 300$, and 500 K.

tion increases with the ribbon's width. In addition, the phononic window function is shown in the inset of Fig. 3.4 at various temperatures. This function, which qualifies the contribution of different phonon frequencies in the thermal conductance, increases with temperature. Therefore, at higher temperatures high energy phonons will contribute to the thermal transport as well.

Figure 3.5-a and -b show the ballistic thermal conductance of AGNRs as a function of temperature and the ribbon's width, respectively. By increasing the temperature and thus the width of the phononic window function, the thermal conductance increases. However, as the energy spectrum of AGNRs is limited to 0.2 eV (Fig. 3.4), the thermal conductance saturates at very high temperatures ($T > \sim 800$K). As shown in Fig. 3.5-b, the thermal conductance increases linearly with the ribbon's width. In fact, the ballistic thermal conductance divided by the width is constant. This is due to the fact that by increasing the width and thus the number of carbon atoms in the unit cell, the number of modes increases almost linearly in the whole energy spectrum, and, therefore, the ballistic transmission function is directly proportional to the width.

3.1.1.3 Thermoelectric Figure of Merit

After calculating the ballistic electrical and thermal parameters, one can evaluate the thermoelectric figure of merit using the Eq. 2.1. The ZT values are shown in Fig. 3.6 for the ribbon's widths between 1nm and 6 nm and temperature up to 750 K. By
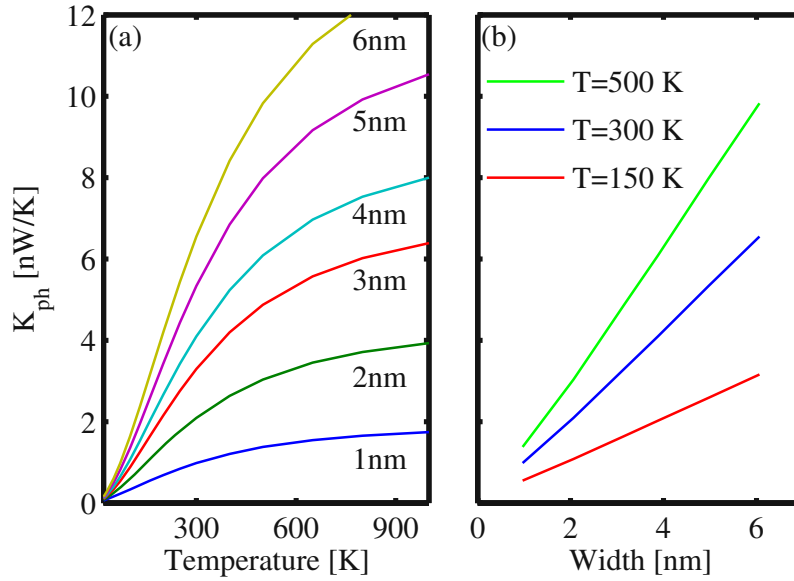
Figure 3.5: Ballistic lattice thermal conductance of AGNRs as a function of (a) temperature and (b) width.

increasing the ribbon's width, ZT decreases drastically. It is due to the fact that the lattice thermal conductance strongly increases with W, whereas the power factor slightly increases. On the other hand, for a given ribbon's width, ZT peaks both at very low and very high temperatures. At high temperature, the contribution of the second conduction subband results in a high power factor. On the other hand, the lattice thermal conductance strongly decreases with temperature, whereas the power factor can be kept by adjusting the Fermi energy. As a result, a high value of ZT can be obtained at very low temperature as well, although the ZT value is smaller than 0.3 for various ribbons and temperatures.

3.1.2 The Role of Line-Edge-Roughness

As shown in Sec. 3.1.1, the high lattice thermal conductance of AGNRs causes a small ballistic ZT value. In fact, A high thermal conductivity in the range of $\sim$ $2000-5300$ W/mK has been reported for wide suspended single-layer graphene [28,72], which is only weakly affected by the boundary and substrate scatterings. On the other hand, in narrow AGNRs, line-edge-roughness (LER) is the dominant scattering source for both electron and phonon transport [70,73–75]. Therefore, in this section, we examine how LER scattering in very narrow AGNRs can affect the thermal and thermoelectric properties.

Very recently, the effect of rough boundaries has been studied in defective AGNRs [70,
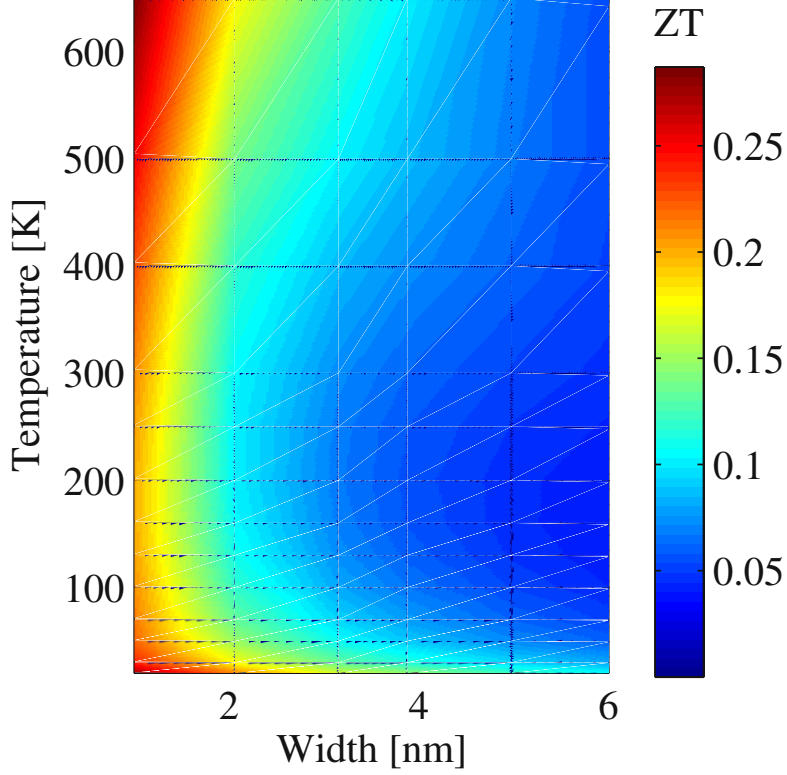
Figure 3.6: Ballistic thermoelectric figure of merit as a function of ribbon's width and temperature.

76–80]. Those previous works have used a simple model for line-edge-roughness which neglect the correlation of the roughness. However, due to the wave nature of phonos, the correlation length of roughness plays an important role as well. To model LER-limited thermal conductivity, an exponential autocorrelation function is employed [81]:

$$R(x) = \Delta W^2 \exp\left(-\frac{|x|}{\Delta L}\right) \tag{3.1}$$

the Fourier transform of which is the power spectrum of the roughness. In Eq. 3.1, ΔW is the root mean square of the roughness amplitude and ΔL is the roughness correlation length. The LER in the real space is achieved by adding a random phase to the power spectrum followed by an inverse Fourier transform [74,81]. Many samples with the same roughness parameters are generated and their thermal properties are evaluated by taking an ensemble average.

To investigate the effect of LER on the thermal conductivity and the MFP of phonons, we performed simulations on a statistical sample of 16-AGNR with roughness parameters of $\Delta W = 0.3$ Å and $\Delta L = 2$ nm. The main results are, however, almost independent of the actual value of the roughness parameters. The statistical average

40
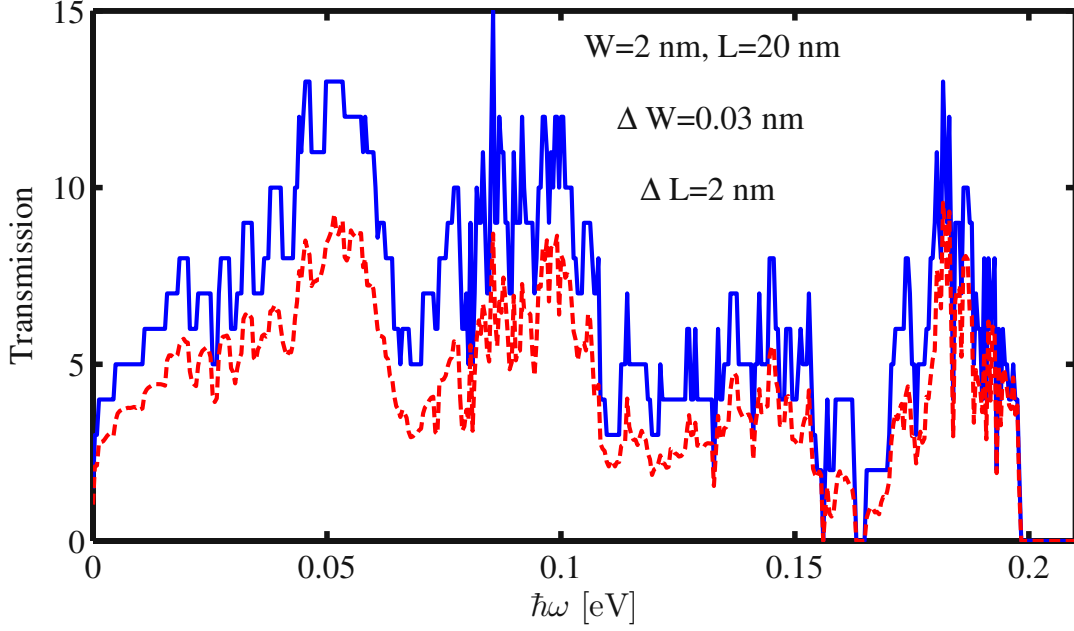
Figure 3.7: The transmission function of phonons for a 16-AGNR: Ballistic result (solid); in the presence of LER with $\Delta W = 0.3$ Å and $\Delta L = 2$ nm for channel length of 20 nm (dashed).

of the transmission function is shown in Fig. 3.7 for a channel length of 20 nm. For reference, the ballistic transmission of a 16-AGNR is also shown with solid line.

Figure 3.7 compares the phonon transmission functions of a 16-AGNR assuming perfect edges and rough edges with roughness parameters of $\Delta W = 0.3$ Å and $\Delta L = 2$nm. By introducing LER, the tranmission decreases from the ballistic value almost over entire energy range. To quantify the dependence of the transmission function on the channel length, the phonon MFP is defined as [32, 57]:

$$\overline{T}_{ph}(\hbar\omega) = \frac{N_{ph}(\hbar\omega)}{1 + L/\lambda_{ph}(\hbar\omega)} \tag{3.2}$$

where $N_{ph}(\hbar\omega)$ is the ballistic transmission function and $\lambda_{ph}(\hbar\omega)$ is the phonon MFP at energy $\hbar\omega$.

Figure. 3.8 shows the phonon MFP of a 16-AGNR as a function of phonon frequency, which is around 50 nm. However, to study the dependence of the thermal conductance on the channel length one can define an effective MFP $\overline{\lambda}_{ph}$ as [19]:

$$K_l = K_{l,B} \frac{\overline{\lambda}_{ph}}{L + \overline{\lambda}_{ph}} \tag{3.3}$$

41
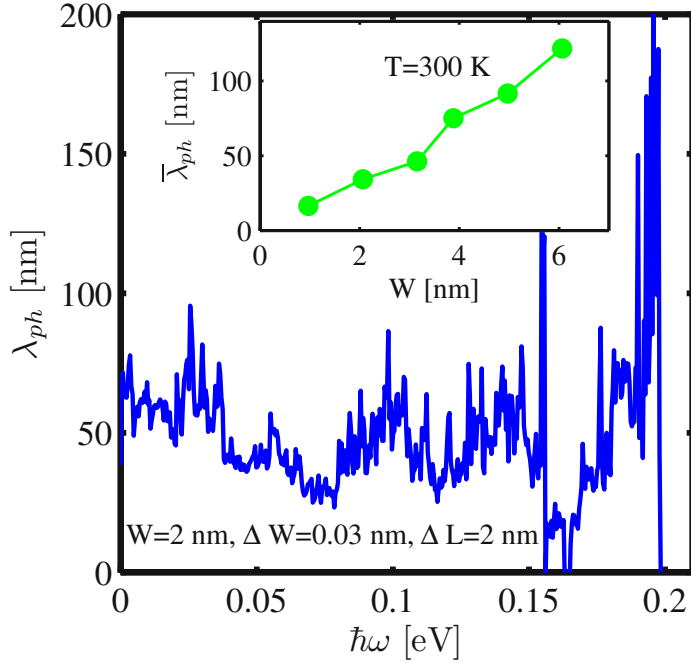
Figure 3.8: The effective mean-free-path of phonons in a 16-AGNR as a function of phonon energy. The inset shows the effective mean-free-path as a function of ribbon's width at room temperature.

which covers the contribution of phonons of different frequencies. Here, the ballistic thermal conductance of AGNRs with perfect edges is denoted by $K_{l,B}$. In the inset of Fig. 3.8 the effective room temperature MFP is shown for ribbon's of different width. The symbols in Fig. 3.8 are ensemble average values. As a rough estimate, the standard deviations of various quantities calculated in this section are about 10% of the corresponding average value for short and narrow channels, whereas they decrease to ∼ 5% of the average values for long and wide channels. By increasing the ribbon's width from 1 nm to 6 nm the effective MFP increases linearly from about 20 nm to 120 nm. The phonon MFP of GNRs with smooth edges was reported to be ∼ 775 nm [82]. Therefore, it seems that LER degrades the high thermal conductivity of AGNRs and can help one achieves higher values of ZT.

To examine the effect of LER on the electronic structure, the electronic transmission of a 16-AGNR with the channel length of 5 nm is shown in Fig. 3.9, with and without the LER. LER degrades the transport of electrons at different energies. However, the reduction is lower at energies near the sub-band edges, where the density of states and thus the scattering rate is higher. Therefore, the presence of LER degrades the sharp features of electronic transmission function and the thermoelectric power factor [83]. The corresponding MFP is shown in Fig. 3.10. The MFP is very small near the band edges due to the high density of states and thus high scattering rate. This indicates
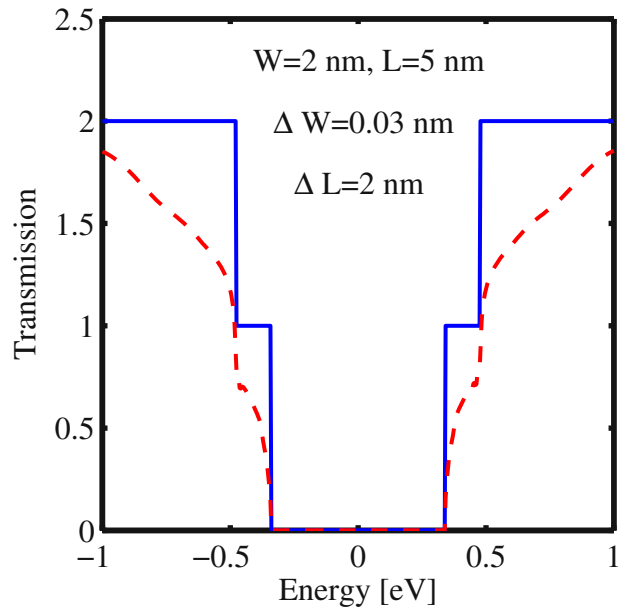
Figure 3.9: The electron transmission of 16-AGNR in the presence of line-edge-roughness is compared with the ballistic one. The channel length is 5 nm.
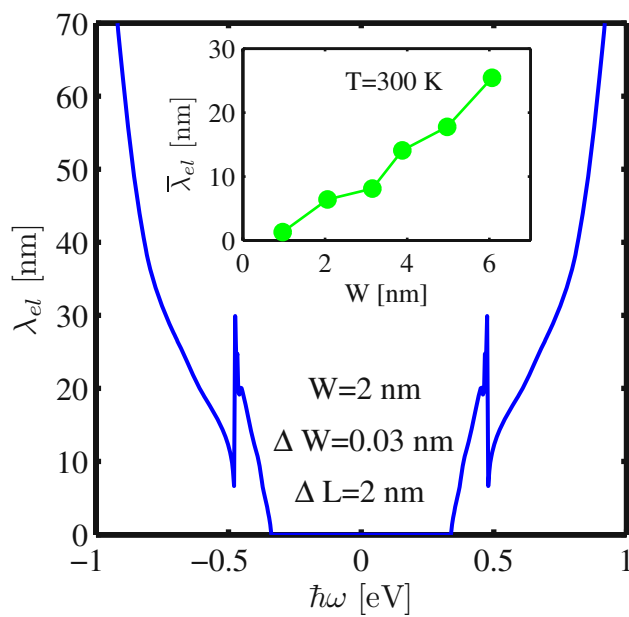
Figure 3.10: The electron mean-free-path is shown as a function of electron energy. Inset: The effective mean-free-path linearly increases with ribbon's width.
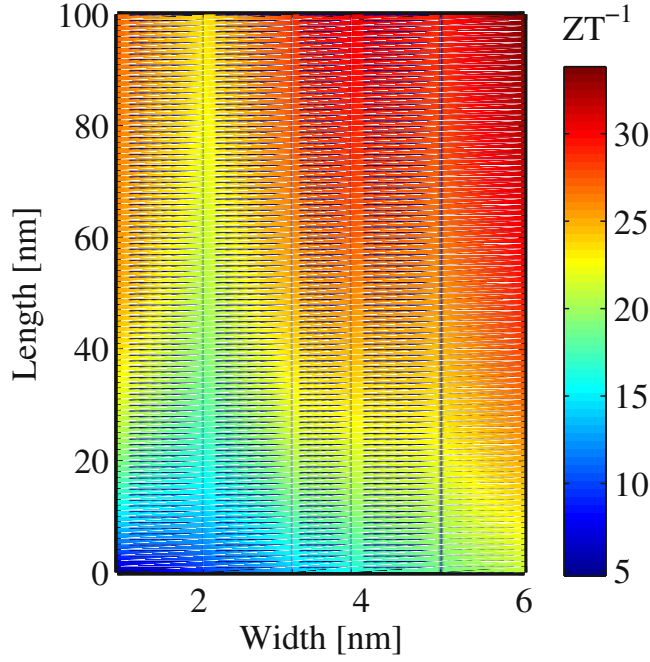
Figure 3.11: The thermoelectric figure of merit as a function of channel length and width in the presence of line-edge-roughness.

that the diffusive transmission function is very negligible near the first conduction subband (Fermi energy), which can drastically degrade the transport parameters. The effective MFP is also shown in the inset of Fig. 3.10. It increases almost nearly with the ribbon's width. However it is smaller than 30 nm even for 6 nm AGNR. The small electron MFP can be described by considering the sensitivity of the band-gap to the ribbons width. The band-gap is not only inversely dependent on the ribbon's width, it is strongly dependent to the index of the ribbon either. Therefore, the presence of LER is not a small perturbation for the electron transport. In fact, the electron transmission will be in the localization regime and one should even define the localization length instead of mean-free-path for long channel [74]. As the ratio $\overline{\lambda}_{el}/\overline{\lambda}_{ph}$ is considerably smaller than one, we conclude that the presence of boundary scattering is not appropriate for the thermoelectric performance of AGNR-based devices, in contrast to what has been observed in silicon nanowires [20].

Finally, the inverse of ZT at room temperature as a function of ribbon's width and channel length is shown in Fig. 3.11. For very short channels, in which the transport is almost ballistic, the value of ZT is ~ 0.2 for narrow ribbons and it decreases by increasing the width, as described in Sec. 3.1.1. However, the value of ZT decreases by increasing the channel length, as the electron tranmission decreases faster than the phonon transmission function. For the channel length of about 100 nm, ZT is less than 0.05, and even smaller values are expected for longer ribbons.

44

In this section, the ballistic and diffusive thermoelectric properties of narrow AGNRs are comprehensively studied. The results indicate that the contribution of the second conduction subband increases the power factor. The second conduction is closer to the first one in wider ribbons. However, the small band-gap of wide AGNRs degrades the Seebeck coefficient. Designing an AGNR with large band-gap and closer conduction subbands is the way that could significantly improve the thermoelectric power factor. On the other hand, the high thermal conductance degrades the thermoelectric performance of AGNRs. Using line-edge-roughness for decreasing the thermal conductance degrades the thermoelectric properties, as it is more severe in the case of electron transport. Engineering AGNR-based materials in which the transport of phonons is more sensitive to the boundary scatting than that of electrons can help to improve or at leat retain the ZT values in long ribbons. It might be accessible in some structures, in which the band-gap is not strongly related to the width. In the next couple of sections, these ideas are used in order to achieve high performance graphene-based thermoelectric devices.

3.2 Thermoelectrics of Graphene Antidot Lattices

In this section, we discuss the ballistic thermoelectric properties of a new graphene-based structure, called graphene antidot lattice (GALs) [65]. Although the scattering of electrical and thermal carriers plays an important role in the thermoelectric properties of materials, the ballistic results give us an insight into how these new materials can be used in the future thermoelectric applications. The results show that by introducing antidots in the graphene sheet (Fig. 3.12) the thermal conductance of GALs decreases and the respective ZT values increase.

3.2.1 Geometrical Structure

The electrical and optical properties of GALs have been theoretically studied in Refs. [26,64,84]. The results indicate that by introducing regular antidots in a graphene sheet, it is possible to achieve a direct band gap semiconductor from a semi-metallic pristine graphene sheet. Bai and co-workers reported the first field-effect-transistor based on GALs [65]. To investigate the effect of the dot geometry on the thermoelectric properties of GALs, the unit cell of a GAL is described by two parameters L_S and N, where L_S is the side length of the hexagon in terms of the graphene lattice constant ($a = 2.46 \mathring{A}$) and N is the number of carbon atoms removed from the pristine supercell. In Fig. 3.12 Circ, Rect, Hex, IsoTri, and RightTri represent a circular, rectangular, hexagonal, iso-triangular, and right-triangular antidot in the hexagonal unit cell, respectively. Fig. 3.12-b shows a circular antidot which is formed by removing 108 carbon atoms from a cell with $L_S = 10$. It is therefore represented by Circ(10, 108). The number of edge carbon atoms in a unit cell of different GALs is also given in
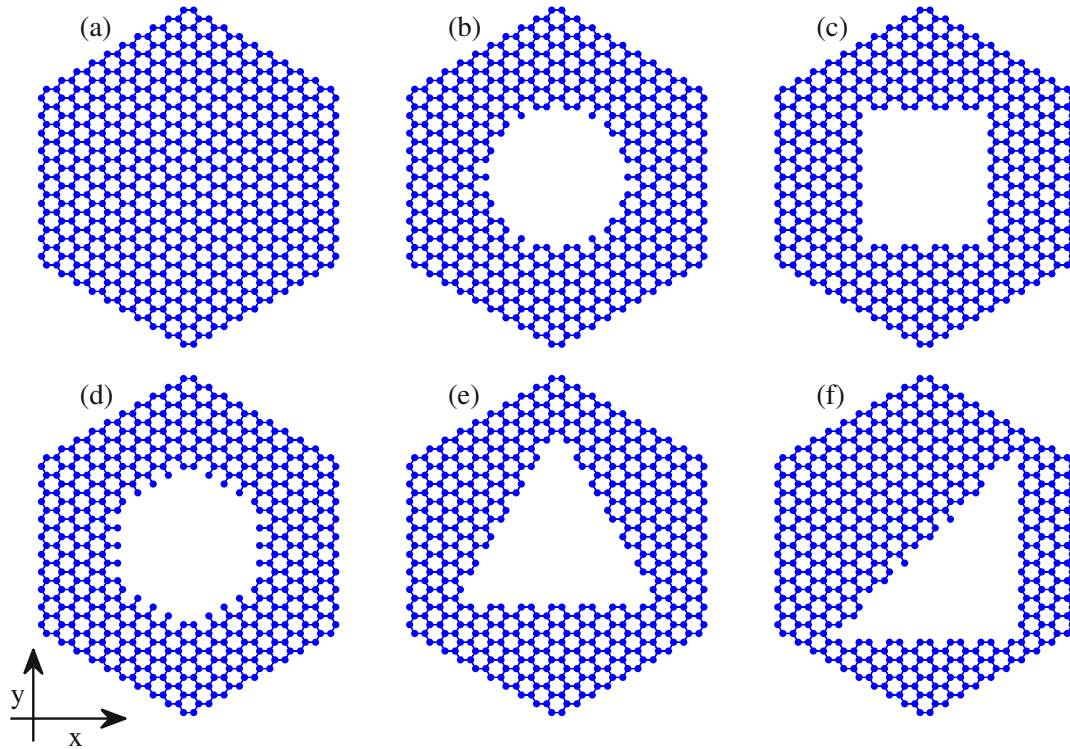
Figure 3.12: Geometrical structures of different GALs. (a)-(f) indicate pristine graphene, $\text{Circ}(10, 108)$, $\text{Rect}(10, 120)$, $\text{Hex}(10, 120)$, $\text{IsoTri}(10, 126)$, and $\text{RightTri}(10, 126)$, respectively. Transport is assumed to be in the direction of the x-axis.

Table 3.1: The number of edge carbon atoms in a unit cell of different GALs.

Structure	Number of boundary atoms
$\text{Circ}(10, 108)$	30
$\text{Rect}(10, 120)$	32
$\text{Hex}(10, 120)$	30
$\text{IsoTri}(10, 126)$	36
$\text{RightTri}(10, 126)$	38

Table 3.1. As shown below, the number of carbon atoms at the boundary plays an important role on the thermal properties of the structure.
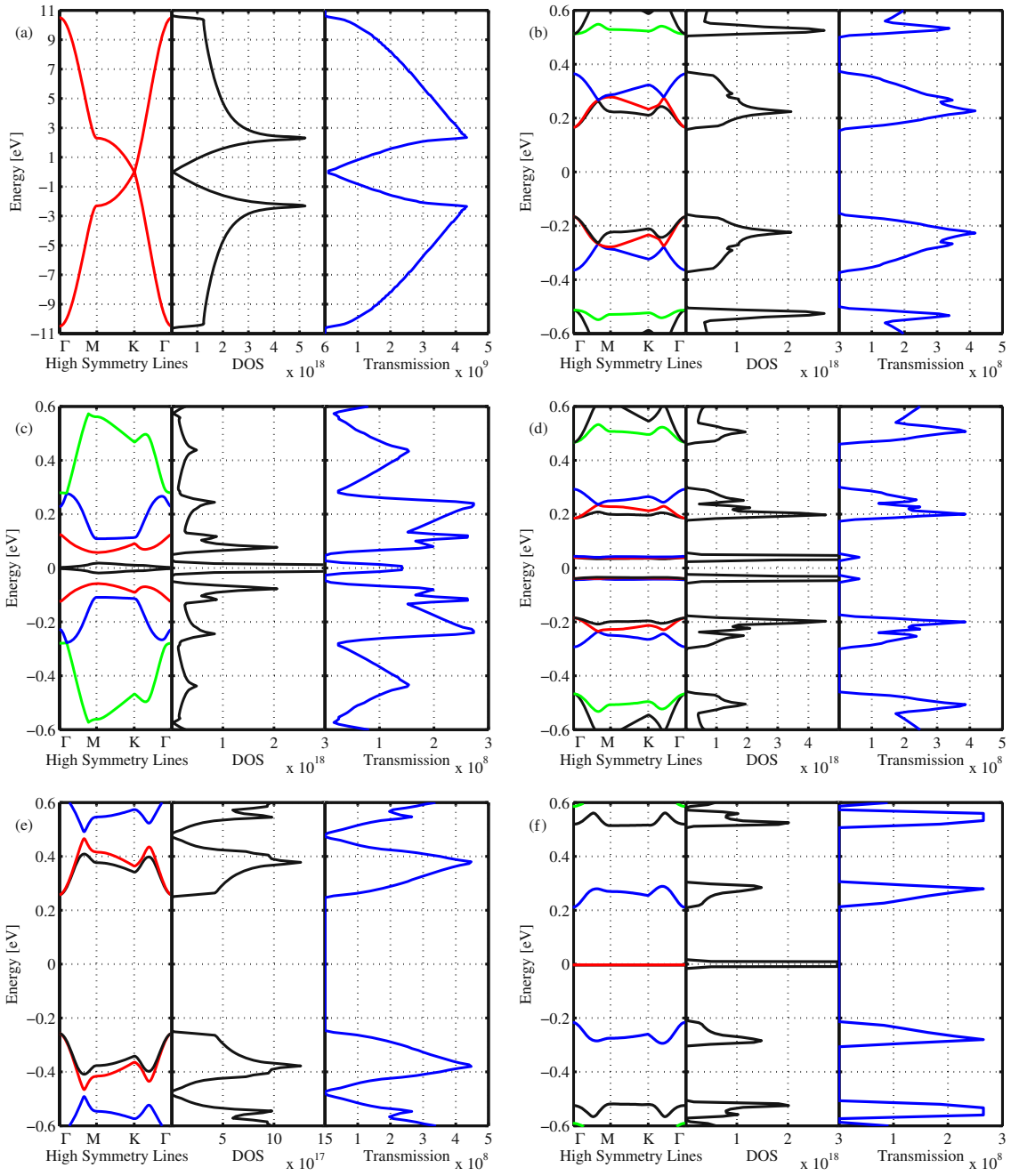
Figure 3.13: The electronic band structure along high symmetry lines. The density of states and transmission of (a) pristine graphene, (b) Circ(10,108), (c) Rect(10,120), (d) Hex(10,120), (e) IsoTri(10,126) and (f) RightTri. The units of the DOS and transmission are $[eV^{-1}m^{-2}]$ and $[m^{-1}]$, respectively.

3.2.2 Electronic Structure

The Seebeck coefficient and power factor are sensitive to the details of the density of states and the asymmetry between electrons and holes [85, 86]. The electronic band structures of GALs are calculated using a third nearest-neighbor tight-binding method (Sec 2.1.1). By introducing the antidots in the graphene sheet, the zero band-gap graphene can be converted into a narrow band-gap semiconductor [26, 27] (see Fig. 3.13). This issue plays an important role in thermoelectric applications. In contrast to pristine graphene, GALs have a beneficial band-gap, so that one can suppress either the electron or the hole current to obtain unipolar conduction. For example, by adjusting the Fermi level near the conduction band the hole current will be negligible. The electron-hole asymmetry with respect to the Fermi level depends on the band-gap, on the sharp features of transmission, on the width of the first conduction subband, and on the value of the transmission. At room temperature, the width of the thermal broadening function is about 0.2eV. Therefore, a band-gap around 0.2eV and a first conduction subband width larger than 0.2eV will be ideal for thermoelectric applications.

In RightTri(10,126), there are some localized midgap states, see Fig. 3.13-f, as a result of sublattice-symmetry breaking [84, 87]. They have a zero group velocity and can not contribute to the carrier transport. Although RightTri(10,126) has the sharpest features in the transmission and its transport band-gap is about 0.4eV, the width of the first conduction subband of RightTri(10,126) is only 0.12eV. As a result, it has a high Seebeck coefficient and a low electrical conductance, see Fig. 3.14. The first conduction subband of a Rect(10,120) has a non-zero group velocity. Therefore, the rectangular GAL is considered as a zero band-gap material and as a result, the Seebeck coefficient will be small which is detrimental to thermoelectric applications. In a Hex(10,120), the first conduction and valence subbands are quasi-flat bands due to existence of some edge carbon atoms which have only one nearest neighbor [87]. As shown in Fig. 3.13-d, these bands have a small group velocity and have a small contribution to electron transport. As a result, the maximum value of the Seebeck coefficient of Hex(10,120) is not very large and is located close to the band-edge of the second conduction subband. On the other hand, the electrical conductance peaks close to the second subband-edge. Therefore, Hex(10,120) has the third highest power factor among the GALs with different antidot shapes.

On the other hand, the band-gap and the first conduction subband width of Circ(10,108) and IsoTri(10,126) are nearly 0.4eV and 0.2eV, respectively. They also have the highest transmissions. Therefore, as shown in Fig. 3.14, they are the best thermoelectric GALs in terms of the power factor. Because of a sharp feature in the transmission, Circ(10,108) has the highest power factor of the GALs considered. In addition, as shown in Fig. 3.14-d the electron contribution to the thermal conductance can be neglected in comparison with the lattice thermal conductance (see Table 3.2).
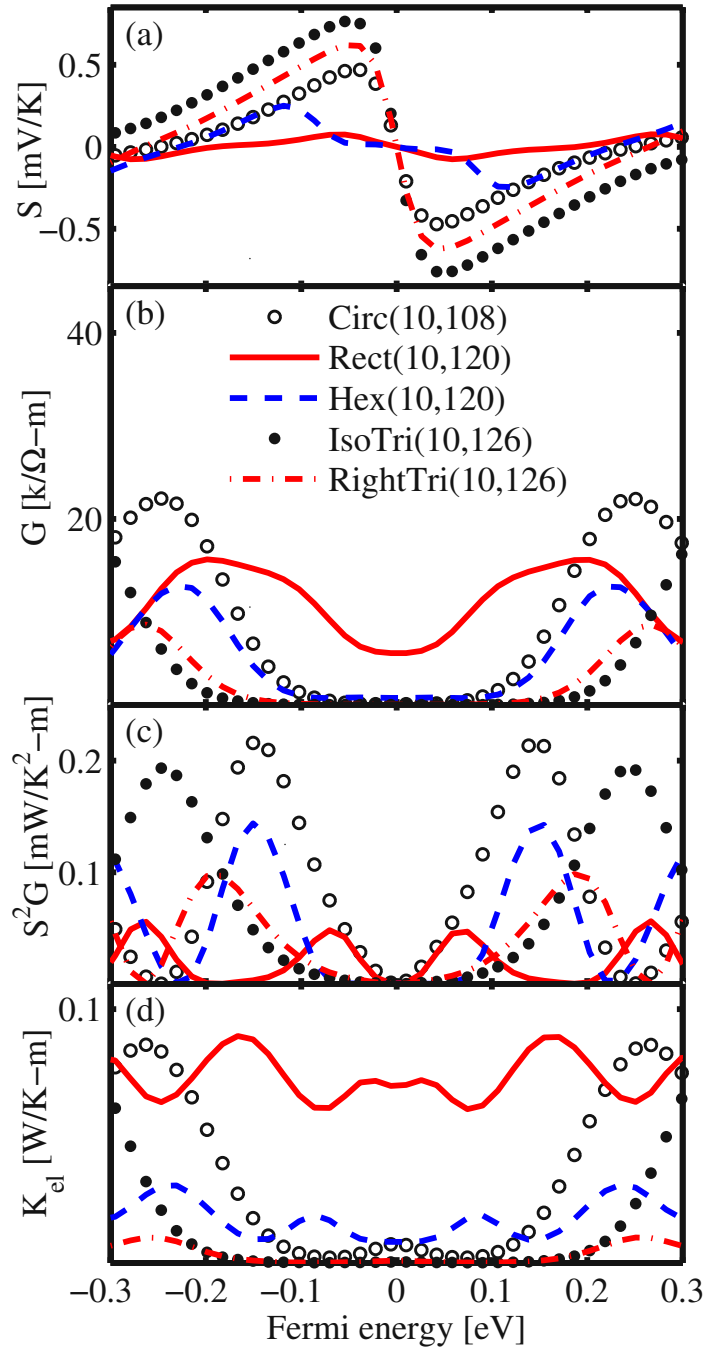
Figure 3.14: (a) Seebeck coefficient, (b) electrical conductance, (c) power factor, and (d) electrical thermal conductance as a function of the Fermi level.

3.2.3 Phononic Structure

We compare the thermal conductance of circular GALs with $L_S = 10$ and different radii, including Circ(10,24), Circ(10,108) and Circ(10,258). The phonon density of states (DOS) and phonon transmission of these GALs are shown in Fig. 3.15. As indicated in Table 3.2, by increasing the size of the antidot, the phonon DOS, the phonon transmission, and the thermal conductance are significantly reduced. In Fig. 3.16 two phonon modes of Circ(10,108) at the Γ point are shown. Fig. 3.16-a presents a localized phonon mode as a result of introducing antidots, whereas, Fig. 3.16-b shows a propagative mode. By introducing antidots into the graphene sheet, some phonon modes become localized, similar to electrons, and they can not contribute to the thermal conductance.
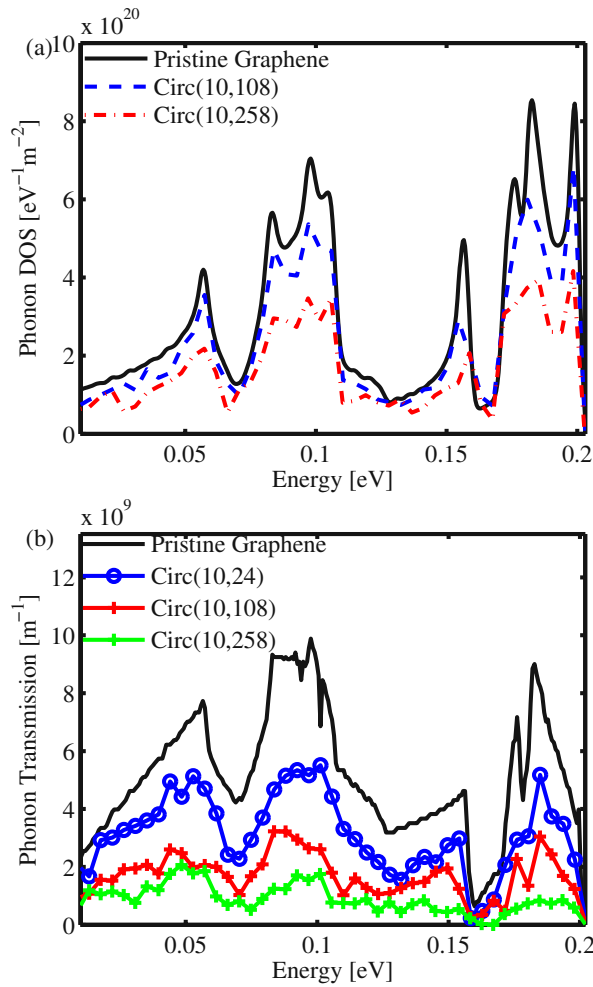
Figure 3.15: Comparison between (a) phonon density of states and (b) transmission of pristine graphene and circular GALs with different antidot areas.

50

Table 3.2: The comparison of the thermal conductance of pristine graphene and different GALs.

Structure	Thermal conductance [W/K-m]
Pristine Graphene	1.3813
Circ$(10, 24)$	0.6948
Circ$(10, 108)$	0.3764
Circ$(10, 258)$	0.2220
Rect$(10, 120)$	0.3378
Hex$(10, 120)$	0.3764
IsoTri$(10, 126)$	0.2606
RightTri$(10, 126)$	0.2509

To investigate the effect of the antidot circumference, we compare GALs with nearly the same area and different shapes, including Circ(10,108), Rect(10,120), Hex(10,120), IsoTri(10,126), and RightTri(10,126). Although the DOS of these GALs have the same order as that of a pristine graphene sheet, the transmissions can be very different. Fig. 3.17-a shows that the phonon transmissions of Circ$(10, 108)$ and Rect$(10, 120)$ are quite different from that of pristine graphene. However, Circ$(10, 108)$, Rect$(10, 120)$, and Hex$(10, 120)$ have nearly the same transmissions, whereas IsoTri$(10, 126)$ and Right$(10, 126)$ have similar transmissions which are different from the first group, see Fig. 3.17-b.

The transmissions of Circ$(10, 108)$, Rect$(10, 120)$, and Hex$(10, 120)$ are similar because they have similar circumference and thus the same number of boundary carbon atoms. Furthermore, the nearest-neighbor dots in these GALs have nearly the same distance. On the other hand, IsoTri$(10, 126)$ and RightTri$(10, 126)$ have the same circumference which is different from those of the first group.

The thermal conductances of pristine graphene and different GALs are summarized in Table 3.2. Triangular GALs have the smallest thermal conductance, although they have the minimum area of all antidot shapes. This behavior can be explained by considering the fact that triangular antidots have the highest circumference of all antidots with the same area. This indicates that circumference of the antidot has a stronger effect on the thermal conductance rather than its area.
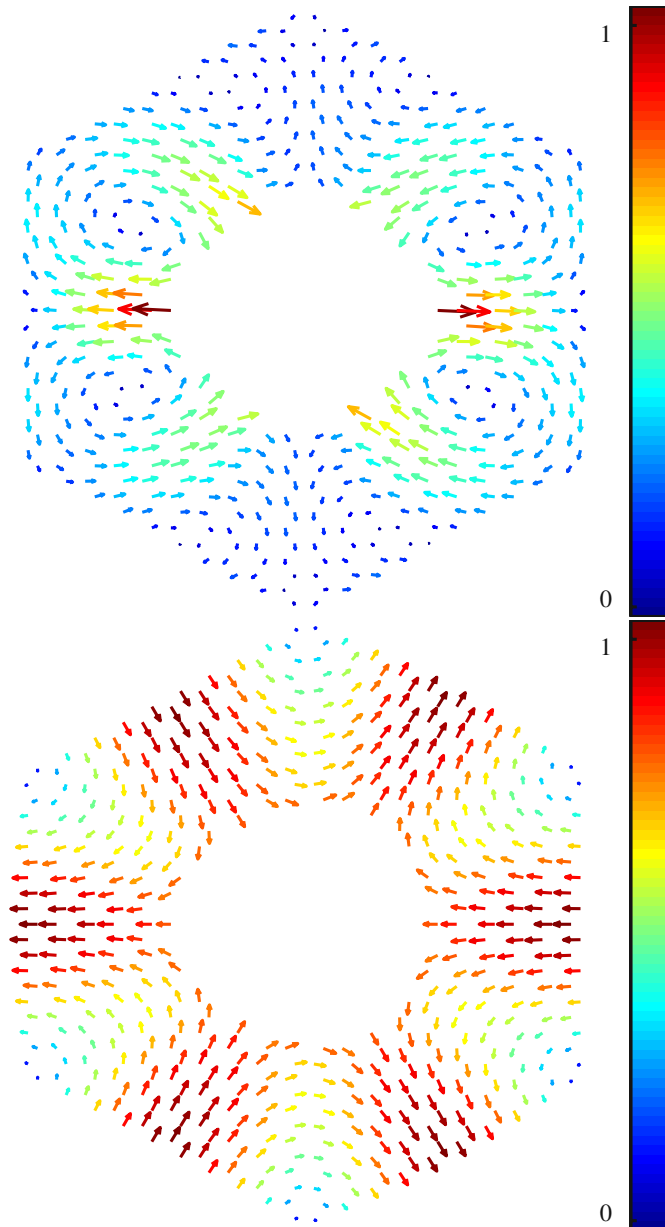
Figure 3.16: Phonon modes at Γ point: (a) represents a localized mode at $E = 30\text{meV}$ and (b) represents a propagating mode at $E = 16\text{meV}$. The amplitude of the vibrations has been normalized.

3.2.4 Thermoelectric Figure of Merit

The figures of merit of different GALs as a function of the Fermi energy are compared in Fig. 3.18. IsoTri has the highest ZT, because it has the lowest lattice thermal conductance and one of the largest Seebeck coefficients. At room temperature, the factor $\partial f / \partial E$ has significant values only in the range of 0.2eV around the Fermi level.
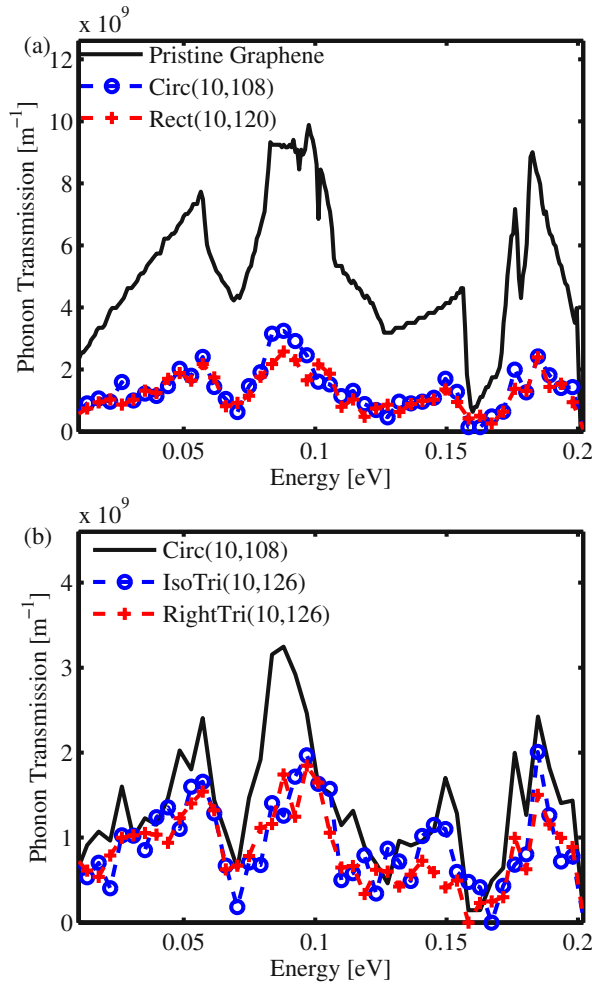
Figure 3.17: (a) The comparison between the phonon transmission of a pristine graphene, Circ(10, 108), and Rect(10, 120). (b) The comparison between the phonon transmission of Circ(10, 108), IsoTri(10, 126), and RightTri(10, 126). IsoTri(10, 126) and RightTri(10, 126) have similar transmission, but generally smaller than that of Circ(10, 108). This can be explained by a larger circumference and a lower distance between the nearest-neighbor antidots of these two GALs.

Under the condition $E_G > 0.2\text{eV}$, holes have no contribution to the total electrical current. A large value of the Seebeck coefficient is therefore obtained.

In our work we did not consider the passivation of dangling bonds at the edges. However, it has been shown that hydrogen passivation of dangling bonds results in further reduction of the thermal conductance [70]. Therefore, a higher ZT for GALs can be obtained by edge passivation.
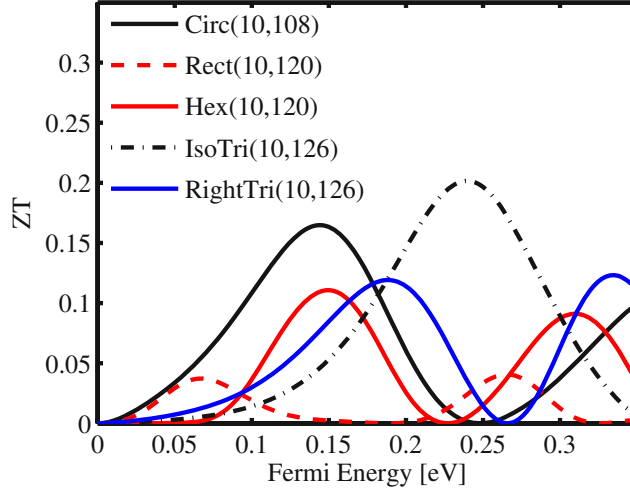
Figure 3.18: The figure of merit ZT of different GALs as a function of the Fermi energy.

3.3 Thermoelectrics Engineering in ZGNRs

Graphene is not a useful thermoelectric material. Although its electrical conductance is as high as that of copper [23], its ability to conduct heat is even higher [82], which increases the denominator of ZT. To make things worse, as a zero bandgap material, pristine graphene has a very small Seebeck coefficient [24], which minimizes the power factor S^2G. In order to improve the Seebeck coefficient graphene needs to acquire a bandgap. This can be achieved by appropriate patterning of the graphene sheet into nanoribbons [25, 27]. Graphene nanoribbons (GNRs) are thin strips of graphene, where the bandgap depends on the chirality of the edges (armchair or zigzag) and the width of the ribbon. Armchair GNRs (AGNRs) can be semiconductors with a bandgap inversely proportional to their width [25]. Although the acquired bandgap can increase the Seebeck coefficient, when attempting to reduce the thermal conductivity by introducing disorder in the nanoribbon, as described in Sec. 3.1, the electrical conductivity is also strongly affected [58, 88], and the thermoelectric performance remains low. Zigzag GNRs (ZGNRs), on the other hand, show metallic behavior with very low Seebeck coefficient, but as described in Ref. [88], the transport in ZGNRs is nearly unaffected in the presence of line edge roughness, at least in the first conduction plateau around their Fermi level.

In this section, by using atomistic electronic and phononic bandstructure calculations, and quantum mechanical transport simulation, it is shown that despite the zero bandgap, the thermoelectric performance of ZGNRs can be largely enhanced. For this a series of design steps are employed: i) Introducing extended line defects (ELDs) as described in Ref. [89] can break the symmetry between electrons and holes by adding

additional electronic bands. This provides a sharp band edge around the Fermi level and offers a band asymmetry which constitutes an "effective bandgap" for thermoelectric purposes. ii) Introducing background impurities enhances the "effective bandgap". iii) Introducing edge roughness reduces the lattice part of the thermal conductivity more effectively than it reduces the electrical conductivity. Using these measures, the figure of merit ZT can be greatly enhanced and high thermoelectric performance could be achieved.

3.3.1 The Role of Extended Line Defects

An efficient thermoelectric material must be able to effectively separate hot from cold carriers. The quantity that determines the ability to filter carriers is the Seebeck coefficient. The Seebeck coefficient depends on the asymmetry of the density of states around the Fermi level. In semiconductors the Seebeck coefficient is large, whereas in a metal the density of states is more uniform in energy and the Seebeck coefficient is small. Metallic ZGNRs also have a small Seebeck coefficient because their transmission is constant around the Fermi level, despite the peak in the DOS at $E = 0$ eV due to the edge states. Recently, however, Bahamon et al. have investigated the electrical properties of ZGNRs that included an ELD (ELD-ZGNRs) along the nanoribbon's length [89]. It was reported that the ELD breaks the electron-hole energy symmetry in nanoribbons, and introduces an additional electron band around the Fermi level. In such a way an asymmetry in the density of states and the transmission function are achieved which improves the Seebeck coefficient. This particular structure has also been experimentally realized recently [90].

For the electronic structure calculations, the Hamiltonian of the GNRs is described in the standard first nearest-neighbor atomistic tight-binding p_z orbital approximation. The hopping parameter is set to -2.7 eV and the on site potential is shifted to zero so that the Fermi level remains at 0 eV. This model has been recently used to describe the electronic transport of ELD-ZGNR with double-vacancies and the results are in good agreement with first-principle calculations and experimental studies [89,90]. To date, only a few first-principle calculations and experimental studies have been conducted for structures that include ELDs [90–92]. The two main features of the electronic structure, the asymmetry between electrons and holes, and the metallic behavior of the ELD in the graphene ribbon have been described in these studies, and are also captured by the tight-binding model, which is used here for ZGNR-based structures.

The changes in the electronic structure of the ZGNRs after the introduction of the ELD are demonstrated in Fig. 3.19. Figure 3.19-a shows the atomistic geometry of the pristine ZGNR of width $W \sim 4$ nm (with 20 zigzag edge lines) and Fig. 3.19-b its electronic structure. The Fermi level is at $E = 0$ eV due to the symmetry of the electron and hole bands. Figure 3.19-c shows the structure of the ELD-ZGNR with the same width. The region where the ELD is introduced is shown in red color. The ELD changes the hexagons of the GNR to pentagons and octagons after a local
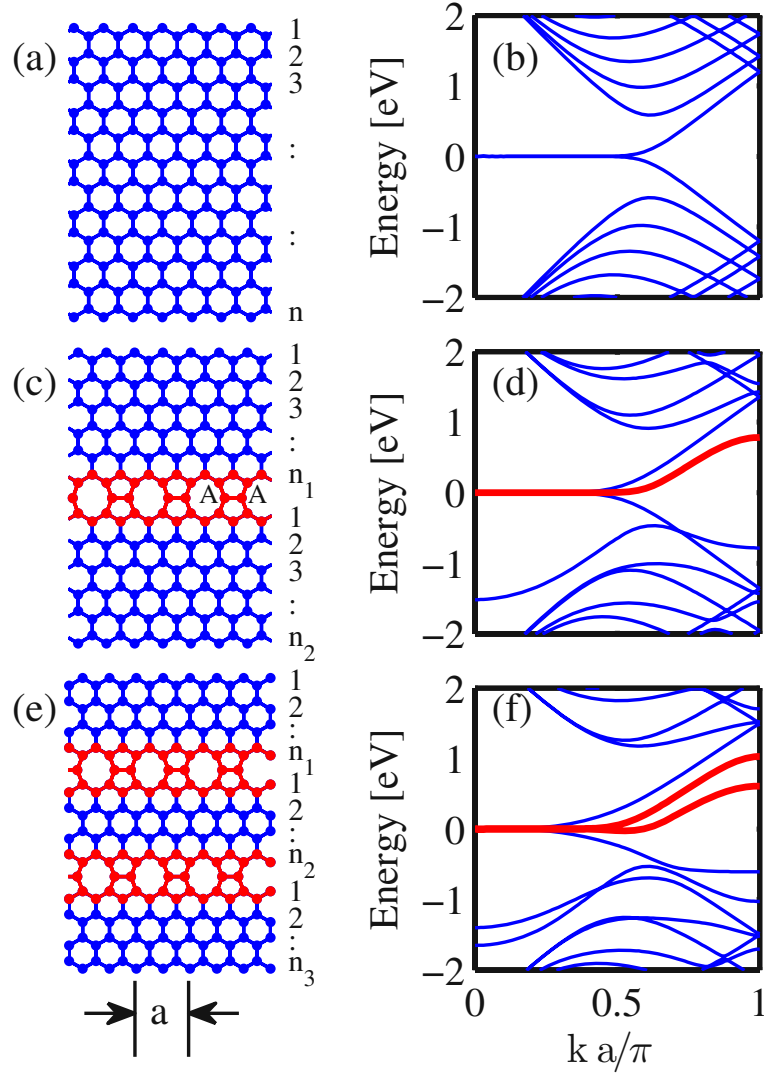
Figure 3.19: The geometrical structure of (a) ZGNR(n), (c) ELD-ZGNR(n_1,n_2), and (e) 2ELD-ZGNR(n_1,n_2,n_3). The bandstructure of (b) ZGNR(20), (d) ELD-ZGNR(10,10), and (f) 2ELD-ZGNR(8,4,8). The bandstructure of ZGNR(20) is folded for a better comparison. The translation vector length is $a = 0.49$ nm. The numbers n, n_1, n_2 and n_3 indicate the number of zigzag edges on the top, bottom, and middle of the ELD regions.

rearrangement of the bonding and the introduction of two additional atoms in the unit cell. To describe the ELD-ZGNR structure a two parameter notation is used as ELD-ZGNR(n_1,n_2), where n_1 and n_2 are the indices of the partial-ZGNRs above and below the line defect, respectively (i.e. the number of zigzag edge lines of atoms). In this work we only consider the cases $n_1 = n_2$.

The bandstructure of the ELD-ZGNR(10,10) is shown in Fig. 3.19-d. The thick-red

line shows a new band that is introduced in the conduction band near the Fermi energy ($E = 0$ eV), which corresponds to the ELD. There are two effects that result in the creation of the extra band. Part of the physics behind this is explained by Pereira et al. in Ref. [93]. The first effect is that a defect in the graphene system will introduce states that reside close to the Fermi level at $E = 0$ eV. This is similar to the edge states of the ribbons that tend to reside near the Fermi level. The second effect again described in Ref. [93], is that an asymmetry in the dispersion between electrons and holes will be created when carbon atoms of the graphene sublattice "A" (or "B") are coupled with atoms from "A" (or "B") again. Usually, the atomic arrangement in graphene can be splitted in sublattices "A" and "B", where atoms from "A" couple to "B" and vise versa. When this happens, the dispersion is symmetric in the first-nearest neighbor tight-binding model. At a defect site such as the ELD, where "A" connects to "A" as seen in Fig. 3.19-c, such asymmetry can be observed. The fact that the overall bandstructure has additional bands compared to the pristine ribbon is also caused by the two extra atoms in the unit cell.

Moving one step further, in Fig. 3.19-e the geometry of a GNR with two ELDs is shown. This structure is denoted as 2ELD-ZGNR(n_1,n_2,n_3), where n_1, n_2, and n_3 denote the the number of zigzag carbon lines above, within, and below the line defects. Figure 3.19-f shows the electronic structure of the 2ELD-ZGNR(8,4,8). In this case two additional bands are introduced near the Fermi level as designated by the thick-red lines. In this structure the asymmetry between electron and hole bands around the Fermi level ($E = 0$ eV) is further enhanced.

Figure 3.20 demonstrates the increase in the asymmetry of the bands around the Fermi level by showing how the transmission changes when one or two ELDs are introduced in the channel. For the pristine ZGNR, the transmission is equal to one, indicating the existence of a single propagating band at energies around the Fermi level (green line). With the introduction of one ELD, the conduction band ($E > 0$ eV) is composed of two subbands, whereas the valence band ($E < 0$ eV) is still composed of one subband. With the introduction of two ELDs, three conduction subbands appear, but still only one valence subband. As it will be shown below, this asymmetry will improve the Seebeck coefficient. This constitutes the first design step in improving the thermoelectric performance of ZGNRs.

There is, however, another point worth mentioning. In Fig. 3.21 the colormaps show the normalized current spectrum at $E = 0.2$ eV in the cross sections of the ELD-ZGNRs described in Fig. 3.20. Figure 3.21-a shows the current spectrum of the ELD-ZGNR(10,10). The current is zero close to the edges of the ribbon and peaks near the center. This is demonstrated more clearly in Fig. 3.21-d, which shows the current along one atomic chain perpendicular to this channel (blue line). The black line of Fig. 3.21-d illustrates the current density on the cross section of the pristine ZGNR channel for reference.

The current spectrum for the 2ELD-ZGNR(8,4,8) is shown in Fig. 3.21-b. The situation is now different since most of the current is confined within the two ELDs.
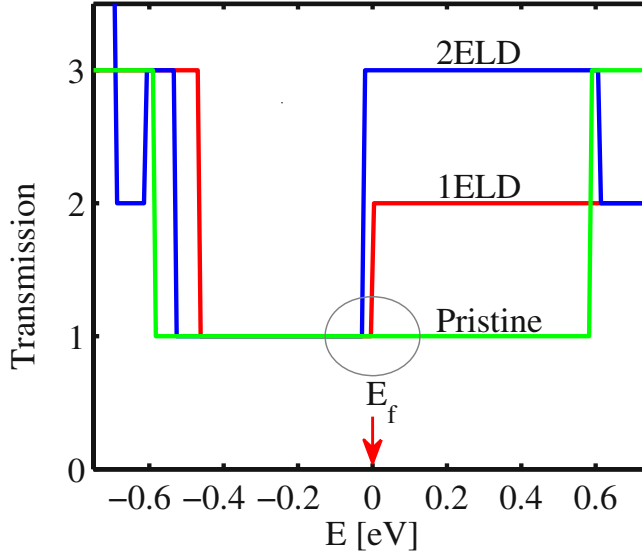
Figure 3.20: The transmission function for three different structures: i) The pristine ZGNR(20), ii) ELD-ZGNR(10,10), and iii) 2ELD-ZGNR(8,4,8).

This, however, is the case only when the distance between the ELDs is smaller than the widths of the upper/lower regions. In the case where the width of the middle region is similar to the widths of the upper/lower regions, the current is spread more uniformly in the channel as shown in Fig. 3.21-c for the 2ELD-ZGNR(7,6,7) channel. Figure 3.21-e shows again the current along one atomic chain in the cross section of these ribbons. The current spectrum is localized in the middle of the channel in the 2ELD-ZGNR(8,4,8) channel (red line) compared to the pristine channel (black line). In a 2ELD-ZGNR(9,2,9) channel with a narrower middle region the current spectrum is localized even closer around the center (blue line). A large portion of the current is in general flowing around the ELD regions. The design capability to localize the current spectrum in the middle of the channel away from the edges will prove advantageous in the presence of edge roughness since the current in this case will be less affected. On the other hand, in the case of the 2ELD-ZGNR(7,6,7) channel the current spectrum tends to concentrate more close to the edges (green line).

3.3.2 The Role of Substrate Impurities

The possibility of further enhancing the asymmetry between electron and hole transport near the Fermi level by the introduction of positively charged substrate background impurities is examined. The effect of background impurities is included in the Hamiltonian in a simplified way as an effective negative long range potential energy on the appropriate on-site Hamiltonian elements as described in Ref. [88]. A positive impurity in the substrate will constitute a repulsive potential for holes (a barrier for holes
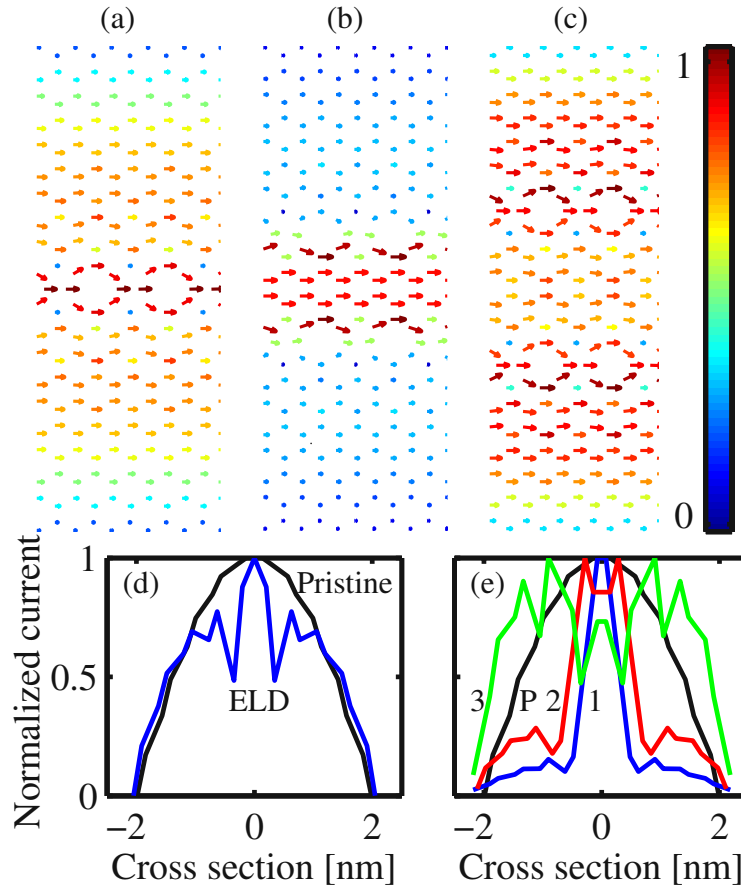
Figure 3.21: Normalized current spectrum at $E = 0.2$ eV for (a) ELD-ZGNR(10,10), (b) 2ELD-ZGNR(8,4,8), and (c) 2ELD(7,6,7). (d) The current in the cross section of ZGNR(20) (black line) and ELD-ZGNR(10,10) (blue line). (e) The current in the cross section of ZGNR(20) (black line), 2ELD-ZGNR(9,2,9) (blue line), 2ELD-ZGNR(8,4,8) (red line), and 2ELD-ZGNR(7,6,7) (green line).

but a well for electrons) and will degrade hole transport more effectively than electron transport. Figure. 3.22-a shows how the transmission of the ELD-ZGNR(10,10) channel (dashed-black line) is affected after the introduction of positive charged impurities in the channel (solid-blue line). Indeed, the transmission of holes below the Fermi level ($E = 0$ eV) is degraded. This effect additionally increases the asymmetry of the propagating bands and improves the Seebeck coefficient. On the other hand, the opposite is observed when negative impurities are introduced in the substrate. Negative impurities are a barrier for electrons and reduce their transmission [94], but do not interfere with the hole subsystem as shown in Fig. 3.22-b. This type of impurities will actually harm the asymmetry and needs to be avoided.
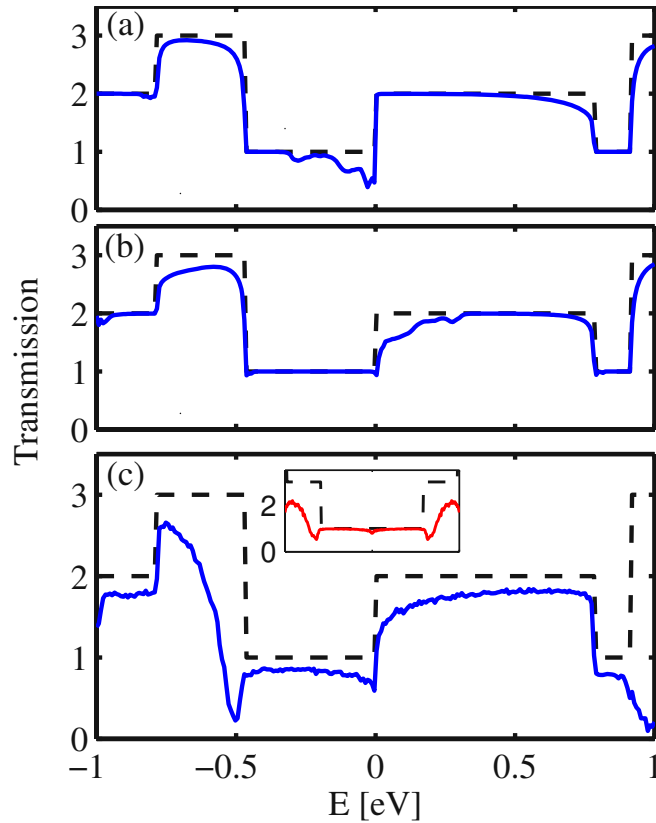
Figure 3.22: The effect of (a) positive substrate impurity, (b) negative substrate impurity, and (c) roughness on the transmission of ELD-ZGNR(10,10) with length of 125 nm. Inset of (c): The transmission of ZGNR(20) in the presence of roughness.

3.3.3 The Role of Line-Edge-Roughness

In the third step of the design process the effect of edge roughness is introduced. The inset of Fig. 3.22-c shows the influence of edge roughness on the transmission of the ZGNR(20) of length 125 nm. As also described in previous studies [19, 88], in the first conduction plateau the effect is negligible. In contrast to ZGNR, ELD-ZGNRs as well as 2ELD-ZGNRs are affected by edge roughness. This is because the bandstructure of these GNRs has undergone a band folding, and therefore, the states in the first conduction plateau have lower wave vectors. As the long range defects can induce only a small momentum transfer, the momentum conservation rule indicates that, in contrast to the ZGNR, the transport of ELD-ZGNRs and 2ELD-ZGNRs will not remain ballistic in the presence of line edge roughness and long range substrate impurities. This is shown in Fig. 3.22-c, where the transmission of a roughened 125 nm long ELD-ZGNR(10,10) channel (solid-blue line) is reduced by $\sim 25\%$ compared to the ballistic value (dashed-black line). Edge roughness degrades the conductivity of
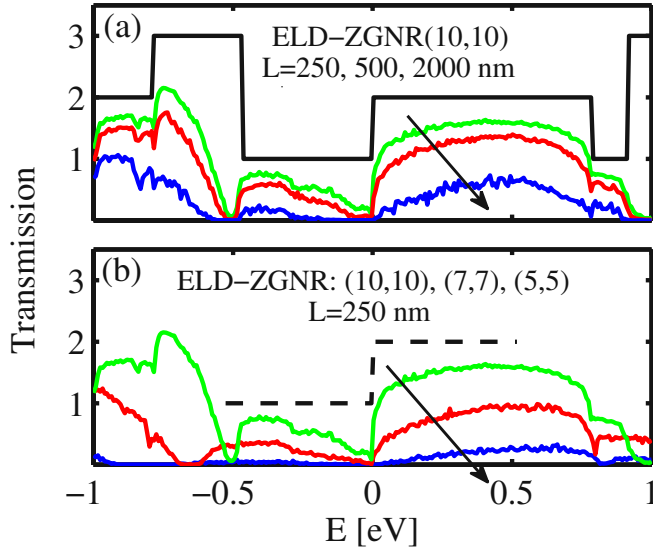
Figure 3.23: The influence of roughness and positive impurities on the ELD-ZGNR channel. (a) Electronic transmission of ELD-ZGNR(10,10). Rough edges are assumed and the length L is varied. The arrow indicates increasing values of length L. (b) Electronic transmission of ELD-ZGNRs with different widths. The length is assumed to be constant at 250 nm and the arrow indicates the direction of decreasing the ribbon's width. Black-solid and black-dashed lines in (a) and (b): The transmission of the pristine ELD-ZGNR.

holes and electrons by a similar amount, and therefore, the level of asymmetry around the Fermi level is retained.

Figures 3.23-a and 3.23-b illustrate the influence of roughness in ELD-ZGNR channels on their transmission, for channels of different lengths and widths. In this calculation positive impurities are also included. Figure 3.23-a shows the transmission of edge roughened ELD-ZGNR(10,10) versus energy for the channel lengths $L = 250$, 500, and 2000 nm. As the channel length is increased, the transmission drops further compared to the transmission of the ideal channel (black-solid line). This is expected since the channel resistance increases with increasing length. Figure 3.23-b illustrates the effect of the ribbon's width on the transmission of ELD-ZGNRs with rough edges. In this case the length is kept constant at $L = 250$ nm, and results for three different ribbons with parameters (10,10), (7,7), and (5,5) are shown. As the width of the ribbon is decreased, the effect of line edge roughness scattering on the transmission becomes stronger because the carriers reside on average closer to the edges.

It is worth mentioning that the effect of edge roughness on the transmission is much stronger in AGNR than in ZGNR. Although in the case of some AGNRs a bandgap
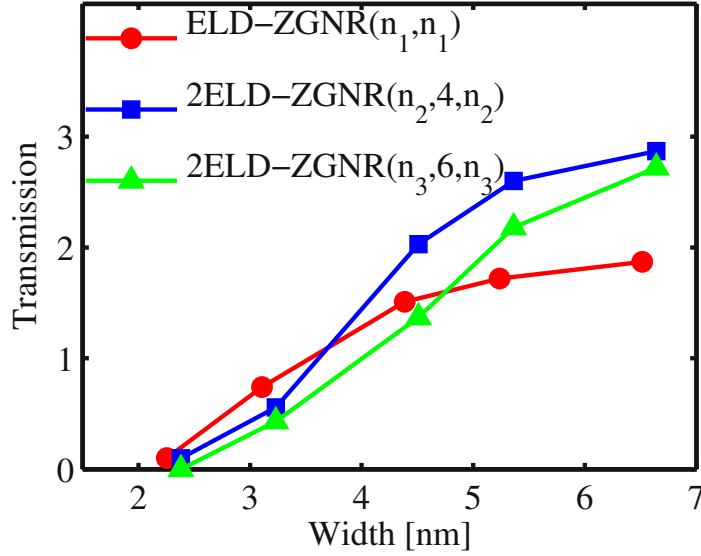
Figure 3.24: Transmission at $E = 0.2$ eV for three different structures versus width. The length is assumed to be constant at 250 nm.

is naturally present and the asymmetry need not be created with the introduction of line defects and impurities, the conductance is severely degraded by the roughness which renders this type of ribbon not well suited for transport applications [88]. (Note that edge roughness will be needed in order to reduce thermal conductivity as will be shown below.)

As we mentioned above in Fig. 3.21, the channel which includes two ELDs can shift the majority of the current spectrum in the region between the two ELDs, and thus farther away from the edges. It is therefore expected that the 2ELD-ZGNR will be less affected by edge roughness scattering than the ELD-ZGNR. A comparison of the transmission of these devices with rough edges is shown in Fig. 3.24. The transmission of ELD-ZGNR(n_1,n_1), and two cases of 2ELD-ZGNR, 2ELD-ZGNR(n_2,4,n_2) and the 2ELD-ZGNR(n_3,6,n_3) at $E = 0.2$ eV versus their width W are compared. The parameters n_i are adjusted such that the three channels have nearly the same width W. The first channel belongs to the category shown in Fig. 3.21-a, the second in the category of Fig. 3.21-b, and the third in the category of Fig. 3.21-c. The third channel as shown in Fig. 3.21 spreads the current spectrum more uniformly in the channel and is expected to be affected the most from edge roughness. All channels have the same length of $L = 250$ nm. For smaller widths the effect of roughness is strong, and the transmissions of all channels are drastically reduced. Since the 2ELD-ZGNR devices can concentrate the current spectrum around the defect lines as shown in Fig. 3.21-b and 3.21-c, they effectively bring it closer to the edges and the reduction is larger for these devices. For larger widths the transmission of the ribbons approaches its ballistic value, which is 2 for the ELD-ZGNR devices and 3 for the 2ELD-ZGNR devices. The

transmission of the 2ELD-ZGNR(n_2,4,n_2) channels increases faster with increasing channel width, because the current spectrum is located farther from the edges which makes it less susceptible to scattering as the width increases. The transmission of 2ELD-ZGNR(n_3,6,n_3) channel eventually increases close to the ballistic transmission value as the width increases, but it increases more slowly than that of the 2ELD-ZGNR(n_2,4,n_2) channel.

3.3.4 The Effect of Roughness on Phonon Transport

The high thermal conductivity of graphene is mostly due to the lattice contribution, whereas the electronic contribution is much smaller [28, 29]. In order to reduce the thermal conductivity, therefore, the focus is placed on reducing phonon conduction. Although the reduction in the electronic transmission of channels with ELDs can be quite strong when considering edge roughness, the reduction in the lattice part of the thermal conductivity is even stronger. One can take advantage of this effect when attempting to optimize the thermoelectric figure of merit.

For the phonon modes, the dynamic matrix is constructed using the fourth nearest-neighbor force constant model [83]. The force constant method uses a set of empirical fitting parameters and can be easily calibrated to experimental data. The fitting parameters given in Ref. [42] are used for graphene-based structures. Here, it is assumed that this model is still valid for structures that include ELDs. Although verification of its validity for ELD-ZGNRs has not been demonstrated yet, for instance using first-principle calculations, in Ref. [95] it was shown using DFT simulations that there is little difference between the phonon transmission of carbon nanotube structures with and without ELDs which could justify the model employed here. In any case, as shown below, the main influence on the phonon transport in this work originates from edge roughness scattering, which reduces the phonon transmission drastically. The effect of edge roughness scattering can be captured adequately by the model employed in this work. The influence of the ELDs on the phonon transmission is much smaller than the effect of edge roughness, and therefore usage of the numerically less expensive fourth nearest-neighbor force constant method is justified.

The phonon transmission for the edge roughened ELD-ZGNR(10,10) channel versus energy is shown in Fig. 3.25-a. Results for channel lengths $L = 10$, 100, and 2000 nm are shown. As expected, the transmission decreases as the length is increased. What is important, however, is that the decrease is much stronger than the decrease of the electron transmission shown in Fig. 3.23-a. For example, for a channel length of $L = 100$ nm the phonon transmission reduces by more than a factor of $6X$, whereas the electronic transmission even at larger length $L = 250$ nm reduces only by $< 30\%$. Interestingly, the same order of reduction of the phonon transmission is observed for the 2ELD-ZGNRs as shown in Fig. 3.25-b, indicating that the line defect does not affect phonon conduction significantly compared to the effect of edge roughness.
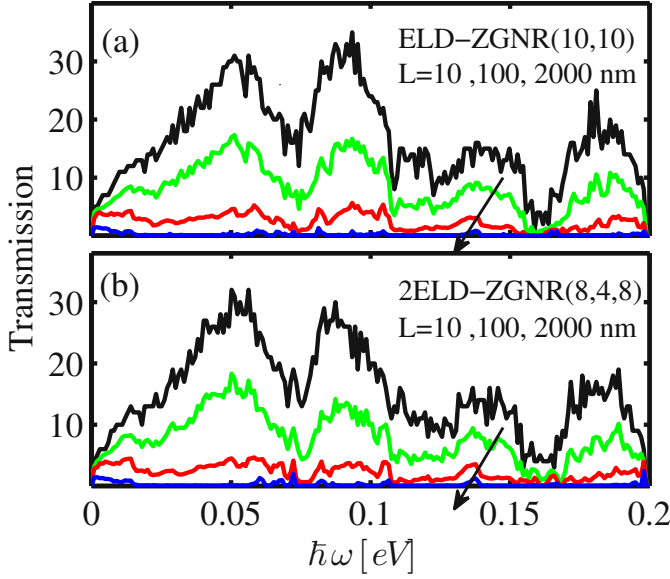
Figure 3.25: Phonon transmission function of (a) ELD-ZGNR(10,10) and (b) 2ELD-ZGNR(8,4,8). Rough edges are assumed and the length L of the channel is varied. The arrows indicate increasing values of channel length L: 10 nm (green), 100 nm (red), 2000 nm (blue). Black lines: The phonon transmission of the channels with line defects but without roughness.

The denominator of the ZT figure of merit consists of the sum of the contributions to the thermal conductivity of the electronic system and the phononic system. In graphene the phonon part dominates the thermal conductivity, whereas the electronic part contribution is much smaller. The situation is different, however, in rough ELD-ZGNRs, in which the phonon thermal conductivity is degraded more than the electronic thermal conductivity. Figure 3.26 clearly illustrates this effect by showing the ratio of the phonon thermal conductance to the electronic thermal conductance versus the rough channel length. The cases of ELD-ZGNR(10,10) and 2ELD-ZGNR(8,4,8) are shown in dashed-red and dash-dot-blue lines, respectively. For small channel lengths, where transport is quasi-ballistic and roughness does not affect the transmission significantly, K_{ph} is almost $5X$ larger than K_{el}. As the length of the channel increases and the effect of the roughness becomes significant, the phonon system is degraded more than the electronic system, and the K_{ph} is significantly reduced compared to K_{el}. For lengths $L \sim 100$ nm and beyond, K_{ph} can become even smaller than K_{el}. The trend is the same when considering channels with one or two ELDs.

The inset of Fig. 3.26 shows that the ratio of the electrical conductance G over K_{el} is almost constant, from which it can be indicated that both G and K_{el} follow the same trend, as dictated by the Wiedemann-Franz law. The K_{ph} and K_{el} values used in Fig. 3.25 are extracted using the corresponding mean free paths (MFPs) for phonons and electrons respectively, defined as Eq. 3.2. Alternatively, K_{ph} and K_{el} could be

Die approbierte gedruckte Originalversion dieser Dissertation ist an der TU Wien Bibliothek verfügbar.
The approved original version of this doctoral thesis is available in print at TU Wien Bibliothek.
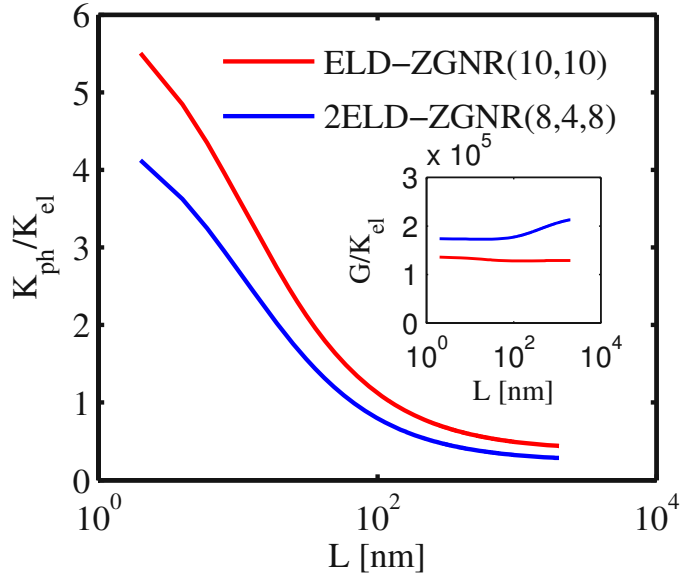
Figure 3.26: The ratio of the phononic to the electronic thermal conductivity versus cannel length L for the ELD and 2ELD structures as noted. Inset: The ratio of the electronic conductivity to the electronic part of the thermal conductivity versus channel length L.

extracted from the transmission calculations by using a statistical average over several rough samples for each channel length. The results of both methodologies are in good agreement for the electronic part of the thermal conductivity. For the lattice part, the agreement is good only for the shorter channels, below ~ 100 nm. For larger channel lengths, the phonon transmission is severely reduced which increases the relative statistical error in the calculation for extracting the K_{ph}. The values extracted directly from the integration of the average phonon transmission might be as much as $2X$ larger. In this case the ratio K_{ph}/K_{el} will be closer to unity, but this is still a huge advantage compared to devices without roughness.

3.3.5 Thermoelectric Figure of Merit

Using the first design step, i.e. the effect of ELDs, it was demonstrated that the transmission of electrons around the Fermi level can be increased (from $\overline{T} = 1$ to $\overline{T} = 2$ and $\overline{T} = 3$ in the presence of one and two ELDs, respectively). An asymmetry is thus created between holes and electrons. This increases both the conductance and the Seebeck coefficient of the channel as shown in Fig. 3.27. Figure 3.27-a shows the conductance of the 2ELD-ZGNR(8,4,8) (blue), of the ELD-ZGNR (10,10) (red), and of the pristine nanoribbon (green) at $300\ K$. As expected, the conductance of the channel with two ELDs is the largest, followed by the channel with one ELD.

Figure 3.27: (a) Electrical conductance, (b) Seebeck coefficient, and (c) thermoelectric power factor of pristine ZGNR(20), ELD-ZGNR(10,10), and 2ELD-ZGNR(8,4,8) channels with perfect edges . The dots indicate the Fermi energy values at which the peak of the power factor occurs for the ELD and 2ELD channels.

The conductances are larger than that of the pristine channel by $\sim 3X$ and $\sim 2X$, respectively. Figure 3.27-b shows the changes of the Seebeck coefficient after the introduction of the ELDs in the nanoribbon. Due to its metallic behavior and the flat transmission near the Fermi level, the pristine channel exhibits zero Seebeck coefficient. Due to the asymmetry built up after the introduction of the ELDs, however, the Seebeck coefficient increases for both channels. The channel with two line defects has the largest asymmetry, and therefore the largest Seebeck coefficient (in absolute values). Finally, the power factor in Fig. 3.27-c is indeed largely improved in the ELD structures, and especially the 2ELD-ZGNR channel.

In Figure 3.28 the same thermoelectric coefficients for the same structures as in Fig. 3.27 are shown, but now edge roughness and positive impurities are included
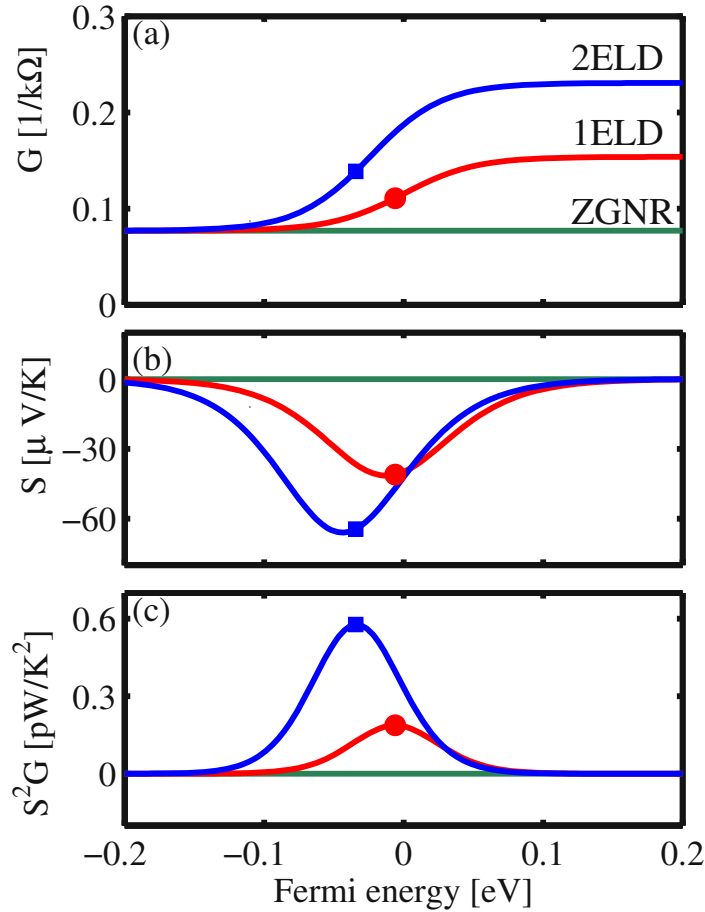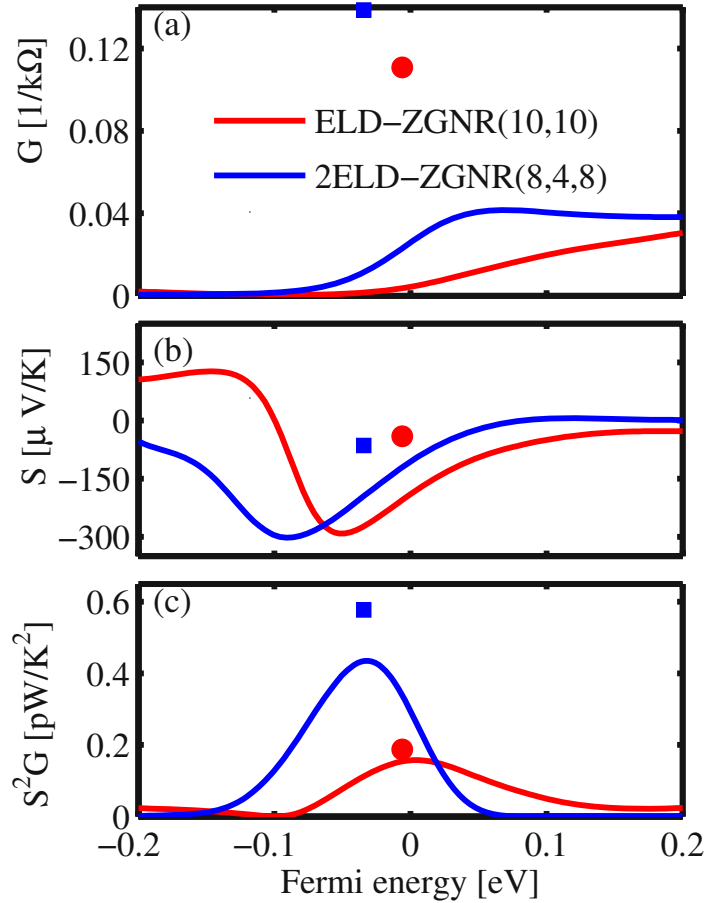
Figure 3.28: (a) Electrical conductance, (b) Seebeck coefficient, and (c) thermoelectric power factor of ELD-ZGNR(10,10) and 2ELD-ZGNR(8,4,8) with rough edges and positively charged substrate impurities. The channel length is 2 μm. The dots indicate the Fermi energy values at which the peak of the power factor occurs for the pristine ELD and 2ELD channels of Fig. 3.27.

in the calculation. The length of the channels in this case is 2000 nm. A similar qualitative behavior is observed as in Fig. 3.27 for both channels. Quantitatively, however, the conductance in Fig. 3.28-a is now significantly reduced by a factor of $\sim 15X$ (the dots correspond to the position of the peak of the power factor of the devices without roughness and impurities in Fig. 3.27). The Seebeck coefficient in Fig. 3.28-b, on the other hand increases. Finally, the peak of the power factor in Fig. 3.28-c reduces only slightly compared to the peak of the power factor of the devices without edge roughness in Fig. 3.27-c (dots).

For the devices that include rough edges, however, as demonstrated in Fig. 3.26, the phonon thermal conductivity is drastically reduced compared to the electronic thermal conductivity. A large improvement in ZT is therefore expected. Figure 3.29
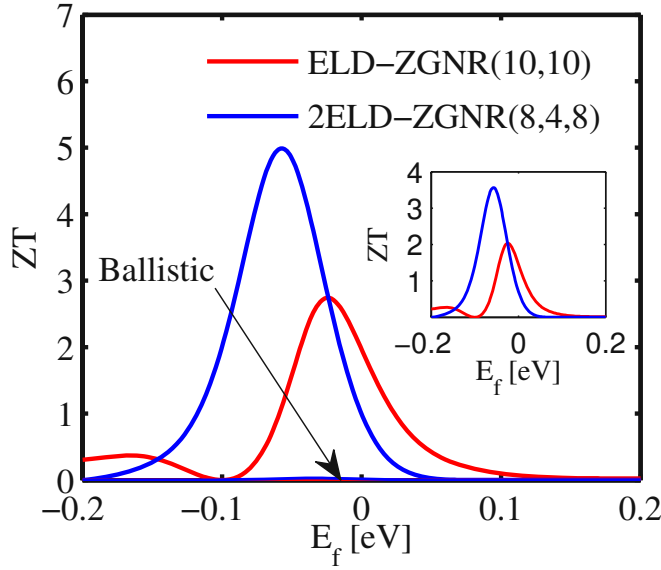
Figure 3.29: The thermoelectric figure of merit ZT for the ELD-ZGNR(10,10) (red line) and 2ELD-ZGNR(8,4,8) (blue line) channels of length $L = 2\ \mu m$. The lattice thermal conductance is extracted from the calculated mean free path. Inset: The same figure of merit ZT but with the lattice thermal conductance extracted by integrating the simulated phonon transmission.

shows ZT versus energy at room temperature for the ELD-ZGNR(10,10), the ELD-ZGNR(10,10) with impurities and roughness (red), and the 2ELD-ZGNR(8,4,8) (blue) with impurities and roughness. As indicated, large values of ZT can be achieved, especially in the case of the device with two ELDs. The phonon lattice conductivity value used in this calculation was extracted using the MFP method. As explained in Sec. 3.3.4, that value could be $2X$ lower than the value extracted from direct integration of the simulated phonon transmission. In the inset of Fig. 3.29 the ZT versus energy using the κ_l values extracted from the transmission are shown. Indeed the values might be reduced by a factor of $\sim 2X$, but still peak ZT values above 2 can be achieved at room temperature, which is comparable and even better than the best thermoelectric materials to date [96]. It is worth mentioning that as shown by Ref. [19] rough ZGNRs can have high ZT values even without the presence of ELDs. For this the asymmetry in the sharp edges of the higher subbands is utilized at energies above 0.5 eV. Those energies however, are too high and can not easily be reached. Finally it is necessary to mention here that the formalism has considered scattering only by edge roughness and impurity scattering, whereas phonon scattering and dephasing mechanisms are not included. However, as it is shown for 1D nanowires [97], the effects of impurity scattering and edge roughness are the most important scattering effects in channels of cross sections below 5 nm, and one can expect this to hold also for GNRs as well.

4 Ballistic Thermal Properties of Silicon-Based Nanostructures

Low dimensional silicon materials, such as nanowires and ultra-thin layers have demonstrated record low thermal conductivities of $1 - 2$ W/mK, reaching the amorphous limit. This resulted in ZT values close to $ZT \sim 0.5$, a large improvement compared to bulk silicon with $ZT_{\text{Bulk}} \sim 0.01$ [17, 20]. Although the two order of magnitude reduction in the thermal conductivity is attributed to boundary scattering of phonons, an additional reduction can be achieved from changes in the phonon mode structure due to geometrical confinement. In this chapter, the effect of confinement and orientation on the phonon transport properties of silicon-based nanostructures of various surface and transport orientations are investigated. To this aim, the density of states, the transmission function, the sound velocity, and the ballistic thermal conductance of silicon-based ultra-thin layers and narrow nanowires are extracted. The lattice dynamics is, here, modeled by the modified valence force field method and the ballistic Landauer transport formalism is employed to calculate the thermal conductance.

4.1 Silicon Nanowires

Numerous studies can be found in the literature regarding the thermal conductivity of silicon nanowires [98–102]. The effects of different scattering mechanisms, i.e. surface roughness scattering, mass doping, phonon-phonon scattering, and phonon-electron scattering have been investigated by several authors [103–106]. In these works, it is demonstrated that the thermal conductivity in ultra-narrow silicon nanowires drastically degrades once the diameter of the nanowire is reduced below 50 nm, or when scattering centers are incorporated. For even smaller nanowire diameters, i.e. below 10 nm, the effect of confinement could further change the phonon spectrum significantly, and provide an additional mechanism in the reduction of the thermal conductivity [107]. This could provide additional benefits to the thermoelectric figure of merit ZT. In this section, we employ the modified valence force field method [45] to address the effect of structural confinement on the phonon dispersion, group velocity and ballistic thermal conductance of ultra-narrow silicon nanowires of diameters below 10 nm. We consider different transport orientations, and different cross sectional sizes (square cross sections $W = H$).
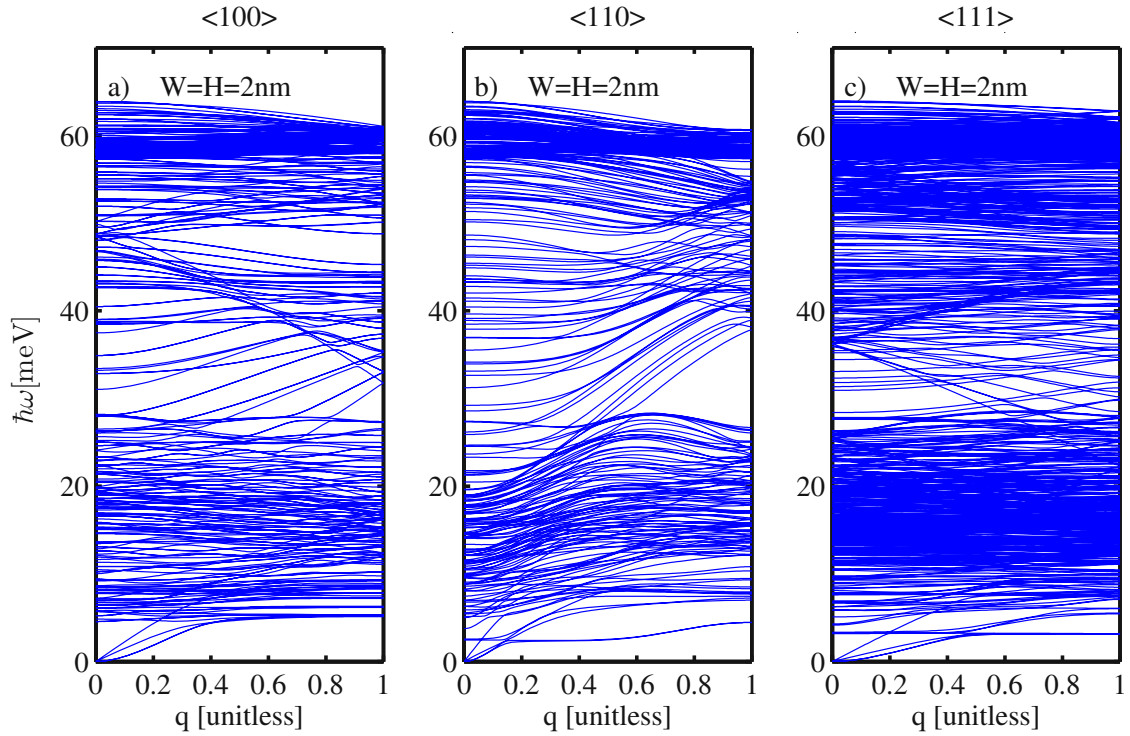
Figure 4.1: Phononic dispersions of silicon nanowires of square cross sections with $W = H = 2$ nm for a) <100>, b) <110>, and c) <111> transport orientations.

4.1.1 Anisotropy in Ultra-Narrow Silicon Nanowires

The phononic dispersions of silicon nanowires of 2 nm $\times 2$ nm cross section for different transport orientations are shown in Fig. 4.1. There are differences in the dispersions, especially in the low energy, low momentum region, which indicate that the thermal properties could be orientation-dependent as well. Figure 4.2 shows the ballistic transmission function of nanowires with side sizes $W = H = 6$ nm for three orientations. The transmission function of the <110> nanowires is the highest in most part of the energy spectrum, whereas the transmission of the <111> nanowires is the lowest in almost the entire energy spectrum. As a result, the ballistic lattice thermal conductance of the nanowires (see Fig. 4.3-a) shows that the <110> nanowires has the highest thermal conductance compared to the <100> and <111> nanowires.

The thermal conductance is larger for the <110> nanowires of all the side sizes we have considered, up to 10 nm as shown in Fig. 4.3-a. The difference between the thermal conductances of the <110> nanowire, which has the highest, and the <111> nanowire which has the lowest, is a factor of ~ 2. Another observation is that the thermal conductance increases as the cross section of the nanowire increases. This is expected since the larger nanowires contain more transport modes. The increase is
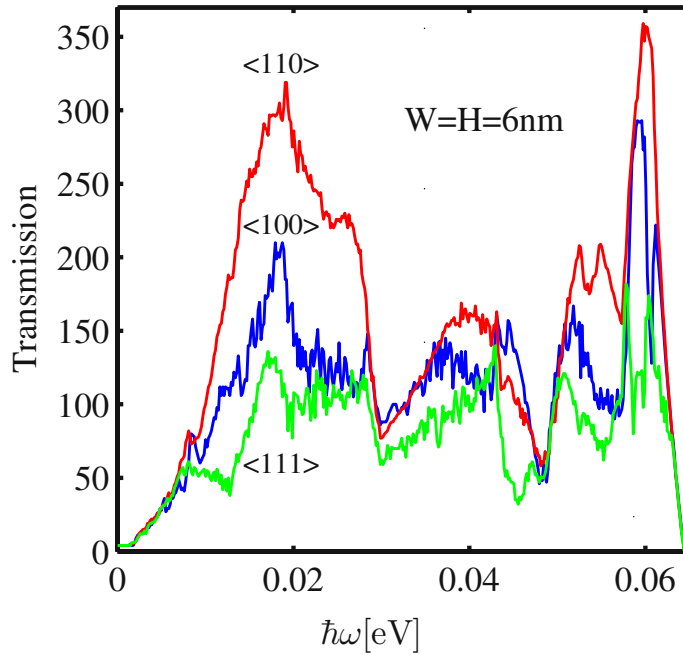
Figure 4.2: Transmission function versus energy for nanowires in different transport orientations. <110> nanowires have the highest and <111> nanowires the lowest transmission.

close to linear. Once the conductances are normalized by the cross section area of the nanowires, however, the resultant normalized conductances remain almost constant. This is indicated in the Fig. 4.3-b. In this case, again, the <111> nanowire has clearly the lowest conductivity, almost 2 times lower than the <110> nanowire for all cross section sizes. In the next section, the reasons behind the anisotropy of the thermal conductance and conductivity are elucidated in terms of the nanowires phonon bandstructure and its related quantities.

4.1.2 Phonon Properties of Ultra-Narrow Silicon Nanowires

The ballistic transmission function is directly related to the product of the density of phonon states and phonon group velocity. Below, each of these quantities and their geometry dependence is investigated in order to provide insight into the orientation dependence of the thermal conductance. For this, nanowires with $W = H = 6$ nm in the three different orientations are considered. Figure 4.4 shows the phonon density of states, which is nearly the same for all orientations in the entire range of frequencies. This can be understood by considering the fact that the density of states is mostly related to the density of atoms in the cross section of the nanowires. The density of atoms is mostly a bulk property and does not change drastically in silicon-based
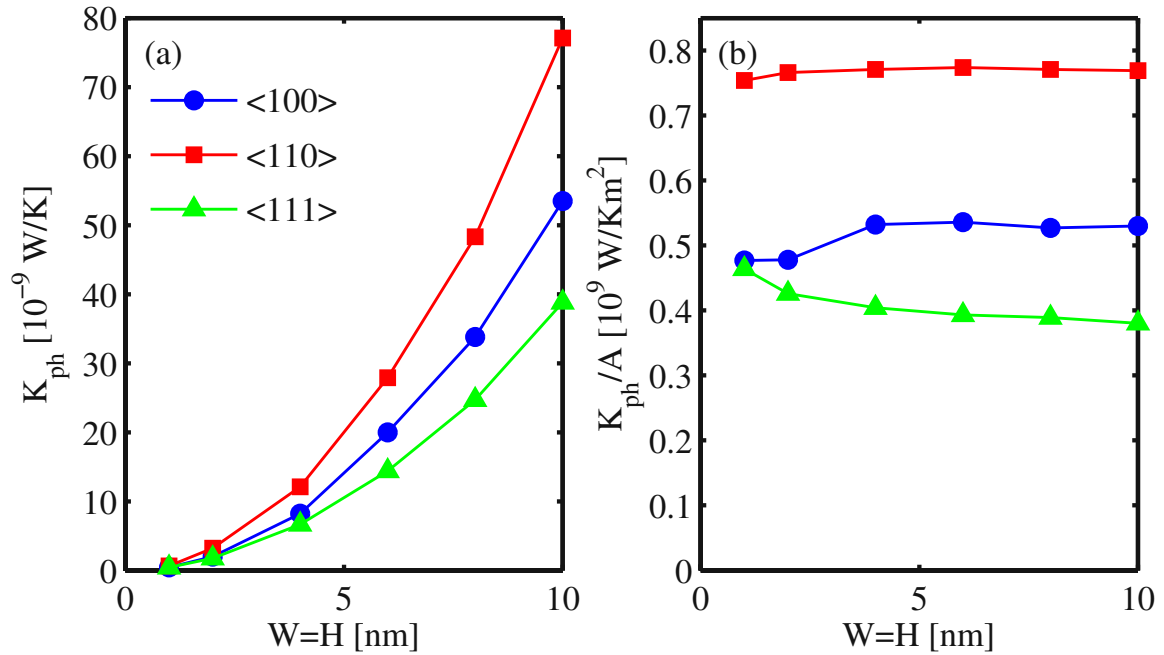
Figure 4.3: (a) Ballistic lattice thermal conductance versus nanowires cross section side size for nanowires in different orientations. (b) The thermal conductance normalized by the cross section area.

structures. Each atom has three degrees of freedom (3×3 elements in its dynamic matrix component), and therefore provides three eigenmodes. Although for ultra-narrow structures i.e. of 2 nm $\times$ 2 nm there could be some differences in the density of states due to finite size effects, a 6 nm $\times$ 6 nm structure is large enough such that the density of states is orientation independent.

On the other hand, as shown in Fig. 4.5, the sound velocity, defined by the slope of the acoustic modes near the Brillouin zone center, is a non-isotropic quantity. The two lowest modes in the phonon dispersion of nanowires are flexural modes. The third mode is the one used to calculate the transverse sound velocity, whereas the fourth mode gives the longitudinal sound velocity. The results, as shown in Fig. 4.5, are in good agreement with previous studies on nanowire sound velocities [39, 108]. The <111> nanowire has the highest longitudinal sound velocity (green-solid), whereas the <100> nanowire the lowest for all cross section sizes. The transverse velocities are lower, and in that case, the <100> nanowire has the highest velocity. The values calculated here are different, and in general lower than the bulk sound velocities (Symbols at the right axis of Fig. 4.5). The velocities in nanowires are lower, also in agreement with other reports, since confinement flattens the phonon spectrum and reduces sound velocities [109].

At first, following a bulk way of analysis, it seems that according to the ordering in
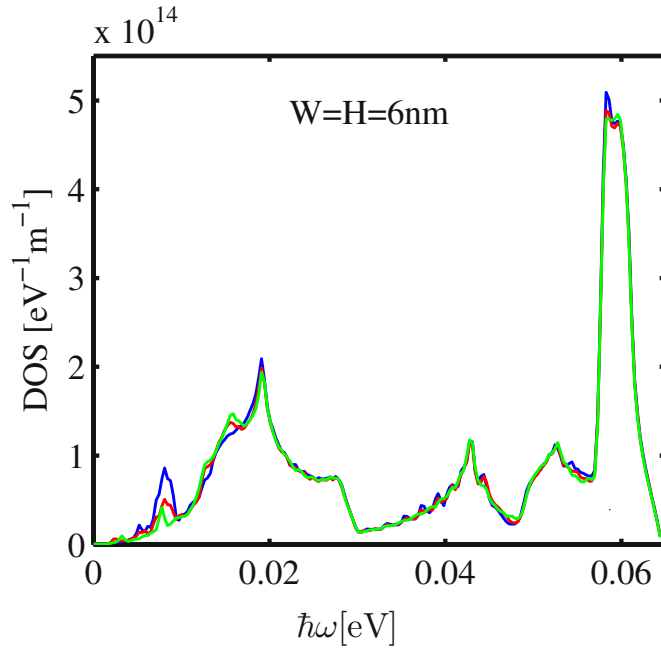
Figure 4.4: The phonon density of states versus frequency for nanowires in different orientations. The density of states is nearly the same for the different transport orientations.

the sound velocity one would expect that the thermal conductance should be higher in the <111> nanowires, followed by the <110> nanowires and then by the <100> nanowires. As we show in Fig. 4.3, however, the order is different, namely that the <110> nanowires have the highest thermal conductance, followed by the <100>, and then by the <111> nanowires. The reason is that the phonon dispersion is modified in nanostructures so that the bulk definition of acoustic and optical modes is no longer the relevant quantity. The sound velocity determines the dispersion only in a small part of energy spectrum (~ 5 meV of out of the total ~ 65 meV). In addition, at room temperature, all the phonons in the entire energy spectrum contribute to the thermal conduction. Therefore, the sound velocity alone cannot describe the nanowire phonon spectrum, which is an indication that the bulk treatment is insufficient for understanding thermal transport in nanowires. What needs to be taken into consideration in order to correctly interpret the results, therefore, is the group velocity of all phonon modes at all energies. For this, we define the average group velocity as follows:

$$<<v_g>> = \frac{\sum_{\alpha,\vec{q}} v_\alpha(\vec{q})|_\parallel \delta(\omega - \omega_\alpha(\vec{q}))}{\sum_{\alpha,\vec{q}} \delta(\omega - \omega_\alpha(\vec{q}))} \qquad (4.1)$$

where the sum holds over all the modes. The velocity of a phonon is in general a function of the subband index, the frequency, and the wave vector. The quantity in
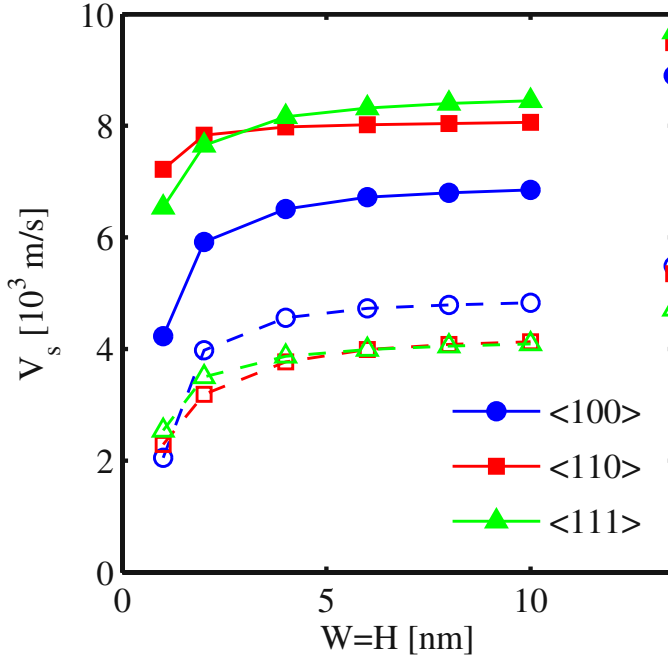
Figure 4.5: The sound velocity of nanowires in different orientations versus the nanowire side size. Longitudinal and transverse velocities are shown in solid and dashed lines, respectively. Symbols at the right axis indicate the respective bulk silicon velocities.

Eq. 4.1 effectively suppresses the subband and $\vec{q}$-point indices and provides a quantity that is only frequency (or energy) dependent. Similar effective quantities are also used in actual thermal conductivity calculations with adequate accuracy in the results [103, 110], although in our actual calculations we utilize all the information of the phonon spectrum.

In contrast to the sound velocity, the average weighted group velocity over different modes can provide a better and more correct insight with regards to phonon transport. Figure 4.6 shows that the average group velocity of phonons for the <110> nanowires is the highest compared to the other orientations in the largest part of the energy spectrum. This can be explained by the shape of the dispersions shown in Fig. 4.1. In the case of the <111> nanowire, the modes look overall less dispersive, i.e. have less curvature. This results in the lowest average group velocity. The modes of the <110> nanowire, on the other hand, are more dispersive, i.e. have more curvature, which results in the highest group velocity. By considering that all nanowires with the same cross sectional area have the same phonon density of states, the differences in the group velocity explain the orientation-dependence observed in the transmission functions and in the thermal conductance shown in Fig. 4.2 and Fig. 4.3, respectively. The transmission function of the <111> nanowire is $\sim 1.25x$ lower than that of the

74
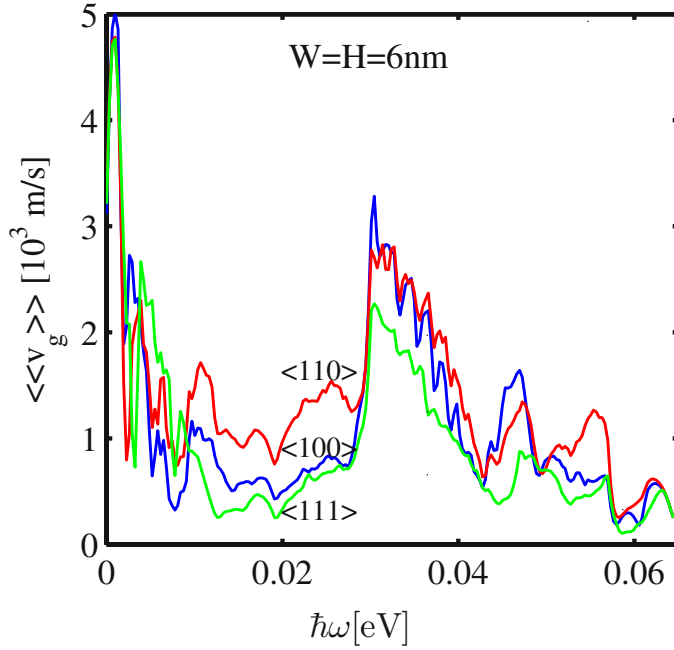
Figure 4.6: Average phonon group velocity of nanowires in different transport orientations versus frequency.

<100> nanowires and almost 2x lower than that of the <110> nanowires.

4.1.3 Discussion

In this section we have studied the thermal properties of ultra-narrow silicon nanowires using the atomistic MVFF method for the computation of the phonon bandstructure. We have extracted the thermal properties using the ballistic Landauer formalism. We have addressed the effects of structural confinement on the phonon dispersion, the phononic density of states, the phononic transmission function, the sound velocity, and the effective group velocity. Our results show that differently oriented nanowires can have up to a factor of two difference in their effective group velocity, transmission function, and ballistic thermal conductance. The <110>-oriented nanowire has the highest ballistic thermal conductance, followed by the <100> and finally the <111> nanowire.

Neophytou et al. have recently studied the role of transport orientations and diameter on the thermoelectric power factor of nanowires using atomistic calculations of the electronic bandstructure [97]. In the case of n-type nanowires only a small orientation-dependence of the electric power factor was observed. In the case of
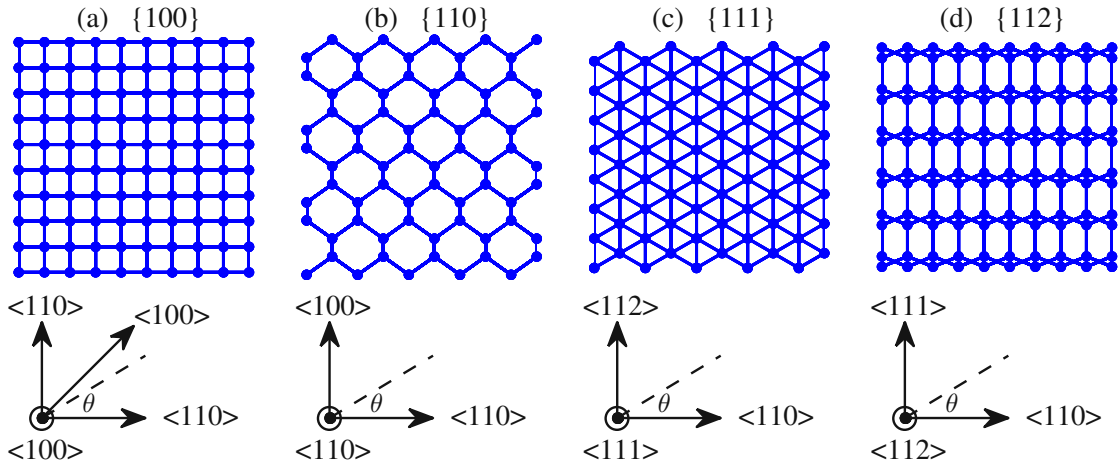
Figure 4.7: The atomistic structure of the cross sections of the different thin silicon layers investigated (a) {100}, (b) {110}, (c) {111}, and (d) {112} surface. In all cases the x-axis is along the $<110>$ transport direction. Transport orientations θ varies between 0 and π.

p-type silicon nanowires, however, they showed that $<111>$ nanowires have significantly higher power factors than differently orientated nanowires. The $<111>$ silicon nanowire channel is, therefore, the most advantageous for p-type thermoelectric applications, since it simultaneously provides the highest power factor and lowest thermal conductance compared with other transport orientations.

4.2 Silicon Thin Layers

In this section, the effects of confinement and orientation on the phonon transport properties of ultra-thin silicon layers of various surface and transport orientations are investigated. Figure 4.7 shows the geometrical cross sections of the thin-layers considered. The layers have {100}, {110}, {111}, and {112} surface orientations. In all cases, we consider the x-axis to be parallel to the $<110>$ orientation, and define the angle θ of the transport direction counter-clockwise from the x-axis. Below, a complete analysis is presented by calculating the phononic properties and thermal conductance as a function of the angle θ for the four surface orientations mentioned. The layer thickness H varies from 1 to 16 nm. The phononic dispersion, density of states, ballistic transmission, and effective group velocity of the different structures are calculated.
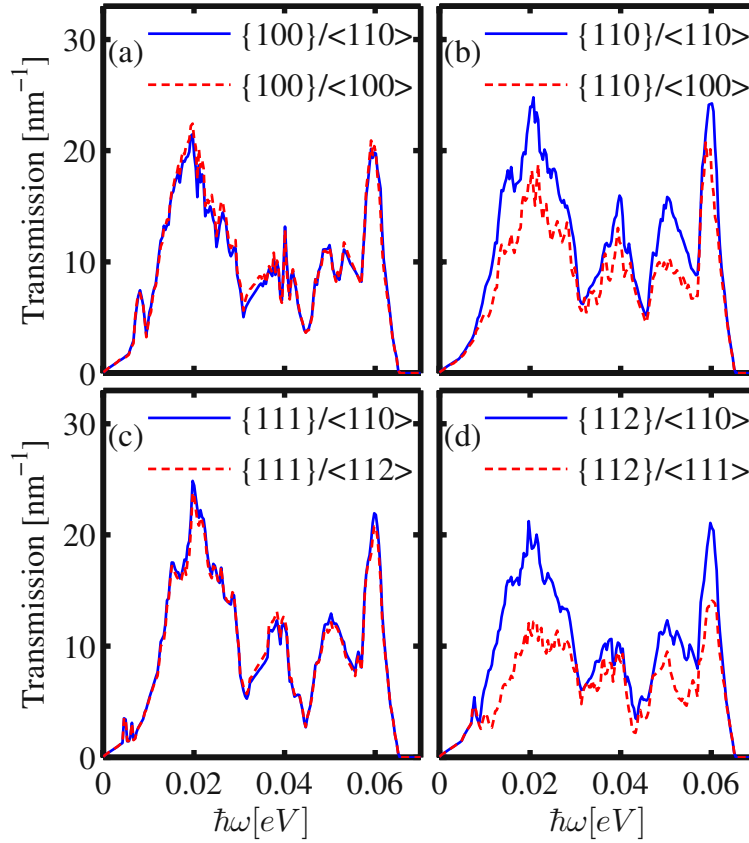
Figure 4.8: Transmission function versus energy for thin-layers of thickness H=2nm with (a) {100}, (b) {110}, (c) {111}, and (d) {112} surfaces, for two transport orientations in each case. The different transport orientations are the ones that yield the highest (blue-solid) and the lowest (red-dashed) thermal conductance for the corresponding surface orientation.

4.2.1 Anisotropy in Ultra-Thin Silicon Layers

Figure 4.8 shows the transmission functions for the four surface orientations of interest along two particular transport orientations for each case, that, as shown below, provide the lowest and the highest thermal conductance for that particular surface. The layer thickness in all cases is 2 nm. In the case of the thin-layer with {100} surface orientation, in Fig. 4.8-a we consider the {100}/<110> and the {100}/<100> transport channels. The transmissions of the two channels are almost the same, indicating negligible anisotropy. In the case of the thin-layer with {111} surface orientation, in Fig. 4.8-c we consider the {111}/<110> and the {111}/<112> transport channels. Again in this case, the transmissions are almost the same.

The transmission function of the thin-layers with {110} and {112} surfaces, on the other hand, is orientation-dependent. For the {110} surface thin-layers in Fig. 4.8-b,

the {110}/<110> channel (blue line) shows the highest transmission function, and the {110}/<100> channel (red-dotted line) the lowest. An even larger difference is observed in the case of the {112} surface thin-layers in Fig. 4.8-d. The highest transmission is observed for the {112}/<110> channel (blue line), and the lowest for the {112}/<111> channel (red-dotted line). The difference in the transmission of the channels in different transport orientations is largest for energies between $10-30$ meV for both the {110} and the {112} thin-layers.

Using the transmission functions extracted from the bandstructures, the ballistic lattice thermal conductance is calculated using the Landauer formula for the thin layers with the four different surface orientations of interest. The thermal conductance as a function of the transport orientation θ, varying from 0 to π is shown in Fig. 4.9 for room temperature. We calculate the conductance of thin layers for thicknesses of 1, 4, 8 and 16 nm. With symbols the high symmetry orientations are denoted using the Miller index notation, i.e. <110> - circle, <111> - star, <112> - triangle, and <100> - square. These orientations are marked on the 16 nm thin-layer result in Fig. 4.9. In all cases, the conductance increases linearly as the thickness increases because the thicker layers contain more phonon modes that contribute to the thermal conductance.

With regards to anisotropy, for the thin-layers with {100} surface in Fig. 4.9-a, the conductance has a maximum along the <100> direction (square), and a minimum is along the <110> direction (circle), although the difference is small (only $\sim 5\%$). Interestingly, this observation is the same for all thicknesses considered. The conductance of the channels with {110} surface is shown in Fig. 4.9-b. The conductance is biggest in the <110> transport orientation ($\theta = 0$, circle) and smallest for the <100> channels ($\theta = \pi/2$, square). The variation between the maximum and minimum values, however, in this case is $\sim 30\%$ for the 1 nm thin layer, and decreases to $\sim 20\%$ for the 16 nm layer. The conductance of channels with {111} surface is shown in Fig.4.9-c. The conductance in this case also peaks along the <110> direction (circle) and is smallest along the <112> direction (triangle). The variation of the conductance with transport orientation in this case is negligible for the thinner layers, but increases to $\sim 10\%$ in the 16 nm case. The thermal conductance for channels with {112} surface is shown in Fig. 4.9-d. The maximum and minimum conductance is observed along <110> (circle) and <111> (star), respectively. Channels with this surface orientation exhibit the largest variation in thermal conductance compared to other surfaces. The difference varies from $\sim 40\%$ for the 1 nm layers to $\sim 30\%$ for the 16 nm layers. Overall, considering all surface and transport orientations, the maximum thermal conductance is observed for the {110}/<110> channels, and the minimum for the {112}/<111> channels. Interestingly, however, regardless of surface orientation, the thermal conductance is high in <110> direction. This agrees well with previous works on silicon nanowires, where it is reported that the <110> oriented nanowires have the highest thermal conductance [107, 111]. A similar conclusion was found for thin layers of larger sizes [112]. As it will be explained in next section, the phonon dispersions
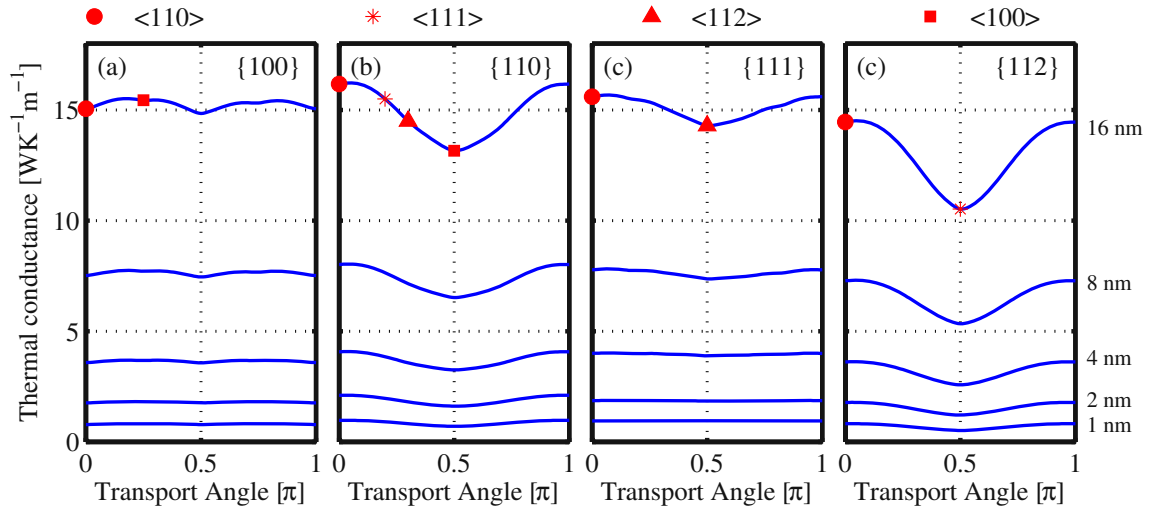
Figure 4.9: Ballistic lattice thermal conductance for different thin-layers with (a) {100}, (b) {110}, (c) {111}, and (d) {112} surfaces. The angle θ as shown in Fig. 4.7 specifies the transport orientation. Some of the high symmetry orientations are denoted by symbols. Results for different layers thicknesses are shown. From bottom to top, the thicknesses are 1, 2, 4, 8, and 16 nm.

along the <110> orientations are more dispersive compared to other orientations, which yield higher group velocities and, therefore, higher thermal conductance.

Figure 4.10 shows the thermal conductance of the $H = 2$ nm layers as a function of temperature. For every surface orientation two transport orientations, the one with the maximum and the one with the minimum conductance are shown (as in Fig. 4.8). The conductance increases with temperature as expected from a ballistic quantity, and starts to saturate around 300 K. The reason is that the phononic window function [57]:

$$W_{\mathrm{ph}} = \frac{3}{\pi^2} \left(\frac{\hbar\omega}{k_{\mathrm{B}}T} \right)^2 \frac{\partial n}{\partial(\hbar\omega)} \tag{4.2}$$

which weights the contribution of phonons with different energy, is nearly constant within the entire phonon energy spectrum of silicon (~ 65 meV) for sufficiently high temperatures. This causes the thermal conductance to saturate. Figure 4.10 shows that the {110}/<110> channel has the largest conductance, and the {112}/<111> channel the smallest in the entire temperature range. The conductances of the other channels lie in between and do not deviate significantly from one another. The same trend is observed for the $H = 16$ nm channels (inset of Fig. 4.10), although the spread is smaller. Below, explanations for this geometry dependence are provided in terms of the phonon bandstructure, by extracting the phonon density of states and the effective group velocity.
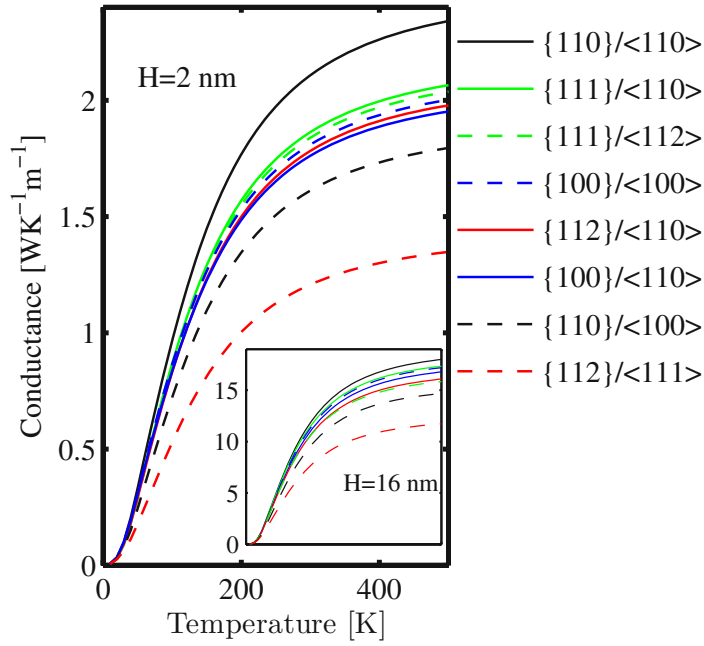
Figure 4.10: The thermal conductance of thin-layers of $H = 2$ nm for various surface and transport orientations, as a function of temperature. The transport orientations are the ones that result in the highest (solid) and lowest (dashed) thermal conductance for the respective surface orientation. Inset: The same quantity for thin-layers of $H = 16$ nm.

4.2.2 Analysis and Discussion

The ballistic phonon transmission function and thus the ballistic thermal conductance in the Landauer formalism are determined by the product of the density of states and the group velocity (Eq. 2.42). In Fig. 4.11 we plot the density of states for thin-layers of thickness $H = 2$ nm with four different surface orientations. Although some differences are observed for the different surface orientations, especially in the low frequency range, the overall values and trends are very similar. The inset of Fig. 4.11 shows the density of states for layers of thickness $H = 16$ nm. In this case a much smaller variation is observed as expected, since the phonon density of states depends on the number of atoms, and layers of the same thickness contain a similar amount of atoms. At smaller thicknesses the different arrangement of atoms can result in slightly different numbers of atoms for different surfaces, but as the thickness increases the crystal becomes more uniform and any variations are eliminated. In general, of course, the arrangement of atoms, the coupling between them, and the type of interactions they have can also influence their density of states. But as we show in Fig. 4.11, such effects on the density of states are only important at very thin sizes, i.e. $H = 2$ nm,
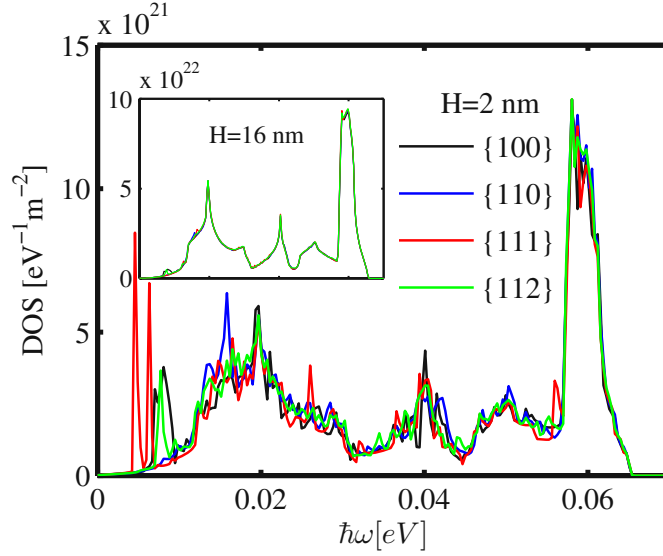
Figure 4.11: The density of phonon states for thin-layers of thickness $H = 2$ nm for different surface orientations. Inset: The density of phonon states for $H = 16$ nm thickness.

and even then, they are small. From this one can conclude that the variation in the thermal conductance and transmission does not originate from the difference in the density of states.

In Fig. 4.12 the effective group velocity defined in Eq. 4.1 is plotted. This quantity is orientation-dependent, in contrast to the density of states, and indicates how dispersive the modes are. The velocity $v_\alpha(\vec{q})|_\parallel$ is calculated along the transport direction. The density of states times the effective group velocity is proportional to the transmission function. Therefore, the differences in the transmission functions should be seen in the effective group velocities of the channels, since the density of states is the same for all channels of the same thickness. Figure 4.12 shows the effective group velocities of the channels considered. Figures 4.12-a and 4.12-c show the effective group velocities of thin-layers with {100} and {111} surfaces along the two different orientations with the lowest and highest thermal conductance for each surface orientation. The two different cases for each surface are almost identical, as in the case of the transmission functions in Fig. 4.8-a and 4.8-c. Figures 4.12-b and 4.12-d show the effective group velocities for channels with {110} and {112} surface orientations, respectively. A variation is observed for the different channels, which causes the difference in the transmission functions shown earlier in Fig. 4.8-b and 4.8-d.

The anisotropy of the effective group velocity originates from the phonon bandstructure. In Fig. 4.13 the contour plots of the phonon bandstructure at $E = \hbar\omega = 10$ meV is shown for the eight channels considered in Fig. 4.8 and Fig. 4.12 for layer thickness
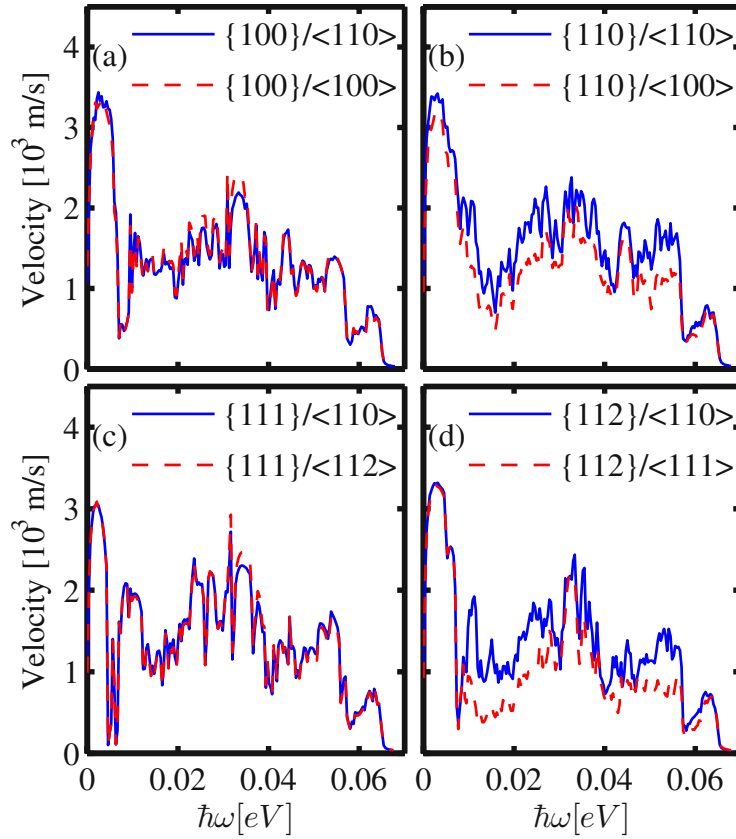
Figure 4.12: The effective group velocity versus energy for thin-layers of thickness $H = 2$ nm for (a) {100}, (b) {110}, (c) {111}, and (d) {112} surface orientations, for two transport orientations in each case. Those transport orientations are chosen that result in the highest (blue-solid) and the lowest (red-dashed) thermal conductance for the given surface orientation.

$H = 2$ nm. This is an energy value at which the most significant differences for the channels with {110} and {112} surfaces appear. It turns out that what is presented for this energy is a good indicator of the anisotropic behavior of the entire energy spectrum, most of which contributes to thermal conductance at room temperature. The lines represent the different modes at that energy, whereas the colormap indicates the cumulative ballistic thermal conductance at room temperature in the transport orientation of the specific channel of interest, as indicated by the arrow in each case. Elongation of contour lines along a specific direction provides high phonon group velocities in the perpendicular direction, and consequently high thermal conductance. This is very similar to the low effective mass and high velocities of carriers in an ellipsoidal band along the direction of the short axis.

Figures 4.13-a and 4.13-b show the energy contours for the {100} surface in the <110> and <100> transport orientations, respectively (indicated by the arrow). Despite the
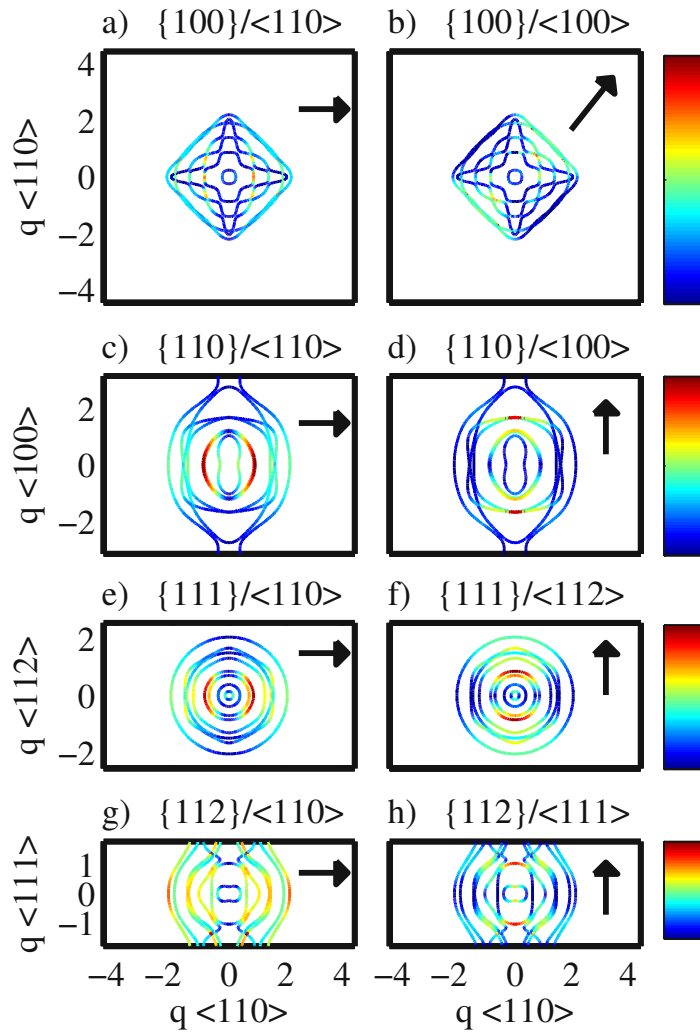
Figure 4.13: Energy contours at $E = 10$ meV for thin-layers of different surface and transport orientations. (a, b) {100} surface, (c, d) {110} surface, (e, f) {111} surface, (g, h) {112} surface. Those transport orientations are chosen that result in the highest (left) and the lowest (right) thermal conductance for the given surface orientation. The color indicates the cumulative thermal conductance at $E = 10$ meV at $T = 300$ K along the different transport orientations in each thin-layer (indicated by the arrow).

square like shape of the contour, which indicates that there is different symmetry in the two orientations of interest, the contours are elongated similarly in both directions, which results in a similar thermal conductance for both channels. This is the case for almost the entire energy spectrum (although at higher energies there are many more modes and more complex contour shapes). In the case of the {111} surface in

Fig. 4.13-e and 4.13-f, a highly symmetric contour provides very similar transmission functions and thermal conductances along the <110> and <112> directions.

The largest differences in the thermal conductance are observed for thin layers with {110} and {112} surfaces in Fig. 4.13-c, 4.13-d and Fig. 4.13-g, 4.13-h, respectively. In both cases, the contours at energy $E = 10$ meV are clearly elongated along the vertical axis. This results in a larger phonon group velocity along the horizontal axis, and finally a higher thermal conductance, as also indicated by the colormap. This is especially evident for the {112} surface, where the contour of the <110> channel in Fig. 4.13-g is colored much closer to red (higher conductance value) than the <111> channel in Fig. 4.13-h, indicating much larger phonon group velocities. This causes the thermal transmission and conductance of the {112}/<110> channel to be higher than that of the {112}/<111> channel shown in Fig. 4.8-d and Fig. 4.9-d.

Figure 4.13 explains the origin of anisotropy in the ballistic thermal conductance of thin-layers with 2nm thickness. However, such effects also hold for all the thicknesses examined, i.e. up to $H = 16$ nm. The anisotropic behavior depends weakly on the layer thickness. The ballistic conductance increases linearly as the layer thickness increases due to the increased number of atoms which results in a larger number of phonon modes, but the anisotropy does not change significantly. This is illustrated in Fig. 4.14-a which shows the ballistic thermal conductance for each of the four surface orientations examined, normalized by the thickness of the layer. For each surface only the direction showing the maximum conductance is considered. The results show that in all cases the normalized conductance is constant, even down to a thickness of $H \sim 5$ nm. Below $H \sim 5$ nm, variations of the order of $10 - 20\%$ are observed for all channels. From this, it follows that other than the reduction in the size of the phonon spectrum with thickness scaling, no significant changes in the shape of the phonon structure are observed, at least not significant enough to introduce changes in the thermal conductance. This is also supported by Fig. 4.14-b, which depicts the ratio of the maximum to the minimum thermal conductance that can be achieved for each surface. Similarly to Fig. 4.14-a, the anisotropy does not change with layer thickness even down to $H \sim 5$ nm. Again, below $H \sim 5$ nm, differences of the order of $10 - 20\%$ can be observed.

This anisotropy observed is not only a function of thickness, but also of temperature. Figure 4.15 shows the ratio of the maximum to the minimum ballistic thermal conductance for the four surface orientations of interest, again by choosing the appropriate transport orientations. Figure 4.15-a and 4.15-b show results for $H = 2$ nm and $H = 16$ nm, respectively. The maximum anisotropy (up to 60%) is observed for the {112} surface, followed by the {110} surface (up to 30%), whereas the thermal conductance for the {111} and {100} surfaces are more or less isotropic (the ratio stays ~ 1). This holds for most of the temperature range examined, even down to 100 K. Below 100 K, the ratio approaches unity in all cases, because at this temperature the main contribution to thermal conductance comes from the acoustic branches at low
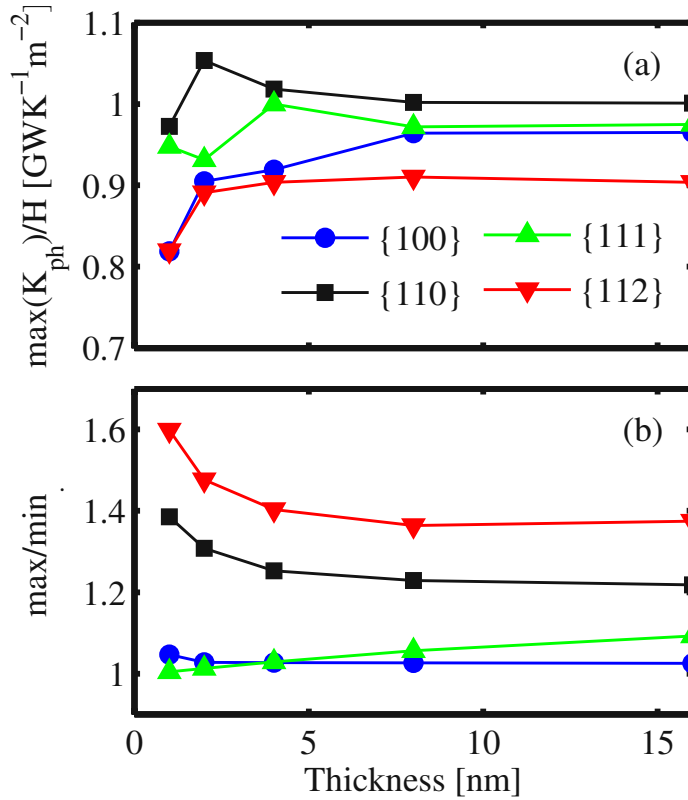
Figure 4.14: (a) The maximum value of the conductance in silicon thin-layers of different surface orientations at $T = 300$ K normalized by the thickness, versus layer thickness. (b) The ratio of the maximum to the minimum thermal conductance for different surface orientations, versus layer thickness at $T = 300$ K. For each surface orientation the transport orientations with the maximum and minimum conductance values are chosen.

energy, which are more isotropic. This is clearly observed in the low energy range of the transmissions in Fig. 4.8, in which the thermal conductivity is isotropic.

4.2.3 Remarks

Finally, it is worth mentioning that this chapter focused on the influence of bandstructure on the anisotropic behavior of the thermal transport properties of ultra-thin silicon layers and ultra narrow silicon nanowires. The accurate phonon bandstructures is employed, but a rather simplified ballistic transport formalism is utilized, which ignores the effects of phonon scattering. The intent, here, is to provide a qualitative indication of the anisotropic behavior of phonon transport in thin layers. Employing atomistic phonon bandstructures and a fully diffusive transport formalism that ac-
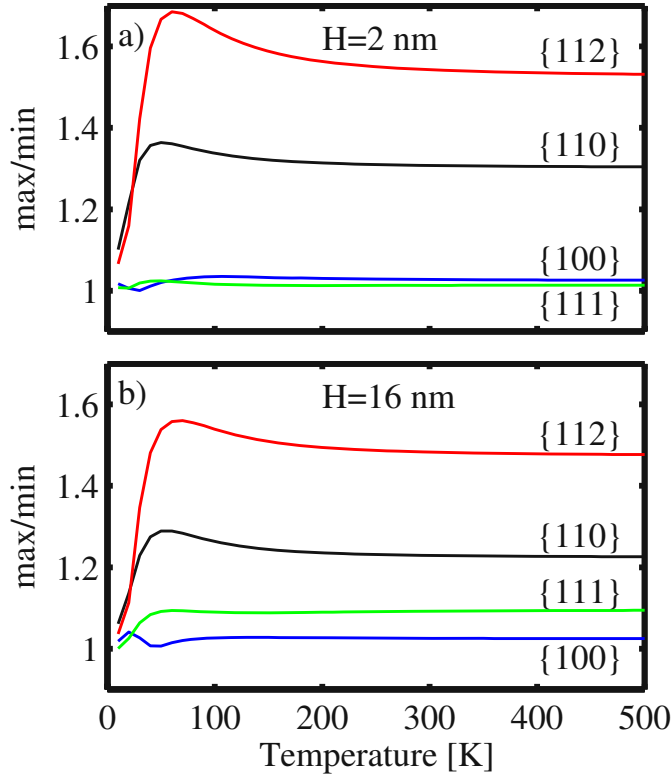
Figure 4.15: The ratio of maximum to minimum thermal conductance of thin-layers for different surfaces versus temperature. For each surface the transport orientation with the maximum and minimum conductance values are chosen. Thicknesses are (a) $H = 2$ nm and (b) $H = 16$ nm.

counts for the energy, momentum, and bandstructure dependence of each scattering event will be the topic of the subsequent chapter.

Our results, however, point out that a factor of two in phonon transport can be achieved once the channel geometry is optimized. These results agree qualitatively well with diffusive phonon transport calculations that indicate the superiority of the thermal conductivity of the {110}/<110> channel over other geometries, and the low thermal conductance for the {111}/<110> and {112}/<111> channel [112]. They also agree with calculations for silicon nanowires, which indicate the beneficial <110> transport orientation to heat transport, compared to other orientations [107, 111, 113]. When it comes to comparing to experimental results, however, unfortunately we could not identify any works in the literature that perform systematic thermal conductivity measurements in such ultra-thin layers ($H < 16$ nm) and in various confinement and transport orientations. Most experimental works on thermal conductivity consider relatively thick layers of thicknesses in the range of several 10 to several 100 of nanometers and primarily on {100} layers. In thicker layers the phonon modes are

almost bulk-like and one cannot observe the anisotropic phonon confinement effects that lead to bandstructure modifications and conductance variations. In addition, the influence of various scattering mechanisms make the thermal conductivity of thicker layers more isotropic, and hide the results of bandstructure anisotropy (that ballistic simulations fully capture).

Our findings, however, are useful in understanding phonon transport in ultra-thin silicon layers, and with regards to applications, could provide guidance in either maximizing thermal conductivity as in the case of thermal management, or minimizing it as in the case of thermoelectrics. For example, for electronic applications, we mention that for p-type nanoelectronic channels, transport in the $\{110\}/<110>$ orientation is beneficial compared to other orientations [114, 115]. This is also the case for the power factor of thermoelectric devices [116]. In the former case, however, for electronic devices large thermal conductivity is necessary in order to remove the heat from the device, otherwise the mobility is degraded. The large thermal conductivity of the $\{110\}/<110>$ channel, therefore, could be advantageous for p-type electronic devices. In the latter case, for thermoelectric devices channels with low thermal conductivity are needed in order to reduce losses and increase thermoelectric efficiency. The large thermal conductivity of the $\{110\}/<110>$ channel, therefore, could counteract the benefit of its larger power factor, and this channel might not be the optimal for thermoelectric p-type silicon devices.

5 Anomalous Diameter Dependence of Thermal Conductivity in Ultra-Thin Silicon Nanowires

In this chapter, we present atomistic valence force field calculations of thermal conductivity in silicon nanowires of diameters from 12 nm down to 1 nm at room temperature. We show that as the diameter is reduced, the phonon density-of-states and transmission function acquire a finite value at low frequency, in contrast to approaching zero as in the bulk material. It turns out that this effect results in what Ziman described as the "*problem of long longitudinal waves*" [61], which states that the thermal conductivity of a material increases as its length is increased due to the vanishing scattering for long-wavelength phonons. We show that this effect also appears in nanowires as their diameter is decreased below $D = 5$ nm. These features persist even in the presence of phonon-boundary scattering. Due to this increase in the contribution of long wavelength phonons, we show that the boundary becomes "effectively" more specular, and strikingly, the thermal conductivity increases with diameter decrease.

5.1 Phonon Transmission Function

Figure. 5.1 depicts the transmission function per unit area as a function of frequency for <100> nanowires of diameters $D = 12$ nm, 2 nm, and 1 nm. The inset of Fig. 5.1 shows the density of states per unit volume of these nanowires versus frequency. Note that we use the <100> transport orientation throughout this chapter. The basic features we describe, however, are valid for different orientations as well. The transmission of the 12 nm nanowire as well as the DOS follow the ω^2 relation of bulk at low frequencies. For thinner diameters, however, the transmission and DOS are constant at low frequencies, and increase as the diameter is reduced. The fact that there is a constant transmission at $\omega = 0$ for the acoustic branches leads to a strong manifestation of the "long-wavelength problem" in the thermal conductivity as we will see below.
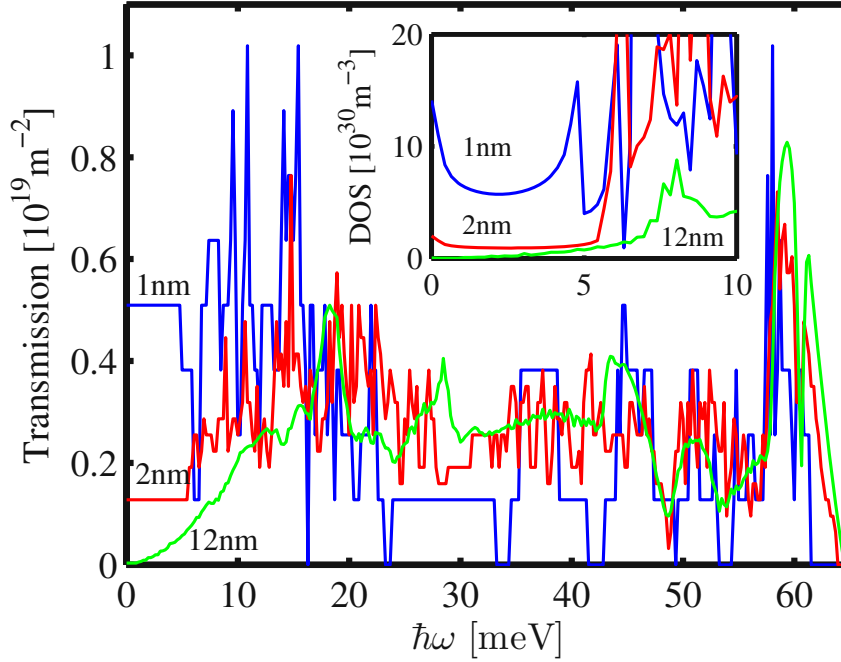
Figure 5.1: The normalized transmission function for silicon nanowires of diameters $D = 1$ nm (blue), 2 nm (red) and 12 nm (green). Inset: The density of phonon states per unit volume for the same diameters.

5.2 The Long-Wavelength Problem

In bulk semiconductors and insulators the thermal resistance arises from phonon-phonon scattering due of the anharmonicity of the inter-atomic potential. At room temperature, phonon-phonon scattering processes are strong and dominate the behavior of the thermal conductivity (κ_{ph}). A large part of the heat in semiconductors is carried by long wavelength longitudinal phonons, which have extremely long mean-free-paths (MFP) for scattering as well. In fact, it was pointed out that the MFP of the long wavelength longitudinal phonons diverges as their frequency tends to zero, resulting in the thermal conductivity to be a function of the size of the bulk solid, and diverging as the size of the solid increases [61, 117]. The most commonly employed single-mode-relaxation-time (SMRT) approximation for the solution the Boltzmann transport equation (BTE) for phonons [60, 62], uses an ω^2-dependent phonon-phonon (Umklapp) scattering rate [118, 119]. This model, in combination with the 3D bulk density-of-states, which is proportional to ω^2 at low frequencies, removes this ambiguity, and successfully explains the thermal conductivity of various semiconductors over a wide range of temperatures (also after appropriately including other common scattering mechanisms, such as defect scattering and grain-boundary scattering).

The thermal conductivity of 1D channels such as carbon nanotubes (CNTs), nanoribbons, and silicon nanowires has also been addressed in several recent studies [72, 98, 111, 120–124], since such channels are attractive for heat management and thermoelectric applications [20, 59]. The divergence of κ_{ph} with the size of the solid, or the "problem of long longitudinal waves" as referred to by Ziman [61], is stronger in this case, since the density-of-states in 1D structures is no longer ω^2-dependent, but has a finite value even at $\omega = 0$ [125], which increases the importance of low wavevector phonons. Indeed, several theoretical and experimental works have pointed out that thermal conductivity in 1D systems deviates from Fourier's law, or even increases with increasing channel length, either linearly, logarithmically, or following some power law [72, 120, 121, 126–128]. By including additional scattering mechanisms to the 3-phonon Umklapp mechanism usually employed, such as 3-phonon processes of second order [120], highly anharmonic potentials [129, 130], employing the exact solution of the Boltzmann equation [126], or molecular dynamics (MD) [122], the divergence is reduced, but it is still persistent, especially at low temperatures.

Here, we revisit this problem for ultra-thin silicon nanowires of diameters below 12 nm using the atomistic MVFF method for the calculation of the phonon modes and the BTE for phonon transport. We show that the issue of long-wavelength phonons turns out to be much more significant in 1D systems compared to the bulk material: This holds not only for low temperatures, but also at room temperature, and not only as the length of the channel is increased, but also as the diameter is reduced.

5.2.1 Scattering Rates

In this work, the thermal conductivity in the silicon nanowires is calculated using the phonon lifetime approximation in the phononic Boltzmann transport equation (Eq. 2.72). For the calculation of the relaxation times, we adopt the bulk formalism for Umklapp scattering [57, 118, 119]:

$$\frac{1}{\tau_U} = B\omega_\alpha q^2 T \exp\left(-\frac{C}{T}\right) \tag{5.1}$$

where $B = 2.8 \times 10^{-19}$ s/K and $C = 140$ K [57]. For boundary scattering we use:

$$\frac{1}{\tau_{B,\alpha}(q)} = \frac{1 - p(q)}{1 + p(q)} \frac{v_{g,\alpha}(q)}{D} \tag{5.2}$$

where D is nanowire diameter and $p(q)$ is q-dependent specularity parameter given by [60, 61, 112]:

$$p(q) = \exp\left(-4q^2\Delta_{rms}^2\right) \tag{5.3}$$

where we used $\Delta_{rms} = 0.3$ nm for the root-mean-square of the roughness amplitude. The specularity parameter p taking values from 0 to 1, is determined by the details

of the surface and surface roughness. For a smooth surface $p = 1$, and the phonon-boundary scattering is fully specular. For a very rough surface $p = 0$, which results in fully diffusive boundary scattering. Recently, studies showed that experimental results for boundary scattering in nanowires of diameters ~ 50 nm are only explained if an almost fully diffusive boundary is assumed [131, 132]. The overall relaxation rate including all scattering mechanisms is computed using Matthiessen's rule.

When considering the classical description of the energy distribution of phonons, in the Debye approximation, the heat conductivity of acoustic modes is given by [61, 121]:

$$\kappa_{\mathrm{ph}} = \frac{k_{\mathrm{B}}}{3\Omega} \int_{\omega_{\mathrm{min}}}^{\omega_{\mathrm{D}}} v_s^2 \tau(\omega) DOS(\omega) d\omega \tag{5.4}$$

where v_s is the corresponding sound velocity, $\omega_{\mathrm{min}} = 2\pi v_s/L$ is the minimum allowed phonon frequency which is determined by the longest allowed wavelength at a given channel length, and ω_{D} is the Debye frequency. As the bulk density-of-states $DOS(\omega)$ is proportional to ω^2, the Umklapp-limited thermal conductivity in 3D (with $\tau_U \sim 1/\omega^2$ as shown in Eq. 5.1) is bounded, even when the contribution of the long MFP phonons (as $\omega \to$) is included:

$$\kappa_{\mathrm{ph}} \sim \int_{2\pi v_s/L}^{\omega_{\mathrm{D}}} v_s^2 d\omega \sim \omega_{\mathrm{D}} - 2\pi v_s/L \tag{5.5}$$

since the second term of Eq. 5.5 goes to zero as the length increases.

In the case of 1D structures, on the other hand, the DOS is finite for low frequencies $DOS(\omega) = L/\pi v_s$ [53], which does not allow the cancellation of the $\tau_U \sim 1/\omega^2$ term. Therefore, the Umklapp-limited thermal conductivity of a 1D system is given by:

$$\kappa_{\mathrm{ph}} \propto \int_{2\pi v_s/L}^{\omega_{\mathrm{D}}} \frac{1}{\omega^2} d\omega \sim L \tag{5.6}$$

indicating a linear divergence with the channel length. Physically, this means that the lowest wavevector that contributes to thermal conductivity is determined by the length of the channel. For an infinite channel, longer and longer wavevectors of finite DOS are involved, which causes divergence in the thermal conductivity, in contrast to bulk. Several works in the literature attempt to add corrections that would bound κ_{ph} as the channel length increases [120, 126], although large κ_{ph} could still be possible in 1D. Some authors still use the bulk dispersion even for ultra-narrow channels [112, 133, 134], others include a constant specularity parameter for surface roughness, that adds a constant term in the total scattering rate, and removes the singularity for $\omega \to 0$ [101, 123, 135, 136]. A different approach was proposed recently by Mingo et al., where an additional rate of a second order 3-phonon scattering mechanism without ω-dependence was introduced for thermal transport in carbon nanotubes as [120]:

$$\frac{1}{\tau_{U2}} = A_0 T^2 \tag{5.7}$$
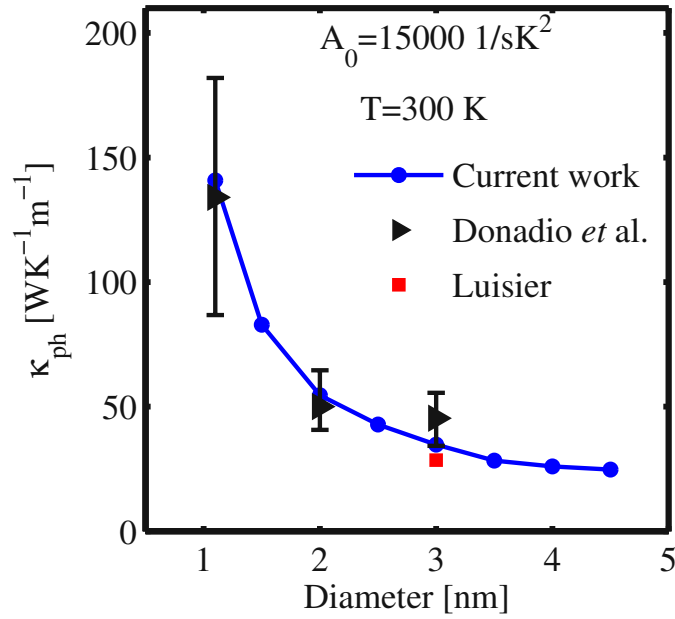
Figure 5.2: Room temperature phonon-phonon limited thermal conductivity for silicon nanowires versus diameter. Blue-dots: This work. Black-triangle: Molecular dynamics results by Donadio et al. [122]. Red-square: Calculations by Luisier [137].

Here A_0 is a frequency independent constant. This is just an order of magnitude approximation which removes the singularity for low frequency phonons, although very high thermal conductivities are still achieved. A study of the exact solution of the phonon BTE in carbon nanotubes showed a saturation in κ_{ph} as the length increased to the millimeter range [126], which could prove the suitability of using Eq. 5.7.

5.3 The Effect of Phonon-Phonon Scattering

The importance of the long wavevector phonons, however, is not only pronounced by the length of the channel. The reduction in the diameter of the nanowire can result in the same effect. An important point in Fig. 5.1 is that nanowires have a finite phonon DOS at low frequencies that also increases as the diameter is reduced, in contrast to bulk. Using the additional scattering mechanism proposed by Mingo et al., and adjusting the parameter A_0, we calibrated our phonon-phonon thermal conductivity calculations for silicon nanowires against the MD simulation results of Donadio et al. [122] and the results of Luisier [137] for nanowire diameters up to $D = 5$ nm
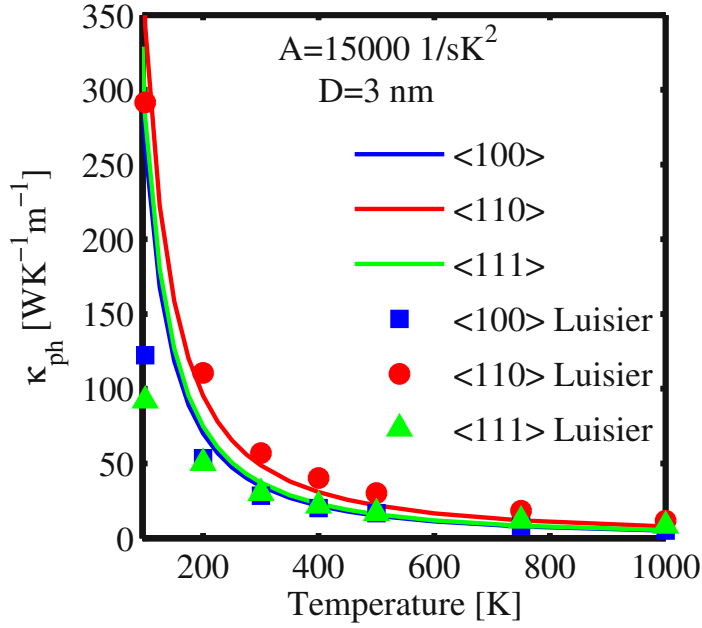
Figure 5.3: Thermal conductivity of the $D = 3$ nm nanowires versus temperature. Symbols are NEGF results from Ref. [137].

as shown in Fig. 5.2. These calculations were performed assuming $T = 300$ K and nanowires in the $<100>$ transport direction. The parameter A_0 of the 3-phonon second order processes was set to $A_0 = 15000/\text{sK}^2$, which provides a good agreement between our results and these two other studies for the entire diameter range considered. Our results also show good agreement with results from NEGF simulations [137] in a large temperature range (especially above $T = 200$ K), as shown in Fig. 5.3.

A clear increase in the thermal conductivity by $\sim 5X$ is observed as the diameter is decreased. This increase can be directly attributed to the increasing contribution of the low-frequency longitudinal modes as the diameter is reduced, since the transmission and DOS acquire a finite value (Fig. 5.1). Indications about thermal conductivity improvements due to phonon confinement can be found in other works as well, for silicon nanowires and other materials [72, 98, 122, 133, 138]. This is the first time, however, that this increase is attributed to the finite value that the phonon DOS acquires for the long-wavelength phonons.

The importance of the longitudinal modes is indicated in the colormap of Fig. 5.4 which shows the contribution of each phonon state to the thermal conductivity of the $D = 2$ nm nanowire. The dark-red color of the longitudinal acoustic (LA) mode indicates that most of the heat is carried by this low frequency, low wavevector mode. A large contribution is also attributed to the transverse acoustic (TA) and flexural
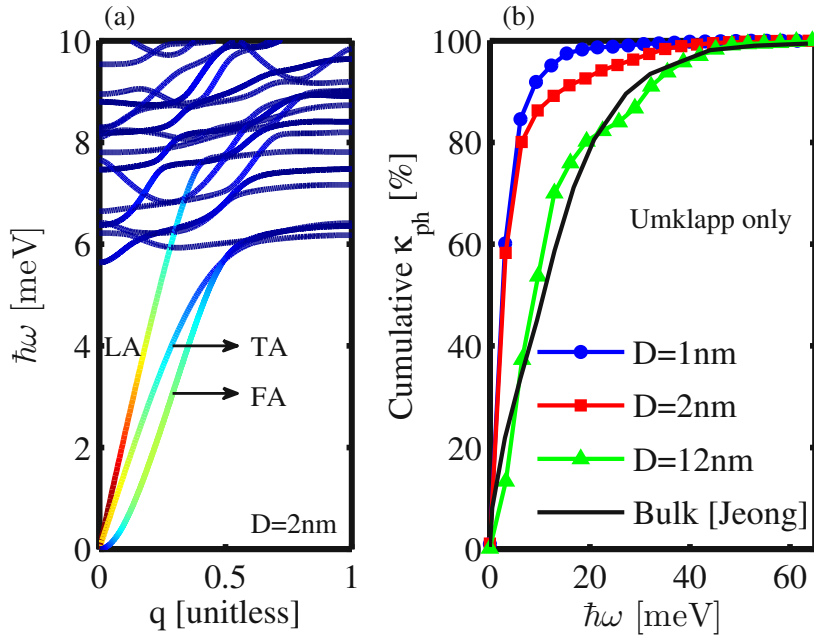
Figure 5.4: (a) The phonon dispersion of the $D = 2$ nm <100> nanowire. The colormap shows the contribution of various phonon states to the phonon-phonon-limited thermal conductivity (red indicates the highest, and blue the lowest thermal conductivity). (b) The cumulative thermal conductivity versus energy for nanowires of $D = 1$ nm (blue-dots), 2 nm (red-square), and 12 nm (green-triangle). The black-solid line shows the cumulative thermal conductivity of bulk silicon from Jeong et al. [57].

acoustic (FA) modes. The higher energy quasi-optical and optical modes carry only little heat due to their low phonon group velocities. To quantify the increasing importance of the low frequency modes with decreasing diameter, Fig. 5.4-b shows the cumulative phonon-phonon limited thermal conductivity versus energy at room temperature. Even in bulk silicon, the low frequency modes carry most of the heat as indicated by the black line from the work of Jeong et al. [57]. Almost half of the heat is carried by phonons of energies below 10 meV. nanowires with larger diameters, e.g. $D = 12$ nm, exhibit similar behavior, as shown by the green line marked by triangles. For thinner diameter nanowires, lower energy phonons become even more important. For $D = 2$ nm and $D = 1$ nm, $\sim 80\%$ of the heat is carried by phonons with energies below 5 meV.

5.4 The Effect of Phonon-Boundary Scattering

We now examine the significance of phonon-boundary scattering at long wavelength, which is the scattering mechanism that dominates thermal transport. Strong phonon-boundary scattering is indeed the reason for increased thermoelectric performance of nanostructures and silicon nanowires in particular [20]. Boundary scattering reduces the phonon MFP and thus the thermal conductivity. The boundary scattering-limited MFP can be obtained from Eq. 5.2 as:

$$\lambda(q) = D \left(\frac{1 + p(q)}{1 - p(q)} \right) \tag{5.8}$$

The MFP inevitably scales with the diameter D, but also by the boundary specularity parameter $p(q)$. In nanowires, the diameter strongly reduces the MFP. As we explain below, however, for ultra-narrow nanowire the term in the brackets increases. This increase relaxes the monotonic decrease of the MFP due to diameter reduction, and weakens phonon-boundary scattering.

The term in the bracket of Eq. 5.8 is large for long wavelength phonons because the specularity parameter $p(q)$ peaks at $q = 0$ as shown in the inset of Fig. 5.5. Long wavelength phonons have $p(0) = 1$, which means that they undergo specular boundary scattering. In other words, waves of lengths larger than the average roughness features are not affected by the roughness and are more specularly reflected. Phonons of smaller wavelengths (larger q) scatter more diffusively, as the roughness feature sizes are of the order of their wavelengths [139]. As we observed in Fig. 5.4, however, the heat transport in thinner nanowires is shifted towards the low-wavevector phonon states as the diameter is reduced. These states, however, are affected very weakly by boundary scattering due to their large $p(q)$, which makes the boundary overall more specular (although the thermal conductivity is still severely degraded due to the reduction in diameter).

Figure 5.5 illustrates the importance of this wavevector-dependence of the specularity parameter $p(q)$ on the cumulative thermal conductivity for the $D = 2$ nm nanowire. The phonon-phonon scattering-limited result of Fig. 5.4 which corresponds to the fully specular case ($p = 1$), is also shown by the red line for reference. For fully diffusive boundaries ($p = 0$ for all frequencies), the thermal conductivity is almost equally distributed over the phonon energy (Fig. 5.5, green line). Note that here we use $\Delta_{rms} = 0.3$ nm. A similar result is observed once a constant specularity parameter is used, i.e. $p = 0.8$ (Fig. 5.5, black line), as it is assumed in several studies [123,136,140]. Interestingly, the distribution of the thermal conductivity over phonon energy for the fully diffusive ($p = 0$), and the almost specular ($p = 0.8$) boundary conditions is very similar. On the other hand, the cumulative thermal conductivity trend is different when the q-dependent p is taken into account (blue line) and looks very much like the phonon-phonon scattering-limited case. The importance of the low frequency modes becomes even stronger (sharper rise of the cumulative conductivity at low frequencies
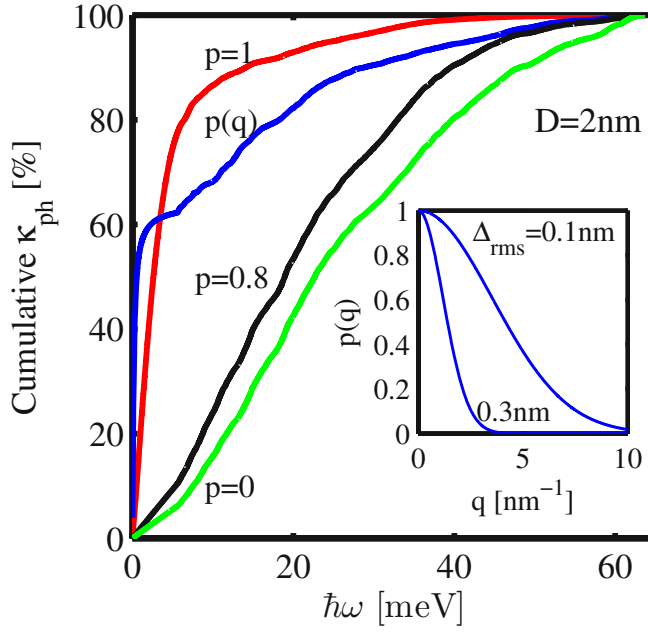
Figure 5.5: The cumulative thermal conductivity versus energy for a nanowire with $D = 2$ nm versus energy, for different treatments of the phonon-boundary scattering specularity parameter p: Phonon-phonon scattering-limited, $p = 1$, (red line); constant specularity parameter $p = 0.8$ (black line), and $p = 0$ (green line) for fully diffusive boundary scattering; wavevector-dependent p, (blue line). Inset: The specularity parameter versus wavevector for roughness amplitudes $\Delta_{rms} = 0.1$ nm and 0.3 nm.

compared to the phonon-phonon scattering case), in which case almost 60% of the total thermal conductivity is carried by phonons of energies below 2 meV. Above energies of 2 meV, where the boundaries become totally diffusive for all frequencies (see inset of Fig. 5.5), the thermal conductivity is distributed almost equally over the remaining phonon energies. We note that the phonon energy above which the thermal conductivity becomes fully diffusive (e.g. $p(q)$ becomes zero) is determined by the roughness amplitude. For smaller amplitudes, e.g. $\Delta_{rms} = 0.1$ nm as shown in the inset of Fig. 5.5, $p(q)$ indicates a stronger specular scattering behavior in a larger part of the phonon energy spectrum.

Therefore, for ultra-thin nanowires, it is not appropriate to use a constant specularity parameter for phonons of all wavevectors as is often assumed for thicker nanowires [123, 141]. The underlying wavevector contributions to the thermal conductivity cannot be captured accurately, although one could adjust the specularity parameter to fit experimental measurements. This is illustrated in Fig. 5.6, which shows the thermal conductivity of the $D = 2$ nm nanowire versus constant values
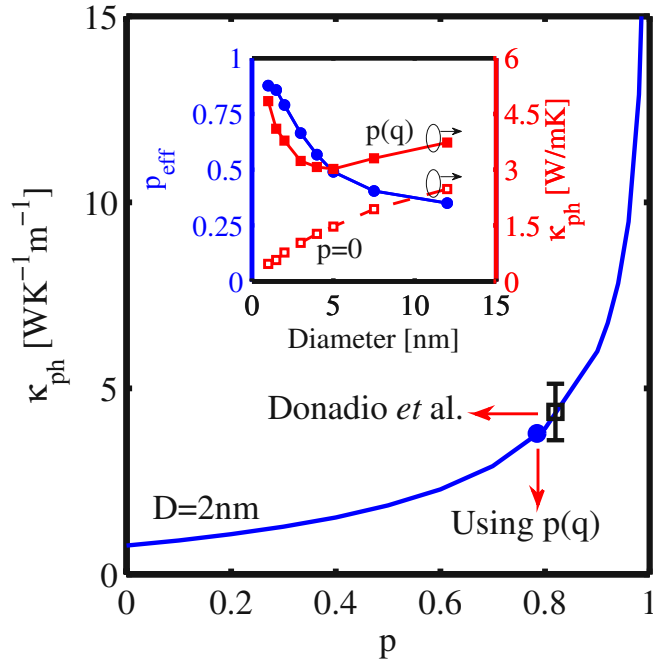
Figure 5.6: Thermal conductivity of the $D = 2$ nm nanowire versus the boundary's specularity parameter that is assumed to be constant for all wavevectors. The blue-dot indicates on the y-axis the thermal conductivity calculated using the wavevector-dependent specularity parameter $p(q)$. On the x-axis, it indicates a constant "effective" specularity parameter for this surface. The black-square symbol indicates on the y-axis the thermal conductivity for this nanowire obtained using MD simulations by Donadio et al. [122]. Inset: The left axis shows the "effective" specularity parameter as a function of the nanowire's diameter (solid-dot blue line). The right axis shows the thermal conductivity considering phonon-phonon and phonon-boundary scattering for the cases of $p = 0$ (dashed-square red line), and $p = p(q)$ (solid-square red line).

of the specularity parameter (the same p for all wavevectors). The thermal conductivity remains low (below 5 W/mK) for a large range of p, even up to $p = 0.8$, and is smaller than the Umklapp scattering-limited conductivity by more than an order of magnitude. The blue dot indicates the thermal conductivity of the same nanowire, with the same roughness amplitude, using the wavevector dependent $p(q)$ as described by Eq. 5.3. In this case, $\kappa_{ph} \sim 4$ W/mK, which is also in good agreement with the result of MD simulations by Donadio et al. (black-square point) for the same nanowire [122]. In order for the two approaches (constant p versus $p(q)$) to provide the same value for the thermal conductivity, a constant specularity parameter of $p \sim 0.8$ needs to be used. The large "effective" specularity parameter indeed illustrates that

the phonon-boundary scattering is almost specular. This is a consequence of the increasing importance of the large wavelength phonons that scatter almost specularly on the nanowire boundary as the diameter is reduced. Indeed, if one extracts an "effective" constant specularity parameter, that provides the same value for the thermal conductivity as the wavevector-dependent $p(q)$, then this number will increase as the diameter is decreased. This is shown in the inset of Fig. 5.6 (left axis). The "effective" specularity parameter saturates around $p \sim 0.3$ for larger nanowire diameters, which is close to the value usually assumed for larger nanowires. As the diameter is reduced to $D = 1$ nm, however, it increases even up to $p \sim 0.9$, a consequence of the dominant role of the long wavelength phonons.

Figure 5.6, therefore, demonstrates the counter-intuitive result that for the same roughness, boundary scattering is overall more specular for ultra-thin nanowires than for thicker ones. The phonon-boundary scattering, however, is still dominant and causes thermal conductivity reduction from $\kappa_{ph} \sim 50$ W/mK (phonon-phonon only as shown in Fig. 5.2), to $\kappa_{ph} \sim 5$ W/mK. The degradation, though, originates from the influence of the diameter reduction on the MFP (see Eq. 5.8), and not from the diffusive nature of the boundary. Interestingly, however, for diameters below 5 nm, the term in the bracket of Eq. 5.8 increases faster than the reduction in D. The MFP then starts to increase, the effect of phonon-boundary scattering is reduced, and the thermal conductivity increases. This is indicated in the inset of Fig. 5.6 (right axis), which shows that as the effective specularity increases with decreasing diameter, the same happens to the thermal conductivity as well (solid-square red line). In contrast, a fully diffusive boundary with $p = 0$ as one would assume for such thin nanowire, results to a monotonic decrease in the conductivity as the diameter is reduced (dashed-square red line).

6 Thermoelectric Figure of Merit of Ultra-Narrow Silicon Nanowires

Thermoelectric materials based on nanostructured and low-dimensional silicon have attracted a significant attention after recent experiments indicated that they can provide a large ZT figure of merit [17, 20, 142]. Although bulk silicon has $ZT_{\text{bulk}} \sim 0.01$, the ZT of silicon nanowires with side lengths scaled down to ~ 50 nm was experimentally demonstrated to be $ZT_{\text{NW}} \sim 0.5$ [17, 20]. A similar observation was made in silicon nanomeshes of features sizes ~ 55 nm [142]. This remarkable improvement in the ZT was a result of a significant suppression in the thermal conductivity κ_{ph}, whereas the electronic power factor was not changed significantly compared to the bulk material. The measurements to date were performed in nanowires or nanomeshes of feature sizes of several 10s of nanometers [17, 20, 142]. Whether this trend continues, or even improves, when the nanowire diameters are reduced in the sub-ten nanometer regime still needs to be shown. The initial theoretical studies proposed that the performance can be improved once the channels are truly one-dimensional, or if the channel bandstructure is properly optimized [9, 143]. On the other hand, at the sub-ten nanometer scale, the electronic mobility is severely degraded due to enhanced electron-phonon interaction and stronger surface roughness scattering (SRS) [143]. It still needs to be shown if this reduction would offset the performance improvement achieved through the reduction of thermal conductivity.

In this chapter, we compute the room temperature thermoelectric figure of merit ZT in ultra-narrow silicon nanowires using atomistic simulations. The role of transport orientations and diameter on the thermoelectric power factor of nanowires using atomistic bandstructure simulations has been recently studied [143]. Using the thermoelectric power factor of Ref. [143] (Figs. 3c and 7c of Ref. [143]) and the calculated thermal conductivity, as in Chapter 5, we estimate the ZT figure of merit for n-type and p-type cylindrical nanowires of various transport orientations.

6.1 Thermal Conductivity

The thermal conductivity of silicon nanowires versus diameter is shown in Fig. 6.1 for nanowires in the <100> (blue lines), <110> (red lines), and <111> (green lines)
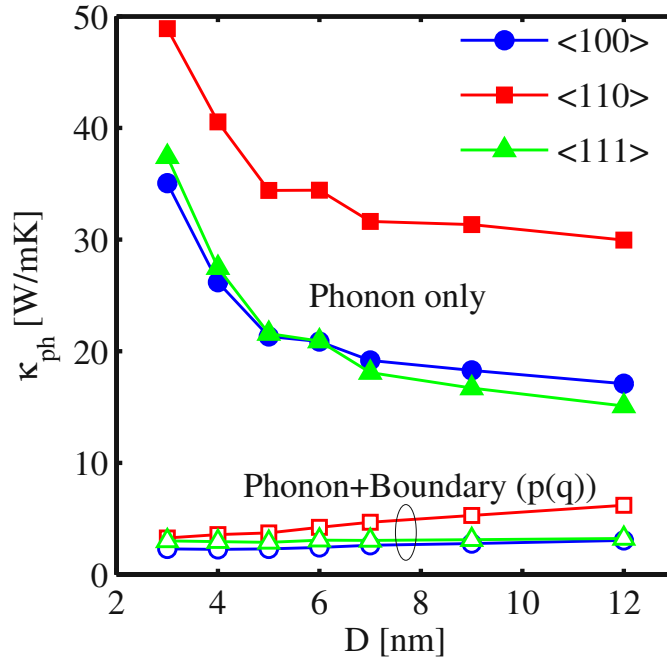
Figure 6.1: The thermal conductivity for silicon nanowires versus diameter at $T = 300$ K. Results for nanowires in the $<100>$ (blue-circle), $<110>$ (red-square), and $<111>$ (green-triangle) orientations are shown. Solid symbols: Results when only phonon-phonon scattering is included. Empty symbols: Results when phonon-phonon and phonon-boundary scattering are included.

transport orientations. With solid symbols we show the phonon-phonon scattering-limited thermal conductivity, whereas with empty symbols the thermal conductivity additionally includes phonon-boundary scattering. Several interesting observations can be made here. First, there is a significant anisotropy in the thermal conductivity, with the $<110>$ nanowires having the highest conductivities in the entire diameter range, also in agreement with other theoretical studies [111]. Second, the phonon-phonon scattering-limited thermal conductivity (solid symbols) is reduced by a factor of $\sim 5X$ from to the bulk value which is 140 W/mK. This indicates the strong influence of phonon confinement. Third, phonon-boundary scattering has a quite strong influence, reducing the thermal conductivity by another factor of $\sim 5X$, limiting the thermal conductivity to values below 10 W/mK in the entire diameter range, irrespective of transport orientation.

This strong reduction of the thermal conductivity is the main reason for the improved thermoelectric performance in nanostructures. Phonon-boundary scattering is the main reason for that reduction, although phonon confinement also contributes to κ_{ph} reduction. For nanowires with ultra-narrow diameters, however, the electrical conduc-

Figure 6.2: The ZT figure of merit for (a) n-type and (b) p-type silicon nanowires versus diameter at $T = 300$ K. Results for nanowires in the $<100>$ (blue-circle), $<110>$ (red-square), and $<111>$ (green-triangle) orientations are shown. In the calculation of the power factor and the thermal conductivity, only electron-phonon scattering and phonon-phonon scattering are respectively considered.

tivity is also strongly degraded by SRS, and it is yet not clear if rough boundaries can still provide a benefit to the ZT. Below, we provide answers to this issue.

6.2 Thermoelectric Figure of Merit

To illustrate how the different scattering mechanisms affect ZT, in Fig. 6.2 we show ZT when only electron-phonon scattering is considered for the electronic system and only phonon-phonon scattering is considered for the phononic system. Results for n-type nanowires are shown in Fig. 6.2-a, and results for p-type nanowires in Fig.6.2-b. Further below, in Fig.6.3, we include the effect of boundary scattering for both systems. We consider nanowires of diameters from $D = 3$ nm to 12 nm in three different orientations, $<100>$ (blue lines), $<110>$ (red lines), and $<111>$ (green lines). We

assume a carrier concentration of 10^{19}cm^{-3}, which is close to the concentration where the maximum of the power factor is observed. ZT in Fig. 6.2 shows a considerable orientation and diameter dependence. For n-type nanowires, the ZT reaches values of ~ 0.15 in the best case (for the $<111>$ nanowires and diameters above 6 nm). In the worst case, ZT is significantly lower at only ~ 0.05, which is achieved for the lowest diameters, as well as for the $<110>$ nanowire in the entire diameter range. ZT for these particular nanowires suffers from their large thermal conductivities as shown in Fig. 6.1 ($\sim 50\%$ higher compared to the other orientations). P-type nanowires have lower ZT values, below 0.05 for most cases. A significant increase is observed in the cases of the $<111>$ and $<110>$ nanowires with decreasing diameter, which can be attributed to the improvement of their electrical conductivity [143] since the bandstructures of these nanowires undergo significant modifications with confinements and their hole effective mass is significantly reduced [144]. For both p-type, and n-type nanowires, the $<111>$ orientation provides the best performance. The reduction in the thermal conductivity due to phonon confinement, therefore, increases ZT by an order of magnitude compared to the bulk value ($ZT_{\text{bulk}} \approx 0.01$).

6.2.1 The Effects of Boundary Scattering

A profound increase in ZT can be achieved when we consider the more realist case, in which we allow for electrons and phonons to undergo boundary scattering in addition to phonon scattering. The ZT figure of merit in this case is shown in Fig. 6.3, (Fig.6.3-a for n-type nanowires and Fig. 6.3-b for p-type nanowires). The anisotropy, and the main features observed with diameter scaling are not altered significantly compared to Fig. 6.2. ZT, however, increases by almost a factor of 4X with the introduction of boundary scattering, both for n-type and p-type nanowires (the phonon-scattering only results of Fig. 6.2-a are shown in Fig. 6.3-a for reference). ZT varies from ~ 0.25 to ~ 0.75 for n-type nanowires ($ZT \sim 0.75$ at larger diameters), also in agreement with other theoretical studies [145]. For p-type nanowires it reaches a maximum of $ZT \sim 0.5$ for the $<111>$ nanowires of smaller diameters.

This increase in ZT indicates that the boundary scattering reduces the thermal conductivity by a factor of $\sim 4X$ more than it reduces the power factor. As explained in Ref. [143], the introduction of surface roughness (SR) scattering, degrades the electrical conductivity significantly, but improves the Seebeck coefficient slightly. The degradation in the power factor, therefore, is dominated by the decrease in the electrical conductivity. Fig. 6.3 shows, however, that even in geometries with ultra-small feature sizes, in which the electrical conductivity is strongly degraded due to enhanced electron-phonon and electron-SR scattering, the thermal conductivity even stronger degrads. It suggests that phonon engineering techniques that further increase phonon scattering can help in the improvement of ZT. This was considered to be the case for nanowires of larger diameters [20], but it appears to be the case also for nanowire diameters as thin as a few nanometers.
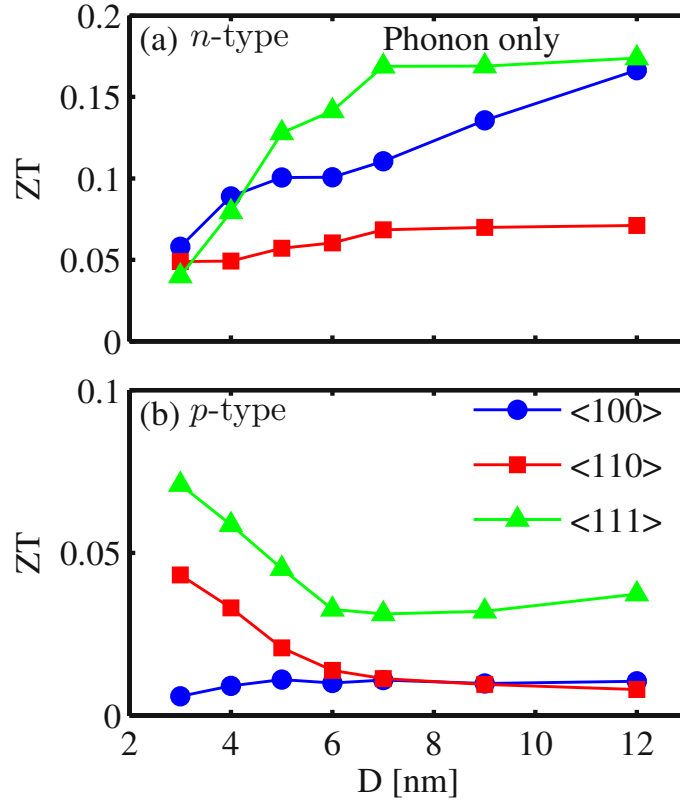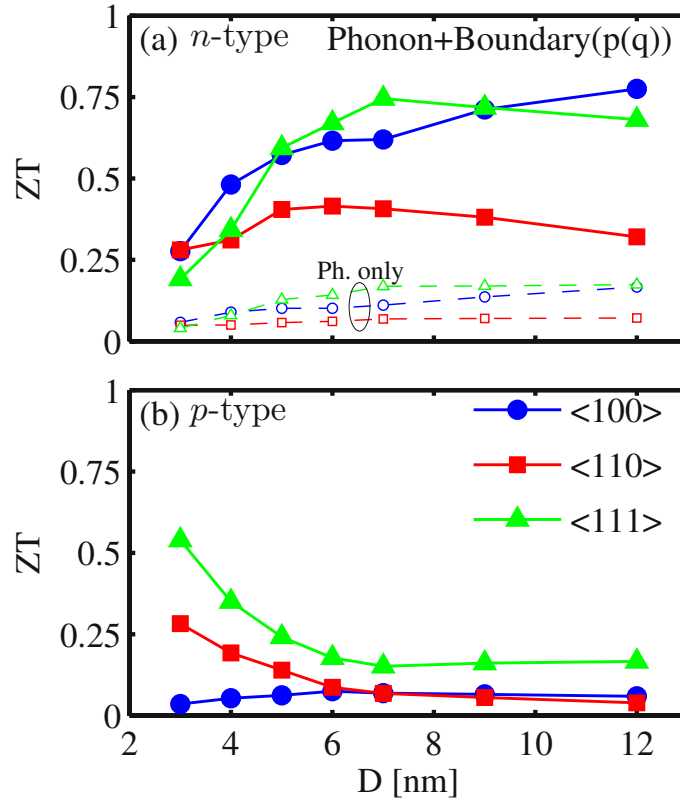
Figure 6.3: The ZT figure of merit for (a) n-type and (b) p-type silicon nanowires versus diameter at $T = 300$ K. Results for nanowires in the $<100>$ (blue-circle), $<110>$ (red-square), and $<111>$ (green- triangle) orientations are shown. In the calculation of the power factor electron-phonon plus electron-boundary scattering is considered. In the calculation of the thermal conductivity phonon-phonon and phonon-boundary scattering are considered. The dotted lines in (a) show for reference ZT when only electron-phonon and phonon-phonon scattering is considered as in Fig. 6.2-a.

6.2.2 Electron versus Phonon Transports in Rough Nanowires

The reason why boundary scattering degrades the thermal conductivity more than the electrical conductivity is that the electronic system is not affected significantly by boundary scattering for larger nanowire diameters, i.e. $D > 10$ nm. In the absence of a confining electric field (e.g. flat potential in the nanowires' cross section), electron scattering by surface roughness depends mainly on the shift of the band edges due to confinement, which is only important for diameters $D < 10$ nm. On the other hand, from Eq. 5.2, the phonon-boundary scattering rate is inversely proportional to the nanowire diameter as D^{-1}, a trend that is initiated at very large diameters.
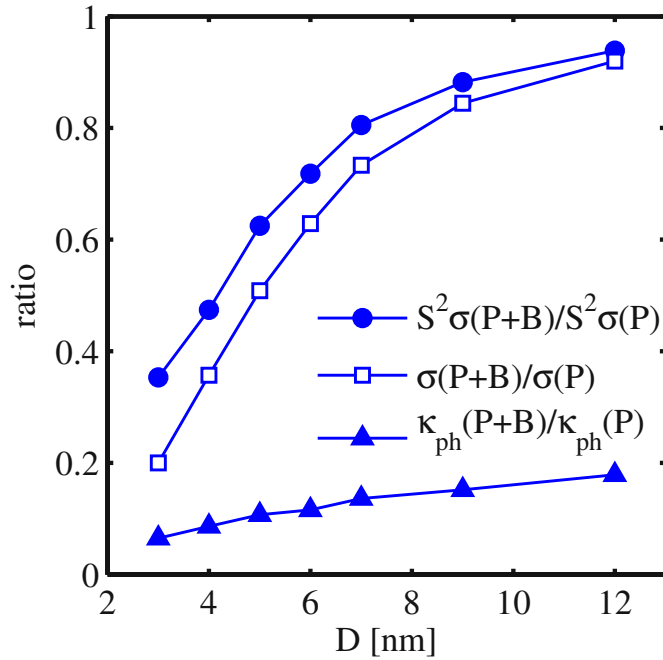
Figure 6.4: Filled circle symbols: The ratio of the power factor with electron-phonon and electron-boundary scattering ($\sigma S^2(P + B)$) included to the power factor with only electron-phonon scattering ($\sigma S^2(P)$) included. An n-type <100> silicon nanowires at room temperature is considered. Empty square symbols: The same ratio for the electrical conductivity. Filled triangle symbols: For the same nanowires, the ratio of the thermal conductivity with phonon-phonon plus phonon-boundary scattering ($\kappa_{ph}(P + B)$) included to the thermal conductivity with phonon-phonon only scattering ($\kappa_{ph}(P)$) included.

At $D = 10$ nm the thermal conductivity is already strongly reduced. Although the surface-roughness scattering-limited electron mobility degrades strongly with a power factor of D^{-6} for $D < 10$ nm [146], the overall reduction of the electrical conductivity is less than the κ_{ph} reduction even for diameters down to $D = 3$ nm.

This stronger reduction of the thermal conductivity due to boundary scattering compared to the reduction of the electrical conductivity due to boundary scattering, is illustrated in Fig. 6.4. Here we show the ratio of the thermal conductivity for the <100> nanowires including phonon-phonon and phonon-boundary scattering ($\kappa_{ph}(P + B)$), to the thermal conductivity including only phonon-phonon scattering ($\kappa_{ph}(P)$) (triangle symbols). We also show the same ratio for the electrical conductivity of the n-type nanowires, e.g. the ratio of the electrical conductivity including electron-phonon-plus-SRS, to the electrical conductivity including only electron-phonon scattering (empty-square symbols). The figure clearly demonstrates that although the degradation in

the electrical conductivity due to SRS becomes stronger as the diameter is reduced, still, the detrimental effect of boundary scattering is larger on the thermal conductivity. Even at the relatively large nanowire diameters ~ 12 nm, phonon-boundary scattering is very effective in reducing the thermal conductivity down to $\sim 20\%$ of its phonon-phonon scattering-limited value. Additionally, the power factor, benefits from an increase in the Seebeck coefficient by diameter reduction and surface-roughness-scattering by $\sim 70\%$ [147]. This improves the power factor, which partly compensates the reduction of the electrical conductivity as also shown in Fig. 6.4 (circle symbols).

6.2.3 Diffusive Thermoelectric Figure of Merit

This improvement in the power factor further proves the point that boundary scattering is more effective in reducing the thermal conductivity than reducing the power factor. As a result, phonon engineering techniques that cause additional reductions in the thermal conductivity could provide improvements of ZT, despite the consequent reduction in the electrical conductivity. For example, in the case of a fully diffusive boundary for phonons, either by special engineering of the roughness [21, 148, 149], by decorating the surfaces with various species [59, 150, 151], or by modulating the nanowire's diameter [124], the ZT performance could be increased. This is illustrated in Fig. 6.5, showing ZT for the same nanowires as before in Fig. 6.3, but now we assume a fully diffusive boundary for phonons, e.g. the specularity parameter is set to $p = 0$ for all wavevectors. In this case, ZT is increased to values close to $ZT \sim 1.3$ for both n-type and p-type nanowires (in the best cases). This is almost a factor of 2X improvement compared to the case we present in Fig.6.3 where we employ the q-dependent specularity parameter $p(q)$, rather than fully diffusive boundaries for all phonons.
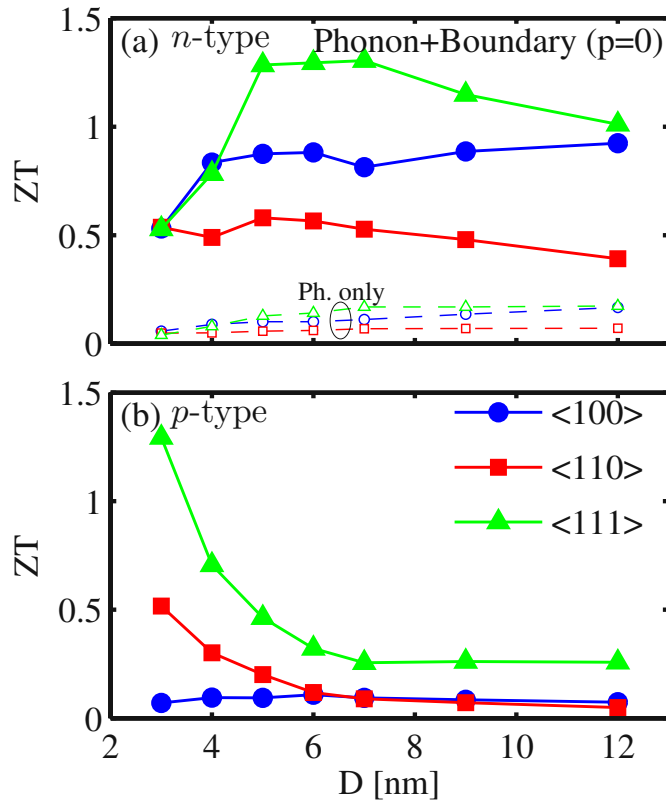
Figure 6.5: The ZT figure of merit for (a) n-type and (b) p-type silicon nanowires versus diameter at $T = 300$ K. Results for nanowires in the $<100>$ (blue-circle), $<110>$ (red-square), and $<111>$ (green-triangle) orientations are shown. In the calculation of the power factor electron-phonon plus electron-boundary scattering is considered. In the calculation of the thermal conductivity phonon-phonon and phonon-boundary scattering are considered, but in this case the boundary is assumed to be fully diffusive. The dotted lines in (a) show for reference the ZT when only electron-phonon and phonon-phonon scattering is considered as in Fig. 6.2-a.

7 Summary and Conclusions

In this thesis, we investigate the thermal and thermoelectric properties of silicon- and graphene-based nanostructures. We start from the investigation of the ballistic to diffusive crossover in the thermoelectric transport in armchair graphene nanoribbon (AGNR). Although in the case of AGNRs a bandgap is naturally present, the band-gap decreases with increasing the width, which results in a lower value of Seebeck coefficient for wider ribbons. As a result, the ballistic power factor only slightly increases with temperature and the ribbon's width. In contrast, by increasing the width the lattice thermal conductance strongly increases and so the ballistic ZT value decreases with increasing W. The introduction of edge roughness in order to reduce high thermal conductivity does not benefit ZT because the electrical conductance is severely degraded by the roughness. As a result, the ZT figure of merit decreases with increasing the channel length and its value is limited to values below 0.3.

We also analyze the ballistic thermoelectric properties of GALs. Our results indicate that the size of the antidots, the circumference of the antidots, and the distance between antidots can strongly influence the thermal properties of GALs. Results from ballistic calculations show that by appropriate selection of the geometrical parameters one can significantly reduce the thermal conductance of GALs and improve their thermoelectric figure of merit.

We present a theoretical design procedure for achieving high thermoelectric performance in zigzag graphene nanoribbon (ZGNRs) channels, which in their pristine form have very poor performance. We show that by introducing extended line defects in the length direction of the nanoribbon we can create an asymmetry in the density of modes around the Fermi level, which improves the Seebeck coefficient. ELDs increase the electronic conduction subbands, which increase the channel conductance as well. The power factor is therefore significantly increased. In addition, we show that by introducing edge roughness the phonon thermal conductivity is degraded effectively more than the electronic thermal conductivity, or the electronic conductance. These three effects result in large values of the thermoelectric figure of merit, and indicate that roughed ZGNRs with ELDs could potentially be used as efficient high performance thermoelectric materials.

Next, we investigate how dimensionality affects thermal and thermoelectric properties of low-dimensional silicon-based nanostructures. We study the effect of confinement on the phonon properties of ultra-narrow silicon nanowires of side sizes of 1 nm to 10 nm. We use the modified valence force field (MVFF) method to compute the phononic

dispersion and extract the density of states, the transmission function, the sound velocity, and the ballistic thermal conductance. We find that the phononic dispersion and the ballistic thermal conductance are functions of the geometrical features of the structures, i.e., the transport orientation and confinement length scale. The phonon group velocity and thermal conductance can vary by a factor of two depending on the geometrical features of the channel. The <110> nanowire has the highest phonon group velocity and thermal conductance, whereas the <111> has the lowest. The <111> channel is thus the most suitable orientation for thermoelectric devices based on silicon nanowires since it also has a large power factor.

Next, we investigate the effect of confinement and orientation on the phonon transport properties of ultra-thin silicon layers of thicknesses between 1 nm to 16 nm. We consider the major thin layer surface orientations {100}, {110}, {111}, and {112}. For every surface orientation, we study thermal conductance as a function of the transport direction within the corresponding surface plane. We find that the ballistic thermal conductance in the thin layers is anisotropic, with the {110}/<110> channels exhibiting the highest and the {112}/<111> channels the lowest thermal conductance with a ratio of about two. We find that in the case of the {110} and {112} surfaces, different transport orientations can result in $\sim 50\%$ anisotropy in thermal conductance. The thermal conductance of different transport orientations in the {100} and {111} layers, on the other hand, is mostly isotropic. These observations are invariant under different temperatures and layer thicknesses. We show that this behavior originates from the differences in the phonon group velocities, whereas the phonon density of states is very similar for all the thin layers examined. We also show how the phonon velocities can be understood from the phonon spectrum of each channel. These findings could be useful in the design of the thermal properties of ultra-thin silicon layers for thermoelectric and thermal management applications.

In this work we also study the thermal conductivity of ultra-thin silicon nanowires using the atomistic modified valence-force-field method for the computation of the phonon bandstructure and the Boltzmann equation for phonon transport. We show that the "problem of long-wavelength phonons" as described by Ziman and others, which causes divergence in the thermal conductivity of quasi-1D channels with increasing length, is also present in silicon nanowires. The divergence occurs not only as the length is increased, but also as the diameter is reduced. We attribute this to the fact that in ultra-narrow nanowires the density-of-states and the transmission function of long-wavelength phonons acquires a finite value, as compared to zero in the bulk materials, which increases their importance in carrying heat, and causes the thermal conductivity to increase as the diameter is reduced below 5 nm. We point out that this effect has two important consequences: The first is that a larger portion of heat is carried by low frequency phonons in ultra-narrow nanowires as compared to bulk, e.g. almost 80% of the heat is carried by phonons with energies below 5 meV. The second is that, counter-intuitively, at the same roughness conditions, the boundary scattering is more specular for the ultra-narrow nanowires, and becomes more diffusive as the

diameter is increased. This results in a striking anomalous increase in the thermal conductivity as the diameter is reduced below 5 nm.

Finally, the room temperature ZT figure of merit of ultra-narrow silicon nanowires of diameters $D < 12$ nm is calculated using atomistic simulations for both electrons and phonons. The ZT values at 300 K in the best case are slightly below unity (~ 0.75), in agreement with experimental measurements. We show that the largest contribution towards achieving this relatively high value is attributed to the significant reduction in the thermal conductivity due to boundary scattering. Phonon confinement also causes a reduction in thermal conductivity and ZT improvement, but its effect is weaker. For ultra-narrow nanowire diameters ($D \sim 3$ nm), the power factor is strongly reduced due to surface roughness scattering. We show, however, that the benefits from phonon-boundary scattering are still persistent in increasing ZT, since for the same roughness amplitudes, boundary scattering reduces the thermal conductivity significantly more than it reduces the power factor (by $\sim 4X$). Finally, we calculate that in the case of fully diffusive boundaries for phonons, the ZT values can increase above unity for both n-type and p-type nanowires.

Bibliography

[1] M. Zebarjadi, K. Esfarjani, M. S. Dresselhaus, Z. F. Ren, and G. Chen, "Perspectives on Thermoelectrics: From Fundamentals to Device Applications," *Energy Environ. Sci.*, vol. 5, pp. 5147–5162, 2012.

[2] T. Seebeck, "Magnetische Polarisation der Metalle und Erze durch Temperatur-Differenz," *Abhandlungen der Deutschen Akademie der Wissenschaften zu Berlin*, pp. 265–373, 1823.

[3] G. Nolas, J. Sharp, and H. Goldsmid, *Thermoelectrics: Basic Principles and New Materials Developments.* Germany: Springer, 2001.

[4] T. Harman, P. Taylor, M. Walsh, and B. LaForge, "Quantum Dot Superlattice Thermoelectric Materials and Devices," *Science*, vol. 297, no. 5590, pp. 2229–2232, 2002.

[5] H. Goldsmid, *Introduction to Thermoelectricity.* Springer, 2010.

[6] Z.-G. Chena, G. Hana, L. Yanga, L. Chenga, and J. Zou, "Nanostructured Thermoelectric Materials: Current Research and Future Challenge," *Progress in Natural Science: Materials International*, vol. 22, no. 6, pp. 535–549, 2012.

[7] C. Wood, "Materials for Thermoelectric Energy Conversion," *Reports on Progress in Physics*, vol. 51, no. 4, p. 459, 1988.

[8] G. Slack, *CRC Handbook of Thermoelectrics.* CRC Press, 1995.

[9] L. D. Hicks and M. S. Dresselhaus, "Thermoelectric Figure of Merit of a One-Dimensional Conductor," *Phys. Rev. B*, vol. 47, p. 16631, 1993.

[10] M. S. Dresselhaus, Y. M. Lin, S. B. Cronin, O. Rabin, M. R. Black, G. Dresselhaus, and T. Koga, "Quantum Wells and Quantum Wires for Potential Thermoelectric Applications," *Proc. Natl. Acad. Sci.*, vol. 41, p. 1, 2001.

[11] G. D. Mahan and J. O. Sofo, "The Best Thermoelectric," *Proc. Natl. Acad. Sci. USA*, vol. 93, p. 7436, 1996.

[12] K. Kim, Y. Zhao, H. Jang, S. Lee, J. Kim, K. Kim, J.-H. Ahn, P. Kim, J.-Y. Choi, and B. Hong, "Large-scale pattern growth of graphene films for stretchable transparent electrodes," *Nature*, vol. 457, pp. 706–710, 2009.

[13] D. A. Wright, "Thermoelectric Properties of Bismuth Telluride and Its Alloys," *Nature*, vol. 181, p. 834, 1954.

[14] W. Kim, S. L. Singer, A. Majumdar, D. Vashaee, Z. Bian, A. Shakouri, G. Zeng, J. E. Bowers, J. M. O. Zide, and A. C. Gossard, "Cross-Plane Lattice and Electronic Thermal Conductivities of ErAs:InGaAs/InGaAlAs Superlattices," *Appl. Phys. Lett.*, vol. 88, p. 242107 (3 pp), 2006.

[15] G. Zeng, J.-H. Bahn, J. Bowers, J. M. O. Zide, R. Singh, A. Shakouri, W. Kim, S. L. Singer, and A. Majumdar, "ErAs:(InGaAs)$_{1-x}$ (InAlAs)$_x$ Alloy Power Generator Modules," *Appl. Phys. Lett.*, vol. 91, p. 263510, 2007.

[16] R. Venkatasubramanian, E. Siivola, T. Colpitts, and B. O'Quinn, "Thin-Film Thermoelectric Devices with High Room-Temperature Figures of Merit," *Nature*, vol. 413, no. 6856, pp. 597–602, 2001.

[17] A. Boukai, Y. Bunimovich, J. Tahir-Kheli, J.-K. Yu, W. Goddard, and J. Heath, "Silicon Nanowires as Efficient Thermoelectric Materials," *Nature*, vol. 451, no. 7175, pp. 168–171, 2008.

[18] D. Li, Y. Wu, R. Fang, P. Yang, and A. Majumdar, "Thermal Conductivity of Si/Ge Superlattice Nanowires," *Appl. Phys. Lett.*, vol. 83, no. 15, pp. 3186–3188, 2003.

[19] H. Sevincli and G. Cuniberti, "Enhanced Thermoelectric Figure of Merit in Edge-Disordered Zigzag Graphene Nanoribbons," *Phys. Rev. B*, vol. 81, p. 113401 (4 pp), 2010.

[20] A. Hochbaum, R. Chen, R. Delgado, W. Liang, E. Garnett, M. Najarian, A. Majumdar, and P. Yang, "Enhanced Thermoelectric Performance of Rough Silicon Nanowires," *Nature*, vol. 451, no. 7175, pp. 163–167, 2008.

[21] A. L. Moore, S. K. Saha, R. S. Prasher, and L. Shi, "Phonon Backscattering and Thermal Conductivity Suppression in Sawtooth Nanowires," *Appl. Phys. Lett.*, vol. 93, p. 083112, 2008.

[22] K. Novoselov, A. Geim, S. Morozov, D. Jiang, Y. Zhang, S. Dubonos, and I. Grigorieva, "Electric Field Effect in Atomically Thin Carbon Films," *Science*, vol. 306, p. 666, 2004.

[23] J.-H. Chen, C. Jang, S. Xiao, M. Ishighami, and M. Fuhrer, "Band gap engineering in graphene and hexagonal BN antidot lattices: A first principles study," *Nature Nanotech.*, vol. 3, no. 4, pp. 206–209, 2008.

[24] J. Seol, I. Jo, A. Moore, L. Lindsay, Z. Aitken, M. Pettes, X. Li, Z. Yao, R. Huang, D. Broido, N. Mingo, R. Ruoff, and L. Shi, "Two-Dimensional Phonon Transport in Supported Graphene," *Science*, vol. 328, no. 5975, pp. 213–216, 2010.

[25] M. Han, B. Ozyilmaz, Y. Zhang, and P. Kim, "Energy Band-Gap Engineering of Graphene Nanoribbons," *Phys. Rev. Lett.*, vol. 98, p. 206805 (4 pp), 2007.

[26] T. G. Pedersen, C. Flindt, J. Pedersen, A.-P. Jauho, N. A. Mortensen, and K. Pedersen, "Optical Properties of Graphene Antidot Lattices," *Phys. Rev. B*, vol. 77, p. 245431 (6pp), 2008.

[27] A. Zhang, H. Teoh, Z. Dai, Y. Feng, and C. Zhang, "Intrinsic and Extrinsic Performance Limits of Graphene Devices on SiO_2," *Appl. Phys. Lett.*, vol. 98, p. 023105 (3 pp), 2011.

[28] A. Balandin, S. Ghosh, W. Bao, I. Calizo, D. Teweldebrhan, F. Miao, and C. Lau, "Superior Thermal Conductivity of Single-Layer Graphene," *Nano Lett.*, vol. 8, no. 3, pp. 902–907, 2008.

[29] J. Hone, M. Whitney, C. Piskoti, and A. Zettl, "Thermal Conductivity of Single-Walled Carbon Nanotubes," *Phys. Rev. B*, vol. 59, pp. R2514–R2516, 1999.

[30] R. Kim, S. Datta, and M. S. Lundstrom, "Influence of Dimensionality on Thermoelectric Device Performance," *J. Appl. Phys.*, vol. 105, p. 034506 (6 pp), 2009.

[31] J. C. Slater and G. F. Koster, "Simplified LCAO Method for the Periodic Potential Problem," *Phys. Rev.*, vol. 94, p. 1498, 1954.

[32] S. Datta, *Quantum Transport: Atom to Transistor*. Cambridge: Cambridge University Press, 2005.

[33] A. Bostwick, T. Ohta, T. Seyller, K. Horn, and E. Rotenberg, "Quasiparticle dynamics in graphene," *Nature Physics*, vol. 3, no. 1, pp. 36–40, 2007.

[34] D. Gunlycke and C. T. White, "Tight-Binding Energy Dispersions of Armchair-Edge Graphene Nanostrips," *Phys. Rev. B*, vol. 77, p. 115116 (6 pp), 2008.

[35] L.-H. Ye, B.-G. Liu, D.-S. Wang, and R. Han, "Ab Initio Phonon Dispersions of Single-Wall Carbon Nanotubes," *Phys. Rev. B*, vol. 69, no. 23, p. 235409 (10 pp), 2004.

[36] J.-W. Jiang, B.-S. Wang, and J.-S. Wang, "First Principle Study of the Thermal Conductance in Graphene Nanoribbon with Vacancy and Substitutional Silicon Defects," *Appl. Phys. Lett.*, vol. 98, no. 11, p. 113114 (3 pp), 2011.

[37] C. Lobo and J. Martins, "Valence Force Field Model for Graphene and Fullerenes," *Z. Phys. D*, vol. 39, pp. 159–164, 1997.

[38] S. Kusminskiy, D. Campbell, and A. C. Neto, "Lenosky's Energy and the Phonon Dispersion of Graphene," *Phys. Rev. B*, vol. 80, p. 035401, 2009.

[39] A. Paul, M. Luisier, and G. Klimeck, "Modified Valence Force Field Approach for Phonon Dispersion: From Zinc-Blende Bulk to Nanowires," *J. Comput. Electron.*, vol. 9, pp. 160–172, 2010.

[40] L. Wirtz and A. Rubio, "The Phonon Dispersion of Graphite Revisited," *Solid-State Commun.*, vol. 131, no. 3–4, pp. 141–152, 2004.

[41] H. Wang, Y. Wang, X. Cao, M. Feng, and G. Lan, "Vibrational Properties of Graphene and Graphene Layers," *J. Raman Spectrosc.*, vol. 40, pp. 1791–1796, 2009.

[42] R. Saito, M. Dresselhaus, and G. Dresselhaus, *Rysical Properties of Carbon Nanotubes.* London: Imperial College Press, 1998.

[43] M. Mohr, J. Maultzsch, E. Dobardzic, S. Reich, I. Milosevic, M. Damnjanovic, A. Bosak, M. Krisch, and C. Thomsen, "Phonon Dispersion of Graphite by Inelastic X-Ray Scattering," *Phys. Rev. B*, vol. 76, no. 3, p. 035439 (7 pp), 2007.

[44] T. B. Boykin, G. Klimeck, and F. Oyafuso, "Valence Band Effective-Mass Expressions in the sp3d5s* Empirical Tight-Binding Model Applied to a Si and Ge Parametrization," *Phys. Rev. B*, vol. 69, no. 11, p. 115201, 2004.

[45] Z. Sui and I. P. Herman, "Effect of Strain on Phonons in Si, Ge, and Si/Ge Heterostructures," *Phys. Rev. B*, vol. 48, pp. 17 938–17 953, 1993.

[46] P. Vogl, H. P. Hjalmarson, and J. D. Dow, "A Semi-Empirical Tight-Binding Theory of the Electronic Structure of Semiconductors," *J. Phys. Chem. Solids*, vol. 44, no. 5, pp. 365–378, 1983.

[47] N. Neophytou, *Quantum and Atomistic Effects in Nanoelectronic Transport Devices.* Electrical and Computer Engineering, Purdue University, 2008.

[48] P. N. Keating, "Effect of Invariance Requirements on the Elastic Strain Energy of Crystals with Application to the Diamond Structure," *Phys. Rev.*, vol. 145, pp. 637–645, 1966.

[49] G. Nilsson and G. Nelin, "Study of the Homology between Silicon and Germanium by Thermal Neutron Spectrometry," *Phys. Rev. B*, vol. 6, no. 10, pp. 3777–3786, 1972.

[50] L. Rego and G. Kirczenow, "Quantized Thermal Conductance of Dielectric Quantum Wires," *Phys. Rev. Lett.*, vol. 81, pp. 232–235, 1998.

[51] R. Landauer, "Spatial Variation of Currents and Fields Due to Localized Scatterers in Metallic Conduction," *IBM J. Res. Dev.*, vol. 1, p. 223 (9pp), 1957.

[52] C. Jeong, R. Kim, M. Luisier, S. Datta, and M. Lundstrom, "On Landauer Versus Boltzmann and Full Band versus Effective Mass Evaluation of Thermoelectric Transport Coefficients," *J. Appl. Phys.*, vol. 107, p. 023707 (7 pp), 2010.

[53] C. Kittel, *Introduction to Solid State Physics.* Wiley, 2005.

[54] W. Zhang, T. Fisher, and N. Mingo, "The Atomistic Green's Function Method: An Efficient Simulation Approach for Nanoscale Phonon Transport," *Numerical Heat Transfer, Part B*, vol. 51, no. 4, pp. 333–349, 2007.

[55] R. Golizadeh-Mojarad, A. N. M. Zainuddin, G. Klimeck, and S. Datta, "Atomistic Non-Equilibrium Greens Function Simulations of Graphene Nano-Ribbons in the Quantum Hall Regime," *J. Comp. Electronics*, vol. 7, no. 3, pp. 407–410, 2008.

[56] M. Sancho, J. Sancho, J. Sancho, and J. Rubio, "Highly Convergent Schemes for the Calculation of Bulk and Surface Green Functions," *J. Phys. F: Met. Phys.*, vol. 15, pp. 851–858, 1985.

[57] C. Jeong, S. Datta, and M. Lundstrom, "Thermal Conductivity of Bulk and Thin-Film Silicon: A Landauer Approach," *J. Appl. Phys.*, vol. 111, p. 093708, 2012.

[58] Y. Ouyang and J. Guo, "A Theoretical Study on Thermoelectric Properties of Graphene Nanoribbons," *Appl. Phys. Lett.*, vol. 94, p. 263107 (3 pp), 2009.

[59] T. Markussen, "Surface Disordered GeSi CoreShell Nanowires as Efficient Thermoelectric Materials," *Phys. Rev. Lett.*, vol. 12, no. 9, pp. 4698–4704, 2012.

[60] G. Srivastava, *The Physics of Phonons.* Adam Hilger-IOP, 1990.

[61] J. M. Ziman, *Electrons and Phonons: The Theory of Transport Phenomena in Solids .* Oxford University Press, 1960.

[62] J. A. Pascual-Gutierrez, J. Y. Murthy, and R. Viskanta, "Thermal Conductivity and Phonon Transport Properties of Silicon Using Perturbation Theory and the Environment-Dependent Interatomic Potential," *J. Appl. Phys.*, vol. 106, p. 063532, 2009.

[63] A. Zhang, Y. Wu, S.-H. Ke, Y. Feng, and C. Zhang, "Intrinsic and Extrinsic Performance Limits of Graphene Devices on SiO$_2$," *arXiv:1105.5858*, 2011.

[64] T. Pedersen, C. Flindt, J. Pedersen, N. Mortensen, A.-P. Jauho, and K. Pedersen, "Graphene Antidot Lattices: Designed Defects and Spin Qubits," *Phys. Rev. Lett.*, vol. 100, no. 13, p. 136804 (4 pp), 2008.

[65] J. Bai, X. Zhong, S. Jiang, Y. Huang, and X. Duan, "Graphene Nanomesh," *Nature Nanotech.*, vol. 5, p. 190, 2010.

[66] Y. M. Zuev, W. Chang, and P. Kim, "Thermoelectric and Magnetothermoelectric Transport Measurements of Graphene," *Phys. Rev. Lett.*, vol. 102, p. 096807, 2009.

[67] P. Wei, W. Bao, Y. Pu, C. N. Lau, and J. Shi, "Anomalous Thermoelectric Transport of Dirac Particles in Graphene," *Phys. Rev. Lett.*, vol. 102, p. 166808, 2009.

[68] Z. Guo, D. Zhang, and X.-G. Gong, "Thermal Conductivity of Graphene Nanoribbons," *Appl. Phys. Lett.*, vol. 95, p. 163103 (3 pp), 2009.

[69] H. Zhang, G. Lee, A. F. Fonseca, T. L. Borders, and K. Cho, "Isotope Effect on the Thermal Conductivity of Graphene," *J. of Nanomaterials*, vol. 2010, p. 537657 (5pp), 2010.

[70] W. Evans, L. Hu, and P. Keblinski, "Thermal Conductivity of Graphene Ribbons from Equilibrium Molecular Dynamics: Effect of Ribbon Width, Edge Roughness, and Hydrogen Termination," *Appl. Phys. Lett.*, vol. 96, p. 203112 (3 pp), 2010.

[71] F. Mazzamuto, J. Saint-Martin, V. H. Nguyen, C. Chassat, and P. Dollfus, "Thermoelectric Performance of Disordered and Nanostructured Graphene Ribbons using Green's Function Method," *J. Comput. Electron.*, vol. 11, no. 1, pp. 67–77, 2012.

[72] D. L. Nika, A. S. Askerov, and A. A. B. *, "Anomalous Size Dependence of the Thermal Conductivity of Graphene Ribbons," *Nano Lett.*, vol. 12, no. 6, pp. 3238–3244, 2012.

[73] Y. Yang and R. Murali, "Impact of Size Effect on Graphene Nanoribbon Transport," *IEEE Electron Device Lett.*, vol. 31, no. 3, pp. 237–239, 2010.

[74] A. Yazdanpanah, M. Pourfath, M. Fathipour, H. Kosina, and S. Selberherr, "A Numerical Study of Line-Edge Roughness Scattering in Graphene Nanoribbons," *IEEE Trans. Electron Devices*, vol. 59, no. 2, pp. 433–440, 2012.

[75] A. D. Liao, J. Z. Wu, X. Wang, K. Tahy, D. Jena, H. Dai, and E. Pop, "Thermally Limited Current Carrying Ability of Graphene Nanoribbons," *Phys. Rev. Lett.*, vol. 106, p. 256801, 2011.

[76] Y. A. Kosevich and A. V. Savin, "Reduction of Phonon Thermal Conductivity in Nanowires and Nanoribbons with Dynamically Rough Surfaces and Edges," *EPL*, vol. 88, no. 1, p. 14002, 2009.

[77] D. L. Nika, E. P. Pokatilov, A. S. Askerov, and A. A. Balandin, "Phonon Thermal Conduction in Graphene: Role of Umklapp and Edge Roughness Scattering," *Phys. Rev. B*, vol. 79, p. 155413, 2009.

[78] A. Savin, Y. Kivshar, and B. Hu, "Suppression of Thermal Conductivity in Graphene Nanoribbons with Rough Edges," *Phys. Rev. B*, vol. 82, p. 195422 (9 pp), 2010.

[79] Z. Aksamija and I. Knezevic, "Lattice Thermal Conductivity of Graphene Nanoribbons: Anisotropy and Edge Roughness Scattering," *Appl. Phys. Lett.*, vol. 98, no. 14, p. 141919 (3 pp), 2011.

[80] Z. Aksamija and I. Knezevic, "Thermal Transport in Graphene Nanoribbons Supported on SiO2," *Phys. Rev. B*, vol. 86, p. 165426, 2012.

[81] J. Wu, "Simulation of Non-Gaussian Surfaces with FFT," *Tribol. Int.*, vol. 37, no. 4, pp. 339–346, 2004.

[82] S. Ghosh, I. Calizo, D. Teweldebrahn, E. Pokatilov, D. Nika, A. Balandin, W. Bao, F. Miao, and C. Lau, "Extremely High Thermal Conductivity of Graphene: Prospects for Thermal Management Applications in Nanoelectronic Circuits," *Appl. Phys. Lett.*, vol. 92, p. 151911 (3 pp), 2008.

[83] H. Karamitaheri, M. Pourfath, R. Faez, and H. Kosina, "Geometrical Effects on the Thermoelectric Properties of Ballistic Graphene Antidot Lattices," *J. Appl. Phys.*, vol. 110, no. 5, p. 054506, 2011.

[84] J. Furst, J. Pedersen, C. Flindt, N. Mortensen, M. Brandbyge, T. Pedersen, and A.-P. Jauho, "Electronic Properties of Graphene Antidot Lattices," *New J. Phys.*, vol. 11, p. 095020, 2009.

[85] D. K. C. Macdonald, *Thermoelectricity: An Introduction to the Principles.* Dover Pubns, 2006.

[86] J. Hone, I. Ellwood, M. Muno, A. Mizel, M. L. Cohen, and A. Zettl, "Thermoelectric Power of Single-Walled Carbon Nanotubes," *Phys. Rev. Lett.*, vol. 80, p. 1042, 1998.

[87] M. Vanevic, V. M. Stojanovic, and M. Kindermann, "Character of Electronic States in Graphene Antidot Lattices: Flat Bands and Spatial Localization," *Phys. Rev. B*, vol. 80, p. 045410 (8pp), 2009.

[88] D. Areshkin, D. Gunlycke, and C. White, "Ballistic Transport in Graphene Nanostrips in the Presence of Disorder: Importance of Edge Effects," *Nano Lett.*, vol. 7, no. 1, pp. 204–210, 2007.

[89] D. Bahamon, A. Pereira, and P. Schulz, "Third Edge for a Graphene Nanoribbon: A Tight-Binding Model Calculation," *Phys. Rev. B*, vol. 83, no. 7, p. 155436 (6 pp), 2011.

[90] J. Lahiri, Y. Lin, P. Bozkurt, I. I. Oleynik, and M. Batzill, "An Extended Defect in Graphene as a Metallic Wire," *Nature Nanotech.*, vol. 5, pp. 326–329, 2010.

[91] D. J. Appelhans, L. D. Carr, and M. T. Lusk, "Embedded Ribbons of Graphene Allotropes: An Extended Defect Perspective," *New J. Phys.*, vol. 12, p. 125006 (21pp), 2010.

[92] M. T. Lusk, D. T. Wu, and L. D. Carr, "Graphene Nanoengineering and the Inverse Stone-Thrower-Wales Defect," *Phys. Rev. B*, vol. 81, p. 155444 (9 pp), 2010.

[93] V. M. Pereira, F. Guinea, J. M. B. L. dos Santos, N. M. R. Peres, and A. H. C. Neto, "Disorder Induced Localized States in Graphene," *Phys. Rev. Lett.*, vol. 96, p. 036801 (4 pp), 2006.

[94] N. Neophytou, D. Kienle, E. Polizzi, and M. P. Anantram, "," *Appl. Phys. Lett.*, vol. 88, p. 242106 (3 pp), 2006.

[95] M. U. Kahaly, S. P. Singh, and U. V. Waghmare, "Carbon Nanotubes with an Extended Line Defect," *Small*, vol. 4, no. 12, pp. 2209–2213, 2008.

[96] G. J. Snyder and E. S. Toberer, "Complex Thermoelectric Materials," *Nature Materials*, vol. 7, pp. 105–114, 2008.

[97] N. Neophytou and H. Kosina, "Effects of Confinement and Orientation on the Thermoelectric Power Factor of Silicon Nanowires," *Phys. Rev. B*, vol. 83, p. 245305 (16 pp), 2011.

[98] I. Ponomareva, D. Srivastava, and M. Menon, "Thermal Conductivity in Thin Silicon Nanowires:Phonon Confinement Effect," *Nano Lett.*, vol. 7, pp. 1155–1159, 2007.

[99] N. Yang, G. Zhang, and B. Li, "Ultralow Thermal Conductivity of Isotope-Doped Silicon Nanowires," *Nano Lett.*, vol. 8, pp. 276–280, 2008.

[100] S.-C. Wang, X.-G. Liang, X.-H. Xu, and T. Ohara, "Thermal Conductivity of Silicon Nanowire by Nonequilibrium Molecular Dynamics Simulations," *J. Appl. Phys.*, vol. 105, p. 014316, 2009.

[101] M. Liangraksa and I. K. Puri, "Lattice Thermal Conductivity of a Silicon Nanowire Under Surface Stress," *J. Appl. Phys.*, vol. 109, p. 113501, 2011.

[102] J. H. Oh, M. Shin, and M.-G. Jang, "Phonon Thermal Conductivity in Silicon Nanowires: The Effects of Surface Roughness at Low Temperatures," *J. Appl. Phys.*, vol. 111, p. 044304, 2012.

[103] N. Mingo, "Calculation of Si Nanowire Thermal Conductivity using Complete Phonon Dispersion Relations," *Phys. Rev. B*, vol. 68, p. 113308, 2003.

[104] X. Lu and J. Chu, "," *J. Appl. Phys.*, vol. 100, p. 014305, 2006.

[105] M.-J. Huang, W.-Y. Chong, and T.-M. Chang, "," *J. Appl. Phys.*, vol. 99, p. 114318, 2006.

[106] P. Martin, Z. Aksamija, E. Pop, and U. Ravaioli, "Impact of Phonon-Surface Roughness Scattering on Thermal Conductivity of Thin Si Nanowires," *Phys. Rev. Lett.*, vol. 102, p. 125503, 2009.

[107] A. Paul, M. Luisier, and G. Klimeck, "Shape and Orientation Effects on the Ballistic Phonon Thermal Properties of Ultra-Scaled Si Nanowires," *J. Appl. Phys.*, vol. 110, p. 114309, 2011.

[108] T. Thonhauser and G. D. Mahan, "," *Phys. Rev. B*, vol. 69, p. 075213, 2004.

[109] X. Lu, J. H. Chu, and W. Z. Shen, "," *J. Appl. Phys.*, vol. 93, pp. 1219–1229, 2003.

[110] J. Zou and A. Balandin, "Phonon Heat Conduction in a Semiconductor Nanowire," *J. Appl. Phys.*, vol. 89, p. 2932, 2001.

[111] T. Markussen, A.-P. Jauho, and M. Brandbyge, "Heat Conductance Is Strongly Anisotropic for Pristine Silicon Nanowires," *Nano Lett.*, vol. 8, no. 11, pp. 3771–3775, 2008.

[112] Z. Aksamija and I. Knezevic, "Anisotropy and Boundary Scattering in the Lattice Thermal Conductivity of Silicon Nanomembranes," *Phys. Rev. B*, vol. 82, p. 045319, 2010.

[113] H. Karamitaheri, N. Neophytou, M. K. Taheri, R. Faez, and H. Kosina, "Calculation of Confined Phonon Spectrum in Narrow Silicon Nanowires Using the Valence Force Field Method," *J. Electron. Mater.*, vol. DOI: 10.1007/s11664-013-2533-z, 2013.

[114] N. Neophytou and H. Kosina, "Hole Mobility Increase in Ultra-Narrow Si Channels under Strong (110) Surface Confinement," *Appl. Phys. Lett.*, vol. 99, p. 092110, 2011.

[115] N. Neophytou and G.Klimeck, "Design Space for Low Sensitivity to Size Variations in [110] PMOS Nanowire Devices: The Implications of Anisotropy in the Quantization Mass," *Nano Lett.*, vol. 9, no. 2, pp. 623–630, 2009.

[116] N. Neophytou and H. Kosina, "Large Thermoelectric Power Factor in p-type Si (110)/[110] Ultra-Thin-Layers Compared to Differently Oriented Channels," *J. Appl. Phys.*, vol. 112, p. 024305, 2012.

[117] W. S. Hurst and D. R. Frankl, "Thermal Conductivity of Silicon in the Boundary Scattering Regime," *Phys. Rev.*, vol. 186, no. 3, pp. 801–810, 1969.

[118] M. G. Holland, "Analysis of Lattice Thermal Conductivity," *Phys. Rev.*, vol. 132, no. 6, pp. 2461–2471, 1963.

[119] M. Asen-Palmer, K. Bartkowski, E. Gmelin, M. Cardona, A. P. Zhernov, A. V. Inyushkin, A. Taldenkov, V. I. Ozhogin, K. M. Itoh, and E. E. Haller, "Thermal Conductivity of Germanium Crystals with Different Isotopic Compositions," *Phys. Rev. B*, vol. 56, no. 15, p. 9431, 1997.

[120] N. Mingo and D. A. Broido, "Length Dependence of Carbon Nanotube Thermal Conductivity and the "Problem of Long Waves"," *Nano Lett.*, vol. 5, no. 7, pp. 1221–1225, 2005.

[121] L. Hu, W. J. Evans, and P. Keblinski, "One-Dimensional Phonon Effects in Direct Molecular Dynamics Method for Thermal Conductivity Determination," *J. Appl. Phys.*, vol. 110, p. 113511, 2011.

[122] D. Donadio and G. Galli, "Temperature Dependence of the Thermal Conductivity of Thin Silicon Nanowires," *Nano Lett.*, vol. 10, no. 3, pp. 847–851, 2010.

[123] N. Mingo, L. Yang, D. Li, and A. Majumdar, "Predicting the Thermal Conductivity of Si and Ge Nanowires," *Nano Lett.*, vol. 3, no. 12, pp. 1713–1716, 2003.

[124] K. Termentzidis, T. Barreteau, Y. Ni, S. Merabia, X. Zianni, Y. Chalopin, P. Chantrenne, and S. Volz, "Modulated SiC Nanowires: Molecular Dynamics Study of Their Thermal Properties," *Phys. Rev. B*, vol. 87, p. 125410, 2013.

[125] J. Wang and J.-S. Wang, "Dimensional Crossover of Thermal Conductance in Nanowires," *Appl. Phys. Lett.*, vol. 90, p. 241908, 2007.

[126] L. Lindsay, D. A. Broido, and N. Mingo, "Lattice Thermal Conductivity of Single-Walled Carbon Nanotubes: Beyond the Relaxation Time Approximation and Phonon-Phonon Scattering Selection Rules," *Phys. Rev. B*, vol. 80, p. 125407, 2009.

[127] C. W. Chang, D. Okawa, H. Garcia, A. Majumdar, and A. Zettl, "Breakdown of Fourier's Law in Nanotube Thermal Conductors," *Phys. Rev. Lett.*, vol. 101, p. 075903, 2008.

[128] G. Wu and J. Dong, "Anomalous Heat Conduction in a Carbon Nanowire: Molecular Dynamics Calculations," *Phys. Rev. B*, vol. 71, p. 115410, 2005.

[129] S. Lepri, R. Livi1, and A. Politi, "Heat Conduction in Chains of Nonlinear Oscillators," *Phys. Rev. Lett.*, vol. 78, p. 1896, 1997.

[130] T. Hatano, "Heat Conduction in the Diatomic Toda Lattice Revisited," *Phys. Rev. E*, vol. 59, pp. R1–R4, 1999.

[131] X. Lu, "Lattice Thermal Conductivity of Si Nanowires: Effect of Modified Phonon Density of States," *J. Appl. Phys.*, vol. 104, p. 054314, 2008.

[132] A. J. H. McGaughey, E. S. Landry, D. P. Sellan, and C. H. Amon, "Size-Dependent Model for Thin Film and Nanowire Thermal Conductivity," *Appl. Phys. Lett.*, vol. 99, p. 131904, 2011.

[133] J. E. Turney, A. J. H. McGaughey, and C. H. Amon, "In-Plane Phonon Transport in Thin Films," *J. Appl. Phys.*, vol. 107, p. 024317, 2010.

[134] Z. Tian, K. Esfarjani, J. Shiomi, A. S. Henry, and G. Chen, "On the Importance of Optical Phonons to Thermal Conductivity in Nanostructures," *Appl. Phys. Lett.*, vol. 99, p. 053122, 2011.

[135] W. Liu and M. Asheghi, "Thermal Conduction in Ultrathin Pure and Doped Single-Crystal Silicon Layers at High Temperatures ," *J. Appl. Phys.*, vol. 98, p. 123523, 2005.

[136] X. Lu, "Longitudinal Thermal Conductivity of Radial Nanowire Heterostructures," *J. Appl. Phys.*, vol. 106, p. 064305, 2009.

[137] M. Luisier, "Atomistic Modeling of Anharmonic Phonon-Phonon Scattering in Nanowires," *Phys. Rev. B*, vol. 86, p. 245407, 2012.

[138] S. Ghosh, W. Bao, D. L. Nika, S. Subrina, E. P. Pokatilov, C. N. Lau, and A. A. Balandin, "Dimensional Crossover of Thermal Transport in Few-Layer Graphene," *Nature Materials*, vol. 9, pp. 555–558, 2010.

[139] M. Maldovan, "Thermal Conductivity of Semiconductor Nanowires from Micro to Nano Length Scales," *J. Appl. Phys.*, vol. 111, p. 024311, 2012.

[140] S. G. Volz and G. Chen, "Molecular Dynamics Simulation of Thermal Conductivity of Silicon Nanowires," *Appl. Phys. Lett.*, vol. 75, p. 2056, 1999.

[141] Y. Chen, D. Li, J. R. Lukes, and A. Majumdar, "Monte Carlo Simulation of Silicon Nanowire Thermal Conductivity," *J. Heat Transfer*, vol. 127, p. 1129, 2005.

[142] J. Tang, H.-T. Wang, D. H. Lee, M. Fardy, Z. Huo, T. P. Russell, and P. Yang, "Holey Silicon as an Efficient Thermoelectric Material," *Nano Lett.*, vol. 10, no. 10, pp. 4279–4283, 2010.

[143] N. Neophytou and H. Kosina, "Effects of Confinement and Orientation on the Thermoelectric Power Factor of Silicon Nanowires," *Phys. Rev. B*, vol. 83, p. 245305, 2011.

[144] N. Neophytou and H. Kosina, "Large Enhancement in Hole Velocity and Mobility in P-type [110] and [111] Silicon Nanowires by Cross Section Scaling: An Atomistic Analysis," *Nano Lett.*, vol. 10, no. 12, pp. 4913–4919, 2010.

[145] E. B. Ramayya, L. N. Maurer, A. H. Davoody, and I. Knezevic, "Thermoelectric Properties of Ultrathin Silicon Nanowires," *Phys. Rev. B*, vol. 86, p. 115328, 2012.

[146] S. Jin, M. V. Fischetti, and T. Tang, "Modeling of Electron Mobility in Gated Silicon Nanowires at Room Temperature: Surface Roughness Scattering, Dielectric Screening, and Band Nonparabolicity," *J. Appl. Phys.*, vol. 102, p. 083715, 2007.

[147] N. Neophytou and H. Kosina, "On the Interplay between Electrical Conductivity and Seebeck Coefficient in Ultra-Narrow Silicon Nanowires," *J. Electron. Mater.*, vol. 41, no. 6, pp. 1305–1311, 2012.

[148] P. N. Martin, Z. Aksamija, E. Pop, and U. Ravaioli, "Reduced Thermal Conductivity in Nanoengineered Rough Ge and GaAs Nanowires," *Nano Lett.*, vol. 10, no. 4, pp. 1120–1124, 2010.

[149] R. Chen, A. I. Hochbaum, P. Murphy, J. Moore, P. Yang, and A. Majumdar, "Thermal Conductance of Thin Silicon Nanowires," *Phys. Rev. Lett.*, vol. 101, p. 105501 (4pp), 2008.

[150] T. Markussen, A.-P. Jauho, and M. Brandbyge, "Surface-Decorated Silicon Nanowires: A Route to High-ZT Thermoelectrics," *Phys. Rev. Lett.*, vol. 103, p. 055502, 2009.

[151] N. Mingo and L. Yang, "Phonon Transport in Nanowires Coated with an Amorphous Material: An Atomistic Green's Function Approach," *Phys. Rev. B*, vol. 68, p. 245406, 2003.

List of Publications

Publications in Scientific Journals

[1] **H. Karamitaheri**, N. Neophytou, H. Kosina: "Ballistic Phonon Transport in Ultra-Thin Silicon Layers: Effects of Confinement and Orientation"; Journal of Applied Physics, 113 (2013), 20; 204305-1 - 204305-9.

[2] **H. Karamitaheri**, N. Neophytou, M. Karami Taheri, R. Faez, H. Kosina: "Calculation of Confined Phonon Spectrum in Narrow Silicon Nanowires Using the Valence Force Field Method"; Journal of Electronic Materials, 42 (2013), 7; 2091 - 2097.

[3] **H. Karamitaheri**, M. Pourfath, R. Faez, H. Kosina: "Atomistic Study of the Lattice Thermal Conductivity of Rough Graphene Nanoribbons"; IEEE Transactions on Electron Devices, 60 (2013), 7; 2142 - 2147.

[4] **H. Karamitaheri**, N. Neophytou, M. Pourfath, R. Faez, H. Kosina: "Engineering Enhanced Thermoelectric Properties in Zigzag Graphene Nanoribbons"; Journal of Applied Physics, 111 (2012), 5; 054501-1 - 054501-9.

[5] **H. Karamitaheri**, N. Neophytou, M. Pourfath, H. Kosina: "Study of Thermal Properties of Graphene-Based Structures using the Force Constant Method"; Journal of Computational Electronics (invited), 11 (2012), 1; 14 - 21.

[6] **H. Karamitaheri**, M. Pourfath, R. Faez, H. Kosina: "Geometrical Effects on the Thermoelectric Properties of Ballistic Graphene Antidot Lattices"; Journal of Applied Physics, 110 (2011), 5; 054506-1 - 054506-6.

[7] **H. Karamitaheri**, M. Pourfath, M. Pazoki, R. Faez, H. Kosina: "Graphene-Based Antidots for Thermoelectric Applications"; Journal of the Electrochemical Society, 158 (2011), 12; K213 - K216.

[8] H. Rabiee Golgir, R. Faez, M. Pazoki, **H. Karamitaheri**, R. Sarvari: "Investigation of Quantum Conductance in Semiconductor Single-Wall Carbon Nanotubes: Effect of Strain and Impurity"; Journal of Applied Physics, 110 (2011), 6; 064320-1 - 064320-6.

Manuscripts currently under Review

[1] **H. Karamitaheri**, N. Neophytou, H. Kosina: "Anomalous Diameter Dependence of Thermal Conductivity in Ultra-Thin Si Nanowires"; Journal of Applied Physics, Under review.

[2] **H. Karamitaheri**, N. Neophytou, H. Kosina: "Thermal Conductivity of Si Nanowires and Ultra Thin-Layers Using Atomistic Phonon Dispersions"; Journal of Electronic Materials, Under review.

[3] N. Neophytou, **H. Karamitaheri**, H. Kosina: "Low Dimensional Semiconductor Thermoelectric Materials: Design Approaches from Atomistic Calculations for Electrons and Phonons"; Journal of Electronic Materials, Under review.

Contributions to Books

[1] **H. Karamitaheri**, M. Pourfath, R. Faez, H. Kosina: "An Investigation of the Geometrical Effects on the Thermal Conductivity of Graphene Antidot Lattices"; in: "Dielectrics in Nanosystems -and- Graphene, Ge/III-V, Nanowires and Emerging Materials for Post-CMOS Applications 3", Z. Karim, D. Misra, P. Srinivasan, Y. Obeng, S. De Gendt (ed.); ECS Transactions, 2011, ISBN: 978-1-56677-864-0, 185 - 192.

Publications in Conference Proceedings

[1] **H. Karamitaheri**, N. Neophytou, H. Kosina: "Thermal Conductivity of Si Nanowires and Ultra Thin-Layers Using Atomistic Phonon Dispersions"; Talk: The 31st International Conference on Thermoelectrics, Kobe, Japan; 2013-06-30 - 2013-07-04; in: "Book of Abstracts", (2013), 1 page.

[2] N. Neophytou, **H. Karamitaheri**, H. Kosina: "Low Dimensional Semiconductor Thermoelectric Materials: Design Approaches from Atomistic Calculations for Electrons and Phonons"; Talk: The 31st International Conference on Thermoelectrics, Kobe, Japan; 2013-06-30 - 2013-07-04; in: "Book of Abstracts", (2013), 1 page.

[3] **H. Karamitaheri**, N. Neophytou, H. Kosina: "Thermal Conductivity of Si Nanowires Using Atomistic Phonon Dispersions"; Talk: International Workshop on Computational Electronics (IWCE), Nara, Japan; 2013-06-04 - 2013-06-07; in: "Proceedings of the 16th International Workshop on Computational Electronics (IWCE 2013)", (2013), 98 - 99.

[4] **H. Karamitaheri**, M. Pourfath, N. Neophytou, H. Kosina: "Theoretical Study of a Zigzag Graphene Nanoribbon Field Effect Transistor"; Talk: Meeting of the Electrochemical Society (ECS), Honolulu, USA; 2012-10-07 - 2012-10-12; in: "ECS Meeting", (2012), 1 page.

[5] **H. Karamitaheri**, N. Neophytou, H. Kosina: "Calculations of Confined Phonon Spectrum in Narrow Si Nanowires using the Valence Force Field Method"; Poster: The 31st International & 10th European Conference on Thermoelectrics, Aalborg, Denmark; 2012-07-09 - 2012-07-12; in: "Book of Abstracts", (2012), 1 page.

[6] N. Neophytou, **H. Karamitaheri**, H. Kosina: "Engineering the Thermoelectric Power Factor of Si and Ge Ultra Narrow 1D Nanowires and 2D Thin Layers Using Atomistic Modeling"; Talk: The 31st International & 10th European Conference on Thermoelectrics, Aalborg, Denmark; 2012-07-09 - 2012-07-12; in: "Book of Abstracts", (2012), 1 page.

[7] N. Neophytou, **H. Karamitaheri**, H. Kosina: "Atomistic Design of Ultra-Narrow Silicon Nanowires for Improved Electronic and Thermoelectric Applications"; Talk: International Conference on Nanosciences and Nanotechnologies, Thessaloniki, Greece; 2012-07-03 - 2012-07-06; in: "Abstract Book", (2012), 46.

[8] **H. Karamitaheri**, M. Pourfath, H. Kosina: "Highly Sensitive Graphene Antidot Lattice Chemiresitor Sensor"; Poster: Graphene Week, Delft, Netherlands; 2012-06-04 - 2012-06-08; in: "Book of Abstracts", (2012).

[9] M. Moradinasab, **H. Karamitaheri**, M. Pourfath, H. Kosina: "On the Role of Stone-Wales Defects on the Performance of Graphene Nanoribbon Photo Detectors"; Poster: Graphene Week, Delft, Netherlands; 2012-06-04 - 2012-06-08; in: "Book of Abstracts", (2012).

[10] **H. Karamitaheri**, N. Neophytou, M. Pourfath, H. Kosina: "Engineering the Thermoelectric Power Factor of Metallic Graphene Nanoribbons"; Talk: International Workshop on Computational Electronics (IWCE), Madison, WI, USA; 2012-05-22 - 2012-05-25; in: "Proceedings of the 15th International Workshop on Computational Electronics (IWCE 2012)", (2012), 77 - 78.

[11] **H. Karamitaheri**, M. Pourfath, R. Faez, H. Kosina: "An Investigation of ZGNR-Based Transistors"; Talk: International Semiconductor Device Research Symposium (ISDRS), Washington DC , USA; 2011-12-07 - 2011-12-09; in: "Proceedings of the International Semiconductor Device Research Symposium (ISDRS 2011)", (2011), ISBN: 978-1-4577-1754-3; 2 pages.

[12] **H. Karamitaheri**, M. Pourfath, N. Neophytou, M. Pazoki, H. Kosina: "First Principle Study of Ballistic Thermal Conductance of Graphene Antidot Lattices for Thermoelectric Applications"; Talk: Carbon-Based Low Dimensional Materials (Carbomat), Catania, Italy; 2011-12-05 - 2011-12-07; in: "Proceedings of the 2nd CARBOMAT Workshop", (2011), ISBN: 978-88-8080-124-5; 19 - 22.

[13] **H. Karamitaheri**, M. Pourfath, R. Faez, H. Kosina: "Transport Gap Engineering in Zigzag Graphene Nanoribbons"; Poster: Trends in Nanotechnology Conference (TNT), Canary Islands, Spain; 2011-11-21 - 2011-11-25; in: "Poster Abstracts Book (TNT 2011)", (2011), 2.

[14] **H. Karamitaheri**, <u>M. Pourfath</u>, R. Faez, H. Kosina: "An Investigation of the Geometrical Effects on the Thermal Conductivity of Graphene Antidot Lattices"; Talk: 219th ECS Meeting, Montreal, Canada; 2011-05-01 - 2011-05-06; in: 219th ECS Meeting, (2011), 1 page.

[15] **H. Karamitaheri**, <u>M. Pourfath</u>, R. Faez, H. Kosina: "Hydrogen-Passivated Graphene Antidot Structures for Thermoelectric Applications"; Poster: 12th International Conference on Thermal, Mechanical and Multi-Physics Simulation and Experiments in Microelectronics and Microsystems, Linz, Austria; 2011-04-18 - 2011-04-20; in: "Proceedings Conference on Thermal, Mechanical and Multi-Physics Simulation and Experiments in Microelectronics and Micro-systems", IEEE, (2011), ISBN: 978-1-4577-0105-4; 4 pages.

[16] **H. Karamitaheri**, <u>M. Pourfath</u>, R. Faez, H. Kosina: "Thermal Properties of Graphene Antidots"; Poster: Nanoelectronics Days 2010, Aachen; 2010-10-04 - 2010-10-07; in: Abstract Book of the Nanoelectronics Days 2010, (2010), 102.

Publication statistics from scholar.google.com: Citations=24, h-index=3, i10-index=1.

	Author	Co-author	Total
Journals	7	1	8
Journals (under review)	2	1	3
Conferences	12	4	16
Contributions to books	1	0	1
Total	22	6	28

Curriculum Vitae

September 2002 – September 2006

    Kashan University, Kashan, Iran

    Bachelor's of Electrical Engineering

    Concentration: Power electronic circuits

    Graduation with high distinction and ranked 1st for outstanding academic achievement

September 2006 – September 2008

    Sharif University of Technology, Tehran, Iran

    Graduate program in micro- and nano-electronic devices at the School of Electrical Engineering

    Masters's Thesis: "Band Structure Calculation of Defective Carbon Nanotube for Decreasing Contact Resistance between CNT and Metallic Electrode"

September 2008 – February 2011

    Sharif University of Technology, Tehran, Iran

    PhD by course at the School of Electrical Engineering

Since February 2011

    Vienna University of Technology, Austria

    PhD program at the Institute for Microelectronics